Lateral Surface Superlattice Devices

by Ramon Cuscó Cornet

Thesis submitted to the Univeristy of Glasgow for the degree
of Doctor of Philosophy. April 1994
Department of Electronics and Electrical Engineering

Abstract

A fabrication process was developed to realize lateral surface superlattice (LSSL) devices on high-mobility modulation-doped GaAs/AlGaAs heterostructures for low-temperature transport studies. The process involved the use of high-resolution electron beam lithography to define an interdigitated array of metal gates, with periodicities down to 230 nm and a 1:1 mark space ratio. The two sets of interdigitated gate arrays, defined by metallization and lift-off, could be independently biased so that an independent control of the the average electrostatic potential and of the periodic potential amplitude was possible. Two different heterostructures were used: a conventional HEMT GaAs/AlGaAs layer, where the 2DEG was formed 90 nm below the surface and a novel, δ-doped heterostructure where the 2DEG was only 28 nm deep.

The devices were characterized at low temperatures ($\approx$ 70 mK) by means of magnetoresistance measurements. The effect of the periodic gate potential on the 2DEG was reflected in oscillations of the magnetoresistance due to commensurability resonances between the cyclotron orbit and the period of the superlattice potential. A strong first harmonic of the commensurability oscillations was observed in the magnetoresistance traces measured on the shallow-2DEG device, suggesting an enhanced contrast of the superlattice potential due to the proximity of the gates to the 2DEG. The strength of the harmonic signal was quantified using Fourier analysis and it was found that the high first harmonic contents could not be explained by simple electrostatic models. An alternative source of modulation, involving the strain field caused by the differential contraction of the metal gates, is discussed. The potential profile obtained from the strain model is in better agreement with experimental results and confirms that the enhanced contrast of the potential is due to the proximity of the gates to the 2DEG. An identical device fabricated on conventional HEMT material exhibited purely sinusoidal commensurability oscillations.

A study of the commensurability oscillations as a function of gate bias was carried out, and some information on the causes of device performance degradation was extracted. In particular, it was found that a parallel sheet of parasitic charge in the shallow-HEMT layer was responsible for its relatively high mobility but also for strongly reducing the electrostatic modulation of the 2DEG by the gate potential. Nevertheless, some indication of perio .d doubling due to differential bias was observed in the Fourier tranform of the experimental data.

In this work we demonstrated the feasibility to fabricate laterally gated devices on shallow HEMT layers and the enhanced contrast of the potential at the 2DEG, achieved because of the proximity of the gates to the 2DEG. However, other problems have been identified that limit the advantages of the increased potential contrast:

- an important component of the potential modulation arises from the strain field generated by the differential contraction of the metal gates on the surface of the semiconductor; the strain couples to the 2DEG via the deformation potential and gives rise to a residual potential modulation that cannot be controlled by the gate bias.

- the presence of a parasitic sheet of electrons in the novel shallow-HEMT layer strongly reduces the efficiency of the gates in electrostatically modulating the 2DEG potential

Further work should be directed to improve the design of the shallow-HEMT layers so that its full potential in relation to laterally gated devices could be achieved.

Acknowledgements

The successful completion of the work described in this Thesis has been possible thanks to the collaboration and helpful advice of many colleagues and friends of the Nanoelectronics Research Center and Physics Department of the University of Glasgow.

I wish to thank specially Mahfuzur Rahman for all his help with setting up the measuring system and for sharing the frustrations through the long process of learning nanodevice fabrication and measuring. His excellent data acquisition program has facilitated enormously the job of measuring the few surviving devices

Professor Steven Beumont, my supervisor, for the unrestricted use of the excellent fabrication facilities of Ultra Small Structures Laboratory and for his support to this project. I gratefully aknowledge financial assistance from the Department to attend a Winter School in France

Clivia Sotomayor Torres, my second supervisor, for offering me the opportunity to come to the Department as a PhD research student and giving her support in critical moments of this project.

The friendly and highly efficient technical support of USSL coordinated by Douglas McIntire. Dave Gourlay has been of great assistance in electron microscopy.

Steven Thoms and Iain Thayne for sharing their expertise in nano-fabrication techniques

Douglas Irons, from whom I learned the handling of cryogenic liquids, for all his efforts in trying to fix a doomed 8T cryostat and the creation of a state-of-the art non-magnetic sample holder for the magnet insert that has made sample mounting less painful and a lot safer.

Alex Ross, for his support and for making sure that Helium deliveries were made on time.

Bobby Burns, for taking care of the dilution refrigerator and lowering and raising the fridge insert as many times as it was necessary until finding a reasonably good device.

Andrew Long, for his help with the fridge operation and for being usually available to discuss problems (lots) and results (few).

John Davies, for his contribution to put the interpretation of the experimental data on solid theoretical ground. I am indebted to him for sending me a manuscript of his paper on the theory of periodic modulation which has been a pleasure to read and has clarified my understanding of the devices.

Eleftherios Skuras, for his contribution to the Shallow HEMT material development and for his help with the fridge operation at awkward times.

John Williamson, for all his efforts in trying to cheer me up, looking for wonderful results out of totally useless samples.

John Weaver, for his assistance in the fight against electrical noise in the measurement system.

Ivan A. Larkin for the suggestion of strain as a source of 2DEG modulation.

To all of them and to the rest of colleagues and friends in the Department, for their sympathy and hospitality.

It is a pleasure to acknowledge frequent and inspiring discussions via e-mail with Andrew Long and John Davies during the period of writing up of this thesis.

Special thanks to Jordi Pascual, my tutor at the University of Barcelona, who has always encouraged me to keep it up, for all his support during this years. I am indebted to him for his advice and for all his efforts to facilitate my return.

I gratefully acknowledge the financial support of the Spanish *Ministerio de Educación y Ciencia* through a Postgraduate Scholarship for the completion of this work.

for my parents

Contents

List of Figures

List of Tables

Chapter 1

Introduction

1.1 Motivation

In the modern theory of solids, the optical and electronic properties of a crystal emerge from the periodic electrostatic potential created by the arrangement of the nuclei in a lattice with a definite symmetry. The periodic potential opens gaps in the energy of the electrons and prevents the propagation of electrons whose energy lies in the gap through Bragg reflection of their wave functions.

The development of high quality crystal growth techniques has made it possible to obtain epitaxial structures with compositional control down to atomic level. In 1970 Esaki and Tsu [1] proposed the creation of an artificial 1D superlattice by alternating epitaxial growth of two different semiconductors. This type of structure was realized and studied experimentally [2] but minigap effects were obscured by the free in-plane motion of the electrons perpendicular to the superlattice axis.

More recently, there have been spectacular improvements in the quality of semiconductor heterostructures grown by Molecular Beam Epitaxy. The III-V

alloy systems, and in particular the GaAs/AlGaAs heterostructures, have been extensively studied because of the good accord between the lattice parameters of GaAs and AlGaAs that makes interface roughness scattering negligible and keeps the band structure related parameters, such as the effective mass, close to the bulk values due to absence of strain. In modulation doped heterostructures, the carriers provided by the intentional impurities are confined at the GaAs/AlGaAs interface in a potential well resulting from the combined effect of the conduction band discontinuity and the attractive electrostatic potential created by the remote ionized donors. In a typical heterostructure, the width of the confining well is of about 10 nm whereas the Fermi wavelength of the electrons is $\lambda_F \approx 50\,\text{nm}$. Therefore the confined electrons have a 2D dynamical behaviour. The ionized impurities are physically separated from the 2-Dimensional Electron Gas (2DEG) by an undoped spacer layer that greatly enhances the electron mobility. Nowadays conventional modulation doped heterostructures in which the electron mean free path exceeds 10μm are routinely grown.

A parallel advance in lithographic fabrication techniques has made it possible to define lateral gate structures on a submicron length scale. The relatively large Fermi wavelength of the electrons in the 2DEG, the large values of mobility and mean free path attainable in modulation doped heterostructures and the ability to control the superlattice potential strength and the Fermi level position with gate bias make Lateral Surface SuperLattice devices an ideal system to study the efects of a periodic modulation on electronic transport. A specially attractive feature of these devices is their mesoscopic nature which opens up the possibility of observing phenomena that are precluded in a crystal because of the large Brillouin zone dimensions and short mean free paths of crystal electrons. An electron gas in the presence of a periodic potential and a dc electric field should exhibit Bloch oscillations [3], an oscillating

current resulting from Bragg reflections of the electrons at the boundaries of the Brillouin zone. These oscillations are never seen in a real crystal because the electron can only traverse small portions of the Brillouin zone before being scattered. In a LSSL device the large coherence length of the electrons and the relatively small change in k necesssary to approach the zone boundary should make the observation of Bloch oscillations easier. Such a device would have an important technological application as an oscillator for the milimetric range.

Other bandstructure-related phenomena have been predicted. The Fermi Level can be varied by the bias applied to the gates, and as it traverses the artificial minigaps sudden drops of the conductance are expected. Theoretical calculations [4] reveal a reach structure with possible applications to multi-state logic devices. A weak periodic structure in the conductance as a function of gate bias has been measured in a LSSL device by K. Ismail et al. [5].

In the presence of a perpendicular magnetic field, the magnetic length enters as a new fundamental length scale in the description of the electron system. When the magnetic length becomes comparable to the period of the superlattice, new commensurability effects are predicted. This interesting regime is not experimentally attainable in ordinary crystals because of the small lattice constant. Once again, LSSL devices open up new regimes to experimental study since the situation where $l_m = a$ is achieved at moderate magnetic fields (typically around 1T) and the large values of mean free path in these devices allow the electrons to experience the effect of many periods of the superlattice potential. One of the most spectacular theoretical predictions is that a 2D periodic potential in the presence of a strong perpendicular magnetic field gives rise to a self similar energy spectrum [6], known as Hofstader butterfly, depending on the number of flux quanta, $\Phi_0 \equiv h/e$, per unit cell. As yet there is no clear experimental evidence of these artificial bandstructure effects.

The only clear indication of artificial bandstructure formation in a laterally gated device has been obtained by Kowenhoven et al. [7] in a periodically modulated narrow channel defined by a corrugated split gate in the quantum Hall effect regime. The formation of edge states makes the transport problem unidimensional and enhances the effect of the periodic potential giving rise to a magnetically induced bandstructure which is not present at $B = 0$.

All the effects described so far are associated with the formation of artificial bandstructure and, as it has been pointed out, their experimental detection has proven to be very elusive. Transport properties are determined by the electrons at the Fermi level and therefore the relevant minigap occurs at $k_n \equiv 2\pi n/a$, where $n \sim ak_F/\pi$. In a LSSL device with a typical carrier density of $N_{2D} \sim 3 \times 10^{11}\,\mathrm{cm}^{-2}$ and a superlattice period of $a \sim 200\,\mathrm{nm}$, the Fermi level lies in the tenth miniband. Since the magnitude of the gap is given by the Fourier component of the periodic potential at wave vector k_n, in the case of weak, sinusoidal potentials, energy gaps of order higher than unity are totally negligible. Consequently, only when the Fermi level lies in the first energy gap the drop in conductance will be significant. To achieve this regime with present AlGaAs/GaAs heterostructures one should use superlattice periodicities down to $\lambda_F/2 \sim 25\,\mathrm{nm}$, which are well out of range of currently available fabrication techniques. Apart from the formidable technological challenge of reducing the superlattice periodicity, the progress towards a true LSSL device requires the development of novel heterostructures in which the 2DEG is formed much closer to the surface while retaining the high values of mobility that are characteristic of standard modulation-doped heterostructures. As we shall demonstrate in Chapter 4, the proximity of the 2DEG to the gates results in an increased amplitude and a sharper contrast in the modulation potential that may eventually lead to a better-defined bandstructure. Finally, another

deleterious effect for the performance of LSSL devices is the presence of random potential fluctuations in the 2DEG due to ionized donors [8] that add to the possible fabrication imperfections of the gates. The potentials of the relatively low number of donors under the gates cannot be averaged and lead to significant fluctuations that become increasingly important as the region under the gates is depleted by a negative gate bias, due to the reduction of screening.

From the preceeding discussion it is clear that no bandstructure related characteristics should be expected from a LSSL device at $B = 0$. When a perpendicular magnetic field is applied the interplay of the fundamental length scales of the electron system, i.e., cyclotron radius, period of the superlattice and Fermi wavelength, results in a rich magnetoresistance trace at low and moderate magnetic fields. A novel series of oscillations arises from the commensurability of the cyclotron orbit with the period of the superlattice potential [9, 10, 11]. The origin of these novel oscillations is now well understood [12, 13] and they provide valuable information on the effective potential seen by the electrons [14].

1.2 Thesis outline

In Chapter 2 we describe the fabrication process of the LSSL devices studied in this work. The achievement of submicron gate arrays requires the use of high-resolution electron beam lithography. A brief review of the techniques involved and their limitations is also given in Chapter 2. An important aspect of the physical realization of LSSL devices is the choice of the epitaxial material that provides the 2DEG. As we shall discuss in the next chapters, the optimum performance of LSSL devices requires a 2DEG with high mobility and

whose distance to the gates is less than the period of the superlattice. These two properties are mutually exclusive and a compromise has to be found to obtain a satisfactory device. In this work we have used a novel layer structure aimed at reducing the separation between the 2DEG and the surface while retaining values of mobility high enough for our purposes. As a comparison, the same kind of devices were fabricated on conventional High Electron Mobility (HEMT) structures. Both types of epitaxial structures are described in Chapter 2.

Chapter 3 deals with the experimental apparatus and techniques used to perform the magnetoresistance measurements on the LSSL devices. The nature of the experiments demanded cryogenic temperatures and the measurement of low level electrical signals using lock-in techniques.

The reduced dimensions of our devices, imposed by the limitations of the fabrication techniques, allowed us to observe features in the magnetoresistance which, although unrelated to the periodic potential, were nevertheless interesting in themselves. We devote Chapter 4 to discuss magnetosize and wall collision effects measured in plain Hall bars incorporated into our devices for characterization purposes. The origin of the strong negative magnetoresistance displayed by all devices is also discussed.

In Chapter 5 the magnetoresistance data from LSSL devices is presented and analysed. The magnetotransport in these devices is dominated by the semiclassical guiding center drift that results in a new series of oscillations periodic in B^{-1} at low fields that reflect the commensurability between the cyclotron orbit and the imposed periodic potential. The conventional HEMT device exhibits up to thirteen periods of purely sinusoidal oscillations, in good agreement with available theories. The high mobility of the layer allows the

study of the effect in the regime in which Landau quantization starts to take over and interference between commensurability and Shubnikov-de Haas oscillations occurs. The shallow HEMT devices have shown for the first time the presence of a strong harmonic in the magnetoresistance signal that reflects the enhanced contrast of the potential at the 2DEG due to the proximity of the gates. The magnetoresistance oscillations have been extensively studied as a function of gate bias and temperature using Fourier analysis. As a result, sources of 2DEG modulation other than the electrostatic field induced by the gates have been identified and are discused in this chapter.

Chapter 2

Fabrication

2.1 Introduction

A number of technologically demanding fabrication processes is involved in the realization of a LSSL device. The small dimensions involved impose important limitations on the processing and necessitates the use of Electron Beam Lithography (EBL) to define the device structures. Most of the techniques used here in the development of LSSL devices are well known and widely used in the microelectronics industry. Standard processes like lift-off, wet-etching and ohmic and Schottky contacts deposition become increasingly unreliable as the device dimensions are scaled down, severely reducing the yield of the fabrication process and the device-to-device reproducibility. Of great importance is the availability of high quality 2DEG layers especially designed for this type of device. Apart from high electron mobility, good material homogeneity across the wafer and low defect concentrations are desirable to improve device characteristics.

In this chapter we describe the 2DEG layers used in this work and present a review of the techniques that constitute our LSSL device fabrication process.

The physical mechanisms leading to the confinement of a 2DEG gas in the heterostructures and new layer designs will be discussed. The production of arrays of submicron metal gates accounts for an important part of the work. In this chapter we also discuss the high resolution EBL technique, its physical limitations and its application to LSSL device fabrication.

2.2 The GaAs/AlGaAs [1] heterostructure

Modulation-doped GaAs/AlGaAs heterostructures have been used for some time to produce high speed field-effect transistors (MODFET) [15]. In such structures a 2DEG is confined at the interface due to the combined effect of conduction band offset and the attractive potential of the remote ionized donors. The reduced scattering by ionized impurities, the good accord between lattice constants and the low electron effective mass ($m^* = 0.067m_e$) in GaAs make it possible to achieve extremely high values of mobility.

Figure 2.1 shows the layer structure of the conventional HEMT wafer A648 used in this work. In the modulation doping technique the 2DEG electrons are supplied by substitutional impurities located in a Si-doped AlGaAs layer and separated from the 2DEG by an undoped AlGaAs spacer layer. The Si atoms preferentially occupy the Ga sites in the lattice and therefore act as donors. Excess electrons fall into the GaAs due to the conduction band offset, leaving ionized donors in the doped layer that produce a built-in electric field and a bending of the bands. The resulting conduction band structure is shown in figure 2.2. An approximately triangular potential well is formed at the GaAs/AlGaAs interface that confines the electrons in the z-direction.

[1] In all the layers studied in this work the Aluminium molar fraction was $x = 0.3$. We use the notation "AlGaAs" to represent the $Al_{0.3}Ga_{0.7}As$ alloy throughout the text.

170Å GaAs cap
500Å AlGaAs $n_{Si}=8\times10^{17}\,cm^{-3}$
250Å AlGaAs
5000Å GaAs
25.5Å AlGaAs/25.5Å GaAs $\times$101 (Superlattice)
1.1 μm GaAs
(100) GaAs substrate

Figure 2.1: Layer structure of the wafer A648. Modulation doping technique achieves high values of electron mobility by physically separating the ionized donors from the 2DEG. The price to pay is the depth at which the 2DEG is formed (90 nm in this layer) that reduces the efficiency of surface gate devices due to loss of contrast and fringing field effects.

Solving the Poisson equation and imposing the continuity of electric field and potential [2] yields

$$\phi(z) = -\frac{4\pi e N_e}{\epsilon}(z-(c+d+s)) \qquad (c+d<z<c+d+s) \tag{2.1}$$

$$\phi(z) = -\frac{2\pi e N_d}{\epsilon}(z-(c+d))^2 - \frac{4\pi e N_e}{\epsilon}(z-(c+d+s)) \qquad (c<z<c+d) \tag{2.2}$$

where N_d is the donor concentration [3] and N_e the carrier density in the 2DEG. The electrons from the ionized impurities fill the 2DEG until the Fermi level

[2] As a first approximation we neglect the small difference between AlGaAs and GaAs dielectric constants

[3] The donors are assumed to be completely ionized

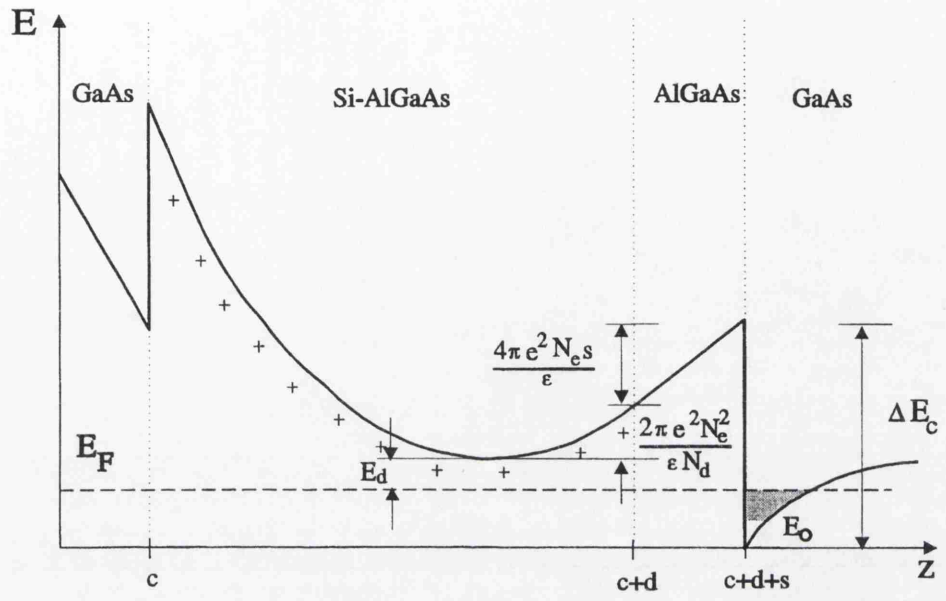

Figure 2.2: Conduction band edge in a standard HEMT layer as obtained from a simplified electrostatic model.

at both sides of the heterojunction is the same

$$E_d + \frac{2\pi}{\epsilon}\frac{e^2 N_e^2}{N_d} + \frac{4\pi e^2 s N_e}{\epsilon} = \Delta E_c - E_0 - (E_F - E_0) \tag{2.3}$$

The relevant energies in equation 2.3 are

- E_d, the binding energy of the electrons to the impurities
- ΔE_c, the discontinuity of the conduction band at the heterojunction, taken to be 0.27 eV, corresponding to an Aluminium molar fraction in the alloy of $x = 0.3$.
- E_0, the lowest energy level in the triangular potential well formed at the heterojunction
- $E_F - E_0$, the Fermi energy relative to the lowest energy level in the well.

The electron density in the 2DEG is given by

$$n_{2d} = \rho(E_F - E_0) \tag{2.4}$$

where $\rho = \pi/(m\hbar^2)$ is the two-dimensional density of states. The value of E_0 depends on the electric field at the heterojunction, $\epsilon E = 4\pi e N_e$, and therefore it is a function of n_{2d}. In the triangular well approximation [16] one finds

$$E_0 = c_0 \left[\frac{(eE\hbar)^2}{2m}\right]^{\frac{1}{3}} \tag{2.5}$$

where $c_0 \approx 2.338$ is the first zero of the Airy function [17]. Substitution of 2.5 into 2.4 yields the relation between Fermi energy and electron density which, substituted into 2.3, determines the electron density in the 2DEG as a function of the layer parameters.

For the layer shown in Figure 2.2, taking $E_d = 0.12\,\text{eV}$, we find $n_{2d} = 2.5 \times 10^{11}\,\text{cm}^{-2}$. The lowest level subband corresponding to this electron density is $E_0 = 40\,\text{meV}$ and the *thickness* of the 2DEG sheet, estimated from the classical turning points of the electron in the triangular well, is $\Delta z \approx 15\,\text{nm}$. In the z-direction the electrons are confined in a region whose dimensions are less than their Fermi wavelength ($\lambda_F = 58\,\text{nm}$) and therefore they exhibit a two-dimensional dynamic behaviour. The doping of the HEMT layers is adjusted so that only the lowest subband is populated at low temperature, thus providing a particularly simple physical system, without the complications of interband or intervalley scattering.

The electron energy relative to the minimum of the subband is given by

$$E(k) = \frac{\hbar^2 k^2}{2m} \tag{2.6}$$

where $m = 0.067 m_e$ is the effective electron mass in GaAs and k the electron wave vector. The Fermi disc is a circle of radius $\sqrt{2mE_F/\hbar^2}$ and the density

of states of the 2DEG [4] results in

$$\rho(E) = \frac{2}{(2\pi)^2} 2\pi k \left(\frac{dE}{dk}\right)^{-1} = \frac{m}{\pi\hbar^2} \tag{2.7}$$

The two-dimensional density of states 2.7 is independent of the energy. At low temperatures all states below E_F are occupied and the Fermi wave vector is related to the electron density by

$$k_F = \sqrt{2\pi n_{2d}} \tag{2.8}$$

At low temperatures only electrons at the Fermi energy contribute to electronic transport. The Fermi wave vector (or equivalently, the Fermi wavelength, $\lambda \equiv 2\pi/k_F$) is a fundamental parameter of the 2DEG that determines the length scale in which quantum effects may be important.

An important aspect of GaAs/AlGaAs heterostructures is the presence of deep donor levels in the AlGaAs. A complete review of *DX* centers in III-V semiconductors has been given by Mooney [22]. Of specific relevance for device performance is the persistent photoconductivity associated with *DX* centers which can be used to change the carrier density of the 2DEG by optical excitation of electrons trapped in the *DX* centers. The increase of electron concentration can have deleterious effects on gated devices since it can lead to the appearance of mobile charge in the spacer layer which is very effective in screening the electrostatic potential of the surface gates. Another problem associated with *DX* centers is the trapping of electrons that results in persistent threshold voltage shifts at low temperature [22].

The persistent photoconductivity effect occurs because the electrons must overcome a considerable potential barrier to recombine, higher than their thermal energy at low temperatures. The change in electronic configuration around

[4] Assuming single subband occupancy

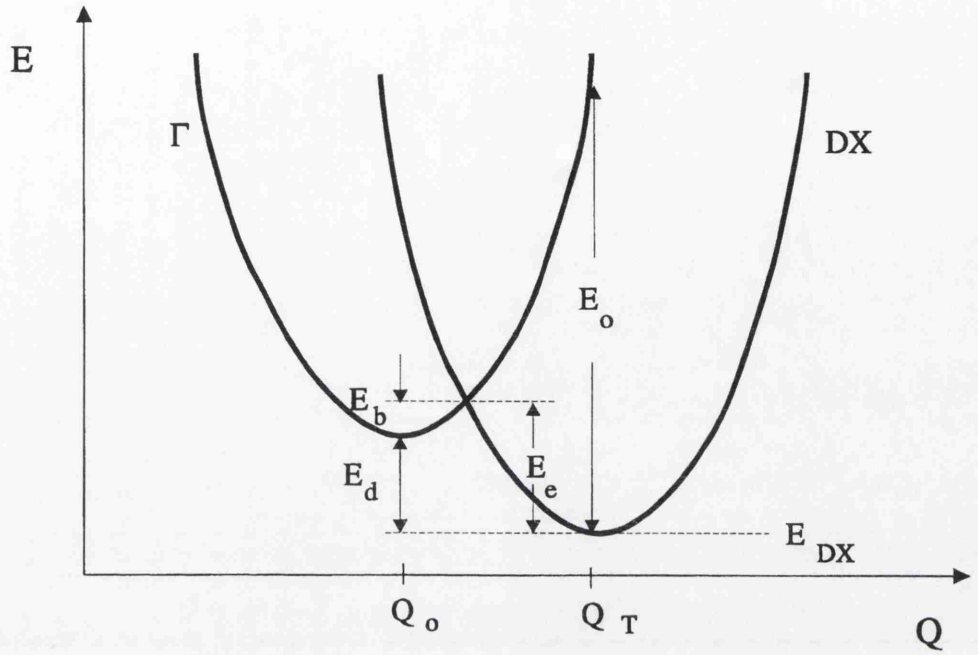

Figure 2.3: Configuration coordinate diagram showing the total energy when the electrons are in the conduction band (Q_0) or bound to the DX level (Q_T). The shift in the value of Q represents a change in the atomic configuration around the impurity atom. The difference between the recombination energy E_e and the capture energy E_b is the donor binding energy E_b. (From Ref. [22]).

the impurity results in a barrier which is higher for detrapping than for binding electrons (see Fig. 2.3). By exposing the sample to illumination at low temperatures the DX centers are ionized (E_0) and the Fermi level rises from a position near the deep donor level to a position close to the conduction band edge. This makes the first term of equation 2.3 negligible and in consequence the value of N_e and the electron density in the 2DEG increase. This carrier density increase is a non-equillibrium situation that can be mantained for long periods of time at low temperatures. The equillibrium population of DX centers can be restored by thermal cycling of the sample up to 150 K.

After processing into Hall bars the samples fabricated out of A648 had

a 2DEG carrier density of $3.6 \times 10^{11}\,\mathrm{cm}^{-2}$ and an electron mobility of $1.2 \times 10^{6}\,\mathrm{cm}^{2}/\mathrm{Vs}$ at $T = 4.2\,\mathrm{K}$, after a brief illumination with an infra-red LED.

2.3 Alternative layer design. Proximity of the 2DEG to the surface

To realise the full potential of laterally gated devices the distance between the surface gates and the 2DEG should be less than the dimensions of the finest features present in the gates. In respect of this limitation, the standard modulation doped heterostructures are far from ideal for studying the effect of nanometric scale gates. Measurement of the quantized conductance in a quantum point contact is a clear example of the importance of the proximity of the 2DEG to the surface. The original experiments [18, 19] were performed on standard HEMT layers and the quantization was observed only at very low temperatures ($T \sim 0.6\,\mathrm{K}$) in a 250 nm wide constriction. Conductance quantization could not be observed at higher temperatures due to thermally induced partial occupancy of several subbands. This limitation could be overcome by using narrower constrictions to increase subband separation and minimise multiple subband occupation; but in a conventional *deep* 2DEG the bias needed to deplete the 2DEG under the gates produces fringing fields that completely deplete the 2DEG before the 1D channel has been formed. Even in wider constrictions, the fringing fields are responsible for a significant smearing of the confining potential. Recently, there has been great interest in novel layer designs to achieve high-mobility shallow 2DEGs [20, 21]. Frost et al. have reported the growth and characterization of a GaAs/AlGaAs heterostructure in which the 2DEG was 25 nm below the surface and the Hall mobility was $1.2 \times 10^{6}\,\mathrm{cm}^{2}/\mathrm{Vs}$. Snider et al. [21] have demostrated the feasibility of a 30 nm

54Å GaAs
100Å AlAs
11.3Å AlGaAs
2.8Å GaAs / δ-doping $4\times10^{12}\,\mathrm{cm}^{-3}$ / 2.8Å GaAs
11.3Å AlGaAs
100Å Al As
5000Å GaAs
25.5Å AlGaAs/25.5Å GaAs $\times$101 (Superlattice)
1.1μm GaAs
Substrate: (100) GaAs

Figure 2.4: Layer structure of wafer A601. The δ-doping plane enclosed in a AlAs/AlGaAs quantum well allows the reduction of the distance between the 2DEG and the surface while preserving the high values of electron mobility characteristic of GaAs/AlGaAs heterostructures.

deep 2DEG to fabricate a 100 nm QPC which exhibited conductance quantization up to $T = 30\,\mathrm{K}$, corresponding to a 10 meV subband separation. All surface gated devices, and LSSLs in particular, should benefit from the proximity of the 2DEG to the surface. This has been the motivation for trying out a novel MBE layer design to fabricate our LSSL devices. The layer structure, following the approach of Frost et al. [20], is shown in Fig.2.4. In this structure the dopant atoms are enclosed in an AlAs/AlGaAs quantum well which helps to avoid parallel conduction by raising the electron energy levels in the well above the X-band in the barrier [20, 23]. The impurity atoms were introduced using the δ-doping technique, with a nominal Si sheet density of $4 \times 10^{12}\,\mathrm{cm}^{-2}$.

δ-doping allows to minimise both the epilayer thickness and the doping levels necessary for the 2DEG formation, being the natural choice for the kind of applications we are interested in. It has to be pointed out, however, that Si migration is an important potential problem in this shallow structures that can significantly degrade electron mobility.

After processing into Hall bars, samples fabricated out of A601 had a 2DEG carrier density of $3.3 \times 10^{11}\,\mathrm{cm}^{-2}$ and a mobility of $6.3 \times 10^{5}\,\mathrm{cm}^2/\mathrm{Vs}$ at $T = 4.2\,\mathrm{K}$ in the dark. The Shubnikov-de Haas oscillations showed good zeros. After illumination with an infra-red LED there was no significant change in the electron density in the 2DEG whereas the mobility increased up to $7.8 \times 10^{5}\,\mathrm{cm}^2/\mathrm{Vs}$. The increase in mobility is probably due to the generation of charges trapped at the AlAs/AlGaAs interface that contribute to the screening of the ionized impurities.

2.4 Fabrication Processes

The microelectronics industry has developed processes for the fabrication of planar electronic devices which can be adapted for the realization of experimental mesoscopic devices. The generalized use of metal-semiconductor contacts [24] in commercial devices has given rise to a well established technology for Schottky gate and ohmic contact deposition.

2.4.1 Pattern definition. Electron Beam Lithography

Optical lithography is the most widely used technique for lateral patterning of micrometric structures. Highest resolution is obtained by projecting a mask

with a magnified image of the device is projected by a demagnifying optical system on the semiconductor previously coated with a photosensitive resist layer. The resolution of this technique is limited by the diffraction of light. The minimum line separation that can be achieved is given by [25] $\Delta x \approx \lambda / \sin\theta$, where λ is the wavelength of the light used and $\sin\theta$ is the numeric aperture of the optical system.

In e-beam lithography the pattern is defined by a scanned electron beam which is focused on the substrate by a series of electromagnetic lenses. Diffraction problems are not important in practice and the resolution is limited by the spreading of the beam over areas much larger than its original diameter by scattering in the resist and suubstrate. These effects can be minimised using the high-resolution nanolithography techniques that are discussed below. E-beam lithography, now extensively used for the generation of optical lithography masks, is especially suitable for the fabrication of experimental devices which usually require frequent modifications. The devices are exposed directly on the substrate eliminating the need for mask generation so that changes in the design can be effected immediately.

All the lithography work presented in this thesis was executed on a modified Scanning Electron Microscope Philips PSEM500. Fig. 2.5 shows a block diagram of the EBL system. The main additions to the commercial SEM are

- Digital scan generator
- Automatic focus adjustment
- Automatic alignment
- Beam blanking system
- Beam current measuring system

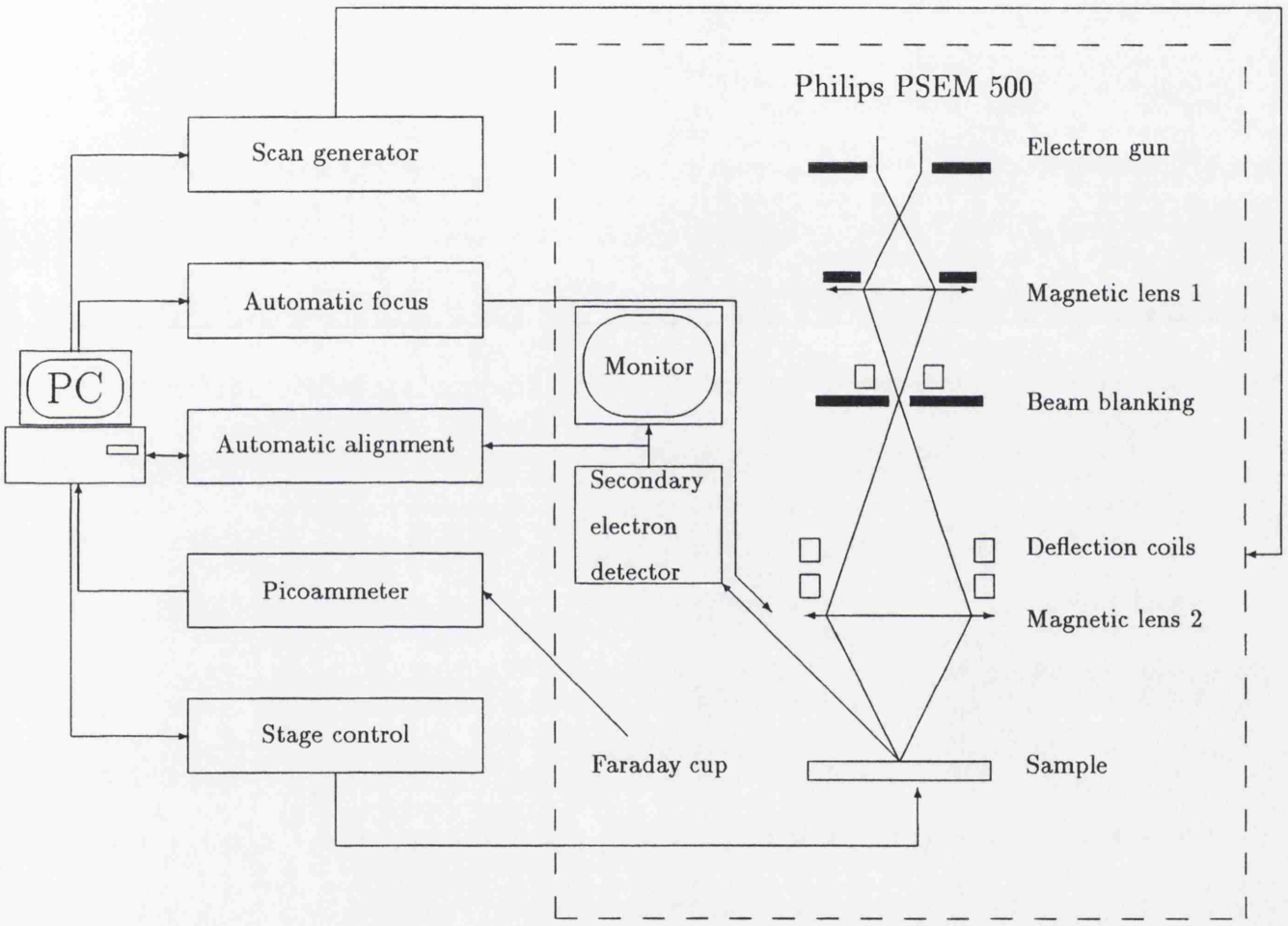

Figure 2.5: Block diagram of the e-beam lithography system based on a modified Scanning Electron Microscope Philips PSEM500.

High beam energy is an important factor in electron beam nanolithography since it reduces both the spread of the beam as it penetrates through the resist and the effect of the back-scattered electrons. The system described here uses an accelerating voltage of 50 kV. The spot size must be smaller than the smallest feature so that the pattern can be filled by multiple passes to obtain better defined edges. At the same time the beam current has to be sufficient to allow accurate setup and alignment. The beam blanker has to be very fast and effective, with high values of attenuation and a response time less than the time required to expose a pattern pixel so that the finest features can be defined without significant distortion

Electron beam lithography resists are classified in two broad groups

- Positive resists, that dissolve preferentially during development in regions that have been exposed
- Negative resists, that dissolve preferentially in unexposed regions

The most widely used resists in EBL consist of organic long chain polymers. The irradiation of positive resists by an electron beam produces chain scissions that result in a significant reduction of the average molecular weight of the exposed areas. In negative resist exposure generates cross-links between adjacent molecules. In general negative resists exhibit poorer resolution, tend to swell during development, and their complete removal from the substrate is difficult. Therefore, positive resists are preferred for high resolution lithography.

For the fabrication of the LSSL devices we used PMMA (Poly-methyl methacrylate), an organic polymer formed by long chains of the monomer

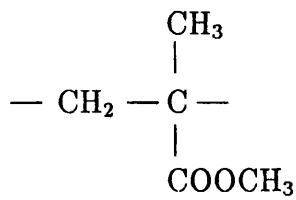

Irradiation by an electron beam causes scissions in the long chains so that there is a significant reduction of the average molecular weight of the exposed areas. The solubility of PMMA in a 1 : 1 (in volume) of MIKB (methyl isobutyl ketone) : IPA (iso propyl alcohol) solution is inversely proportional to the square of the average molecular weight. The development of the sample in MIKB : IPA for 50 s at 23 °C dissolves preferentially the exposed regions and leaves a PMMA mask on the unexposed areas.

The resolution limit of EBL is determined by the difficulty of confining the energy of the beam in a region comparable to the spot size. As the electron beam passes through the resist layer it broadens due to forward scattering. This effect can be minimised by using electrons accelerated to higher energies (50 keV or 100 keV) in conjunction with reduced resist layer thickness. For the feature sizes used in this work forward scattering is not a serious limitation to the lithographic resolution. High energy secondary electrons generated as the beam passes through the resist cause an additional exposure to an area surrounding the actual position of the beam which cannot be reduced by using thinner resists. However the effect is not significant at the length scales that we use.

Electrons back-scattered from the substrate pose a more serious problem to the definition of arrays of submicron gates. These electrons expose the resist film over an area with a characteristic diameter of approximately twice the penetration depth of the electrons in the substrate. In areas with a high packing density of small structures this effect results in an inhomogeneous background that can severely distort the pattern exposure. This problem, known as the *proximity effect*, can be partly compensated by varying the dose given to each pattern so that all exposed regions receive the same energy density. In some cases it is possible to expose sacrificial patterns to ensure a more homogeneous

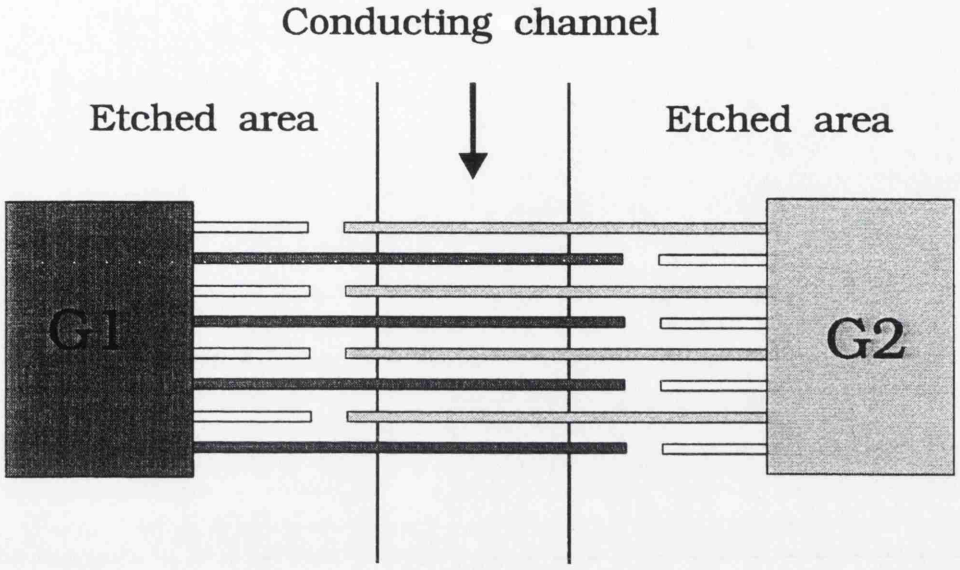

Figure 2.6: Interdigitated gate structure that allows differential biasing of the gate arrays. The sacrificial fingers are needed to keep the dose received by each finger constant along its length (proximity effect).

background exposure. This is illustrated by the interdigitated gate structure that makes up our LSSL devices (see Fig. 2.6). The proximity effect can be substantially reduced by using higher acceleration voltages. Beams of higher energy electrons penetrate deeper in the substrate and the back-scattered electrons spread over a larger region, giving rise to a much more uniform background with lower concentration of back-scattered electrons in the pattern region. All the lithography described in this work was performed at 50 keV. The use of ever increasing accelerating voltages may not be desirable since e-beam may induce some damage in the 2DEG material. In fact, some of the LSSL devices studied show a substantial decrease of mobility in the gated region that cannot be accounted for by a built-in electric field due to the presence of the gates. The high exposures ($\approx 500\,\mu\mathrm{Ccm}^{-2}$) necessary to define the gates across the conducting channel may produce defects in the semiconductor that

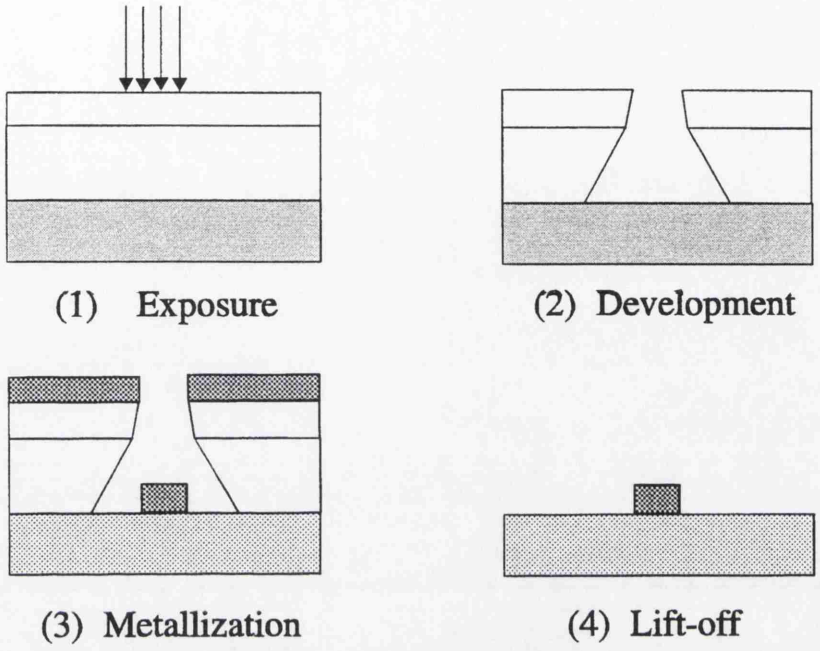

Figure 2.7: Illustration of the pattern transfer process. (1) A bilayer resist film is exposed by a 50 keV electron beam that causes an increase of solubility of the resist. (2) The exposed areas are cleared in the development process. (3) Metal is evaporated on the sample. (4) The resist is dissolved in acetone so that only the metal adhered to the semiconductor is left.

trap electrons and degrade the 2DEG characteristics.

2.4.2 Pattern transfer. Resists and lift-off

In practice, the fabrication of nanometric devices is not ultimately limited by lithography resolution but by the ability to successfully transfer the patterns into metal gate structures. This is achieved by a process of metallization and lift-off (see Fig. 2.7). Lift-off in acetone dissolves the remaining resist film so that only the metal adhering to the semiconductor surface is left. An

undercut resist profile, as illustrated in Fig. 2.7, favours lift-off. This profile is achieved by using a double PMMA layer with different molecular weights. The bottom layer, in contact with the semiconductor surface, has a lower average molecular weight and therefore higher sensitivity. The top layer, with a higher molecular weight and consequently less sensitivity, effectively acts as the metallization mask. The use of double layer resists is essential in high resolution nanolithography since

1. The bottom layer provides adequate thickness to facilitate lift-off.

2. The top layer can be made very thin, thus reducing the broadening of the beam as it passes through the resist. Moreover, it is least affected by primary forward scattering.

3. Overexposure of the bottom layer is not critical and contributes to the undercut profile that makes lift-off easier.

4. The patterns are defined by the top layer; as it is less sensitive and separated from the substrate the proximity effect is noticeably reduced.

We used two different sources of PMMA: 180000 average molecular weight PMMA supplied by BDH Chemicals Ltd. and 360000 average molecular weight PMMA(ELVACITE) supplied by DuPont Co. The PMMA is dissolved in Clorobenzene and spun over the sample at 5000 rpm to form an homogeneous film whose thickness is controlled by the concentration of the PMMA solution. The samples are then baked at 180 °C for about 30 min. to eliminate the solvent completely. At the same time the PMMA undergoes a glass transition that hardens and smooths the film. Gate levels, where hardness of the resist is important, and isolation levels, where good adhesion of the resist is essential, usually require longer periods of baking. The best results in the fabrication of arrays of 130 nm gates were obtained using 4% BDH, baked for 60 min followed

by 2.5% ELVACITE, and then baked overnight.

2.4.3 Deoxidation and Metal-Semiconductor Contacts

On the exposed surface of GaAs there is a native oxide layer a few nanometers thick. It is customary to deoxidize the samples in a 1 : 4 (in volume) of HCl : H_2O solution for 30 s. in order to remove the oxide layer and obtain better metal-semiconductor contacts. However, in view of the fact that the process is carried out in an open atmosphere, the oxide layer grows again very quickly and consequently the deoxidation process yields at best a semiconductor surface less dependent on the history of the sample. It has been found that shallow HEMTS are very sensitive to the deoxidation etch since it can etch deep enough to deplete the 2DEG and make the electric contact to the 2DEG impossible. Therefore, only a very light etch (1 : 10 (in volume) of HCl : H_2O for 10 s.) is performed on these materials prior to ohmic contact deposition.

Another delicate step is the gate level deoxidation. Due to the dimensions of the gates it is not good practice to deoxidize the sample prior to gate metallization. We found that the etch is highly non uniform since the acid tends to form pools along the resist groves and the complete removal of the acid is difficult. The approach adopted here has been to carry out a very light etch (1 : 10 (in volume) of HCl : H_2O for 5 s.) prior to spinning resist and performing the metallization immediately after development. Any potentially damaging cleaning process such as argon glow discharge or the use of oxigen ashing was carefully avoided.

The evaporation of thin metal films in a high vacuum system produces stable and reproducible contacts that are extensively used in microelectronics.

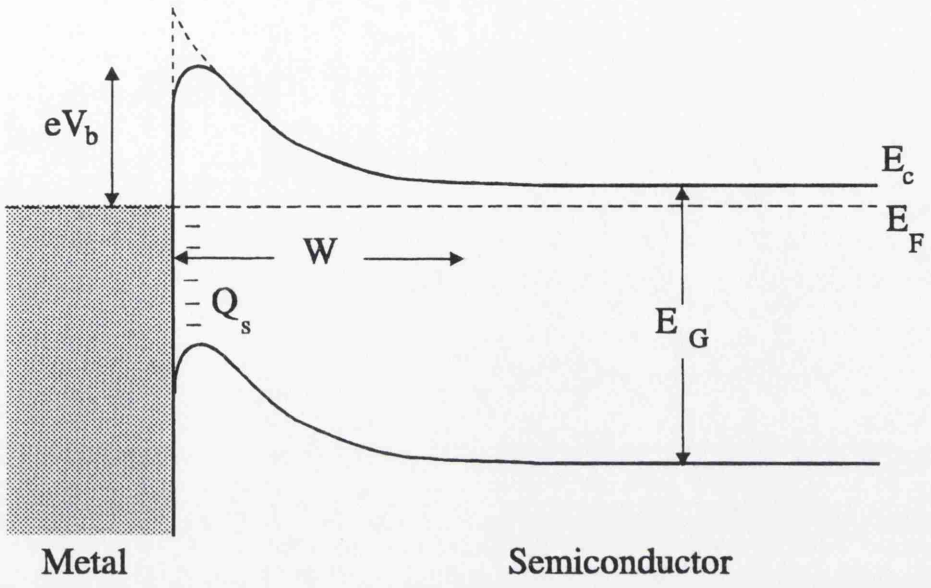

Figure 2.8: Band diagram in a metal-semiconductor union illustrating the Schottky barrier formation and the correction to the barrier height due to the Schottky effect.

In the fabrication of LSSL devices two kinds of contacts were used:

- Schottky contacts. These are formed when a metal comes into contact with a semiconductor and a transfer of electrons from the semiconductor to the metal occurs as the respective Fermi levels are forced into alignment. The extra negative charge on the metal surface is compensated by a positive charge in the semiconductor as conduction electrons recede and leave uncompensated ionized donors in the depletion region w. The built-in electric field bends the bands and a Schottky barrier with rectifying properties is formed at the metal-semiconductor interface (Fig. 2.8). The presence of a thin native oxide layer on the semiconductor does not affect the electron transport since electrons can easily tunnel through. The Schottky barrier height is roughly independent of the metal that forms the contact because of the presence of a high density of interface

states in the metal-semiconductor junction that are responsible for the Fermi level pinning approximately in the middle of the energy gap. Therefore a Schottky barrier of the order of 0.7 eV is formed between GaAs and a metal. The effective barrier height seen by an electron is lowered by the image force due to the presence of the metal sheet.

The use of Schottky contacts allows reversible control of the 2DEG density by electrostatic means. When the metal is negatively biased with respect to the semiconductor a further negative charge depletion occurs in the semiconductor. If the Schottky gates are defined on the surface of an epitaxial 2DEG heterostructure the field effect can effectively control the 2DEG carrier density or even completely deplete the regions of the 2DEG underneath the gates, as has been demonstrated by numerous experiments [7, 26, 27, 28], most notably by the measurement of quantized conductance in a quantum point contact [18]. Surface Schottky gates can also be used to impose a weak periodic modulation on a 2DEG [5, 10, 14, 29]. However, as we shall discuss in Chapter 5, in complex epitaxial 2DEG layers such as A601 (Fig. 2.3) the effect of the gate bias on electron transport in the 2DEG is not simply a consequence of the straightforward electrostatics considered above. The redistribution of mobile charge in the semiconductor layers that separate the gates and the 2DEG has important consequences on the electron mobility and has to be taken into account to explain the device characteristics [14].

The metallization used in the gate arrays consisted of 15 nm Ti and 15 nm Au. The gate metallization is the last level of the LSSL device. This approach avoids Schottky contact characteristics degradation due to thermal cycling in further processing.

- Ohmic contacts. As mentioned above, metal-semiconductor contacs generally show rectifying characteristics. To obtain electrical contact to the 2DEG the doping of the semiconductor has to be locally modified. Ohmic contacts are effected by thermal diffusion of metals and dopants in the contact area. The ohmic contacs used in the LSSL devices are formed by:

  - 8 nm of Ni, acting as adhesion layer and diffusion barrier
  - 120 nm of Ge and 135 nm of Au. These metals, in eutectic proportion, diffuse into the semiconductor to form the contact
  - 50 nm of Ni, acting as a diffusion barrier
  - 45 nm of Au, capping layer to avoid oxidation and improve the connection to the bonding pads

  The electric contact is properly formed after thermal annealing at 360 °C in an argon atmosphere for 30 s.

2.4.4 Isolation

The devices were structured into a double Hall bar (see Fig. 2.9). The electrical isolation of the conduction channel was carried out by means of wet etching. The isolation pattern, consisting of the areas outside the Hall bar that have to be removed, together with a system of trenches around the contacts, is defined by e-beam lithography. After development a mask of PMMA (10% BDH/8% BDH) protects the Hall bar and the contact area. The sample is chemically etched in a solution 1000 : 20 : 7 (in volume) of H_2O : NH_4^+ : H_2O_2 at 6 °C for 30 s. The hydrogen peroxide oxidizes the semiconductor whereas the ammonia solution dissolves the oxide layer that forms in the exposed areas. The low temperature favours a smooth and controlled etch. The depth of the etch is the minimum that ensures electrical isolation between adjacent devices,

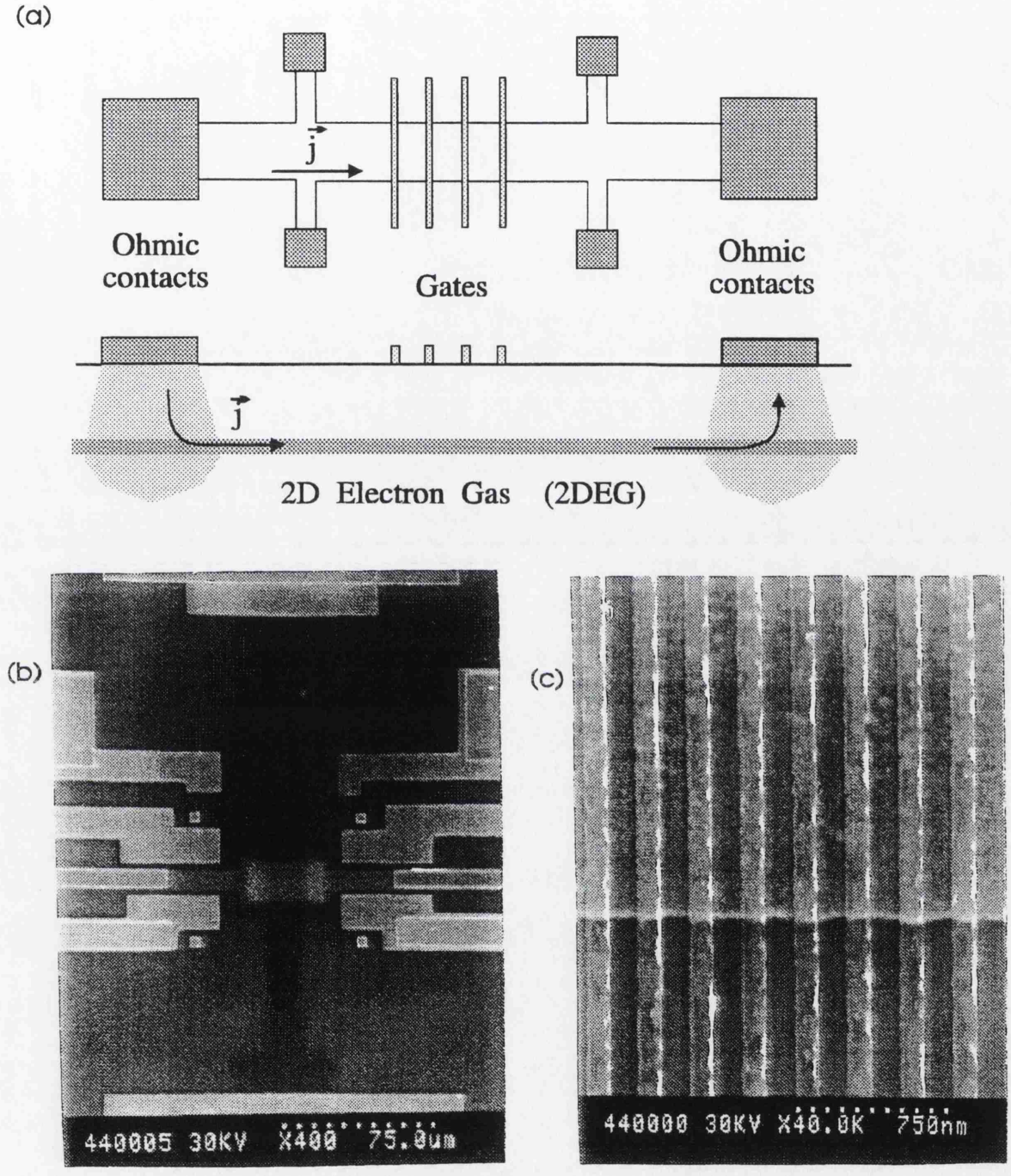

Figure 2.9: (a) Schematic representation of the active part of a LSSL device. (b) SEM micrograph of a LSSL device at $\times 400$ (c) SEM micrograph at $\times 40000$ showing the detail of the array of metal fingers that make up the gates.

with leakage currents well below 1μA for bias up to 1 V.

2.4.5 Device design

The device dimensions are limited by the size of field of the electron microscope, which in turn is governed by the magnification setting. The gate array is exposed at $\times 2500$, and at that magnification the microscope can only write over an area of $56\,\mu$m $\times\, 42\,\mu$m . The metal fingers cover an area 41μm long and 21μm wide (corresponding to 80 periods of a 265 nm-period grating). The gate arrays are designed as two sets of interdigitated fingers that can be biased independently.

The conducting channel is structured as a double Hall bar. Three pairs of ohmic contacts allow 4-terminal measurements of any component of the resistivity tensor. Each Hall bar is $14\,\mu$m wide and $32\,\mu$m long. The gates are defined across one of the Hall bars, overlapping the etched conduction channel, perpendicularly to the current flow. The second unpatterned Hall bar is used for in-situ characterisation of the 2DEG. The device geometry is very versatile and it can be readily adapted to other measurement set-ups, such as non-local resistance configurations [30].

Experimentally it is the longitudinal resistance, R_{xx}, that we measure directly, not the resistivity, ρ_{xx}. These quantities are related by

$$R_{xx} = \frac{L}{W}\rho_{xx} \tag{2.9}$$

where L and W are, respectively, the lenght and the width of the 2DEG region. For the detection of small variations in ρ_{xx} a large aspect ratio L/W would be desirable. In practice, the value of L is limited by the area that it is possible to cover with the gratings. We have chosen $W > l$, where l is the

electron mean free path, to minimise the effect of wall collisions. Most of the channel area between voltage probes is covered with the gratings so that the effect of the parasitic resistance of the series 2DEG is minimised.The metal fingers run across the etched Hall bar and over 45 nm thick connecting pads with continuity.

In the presence of a perpendicular magnetic field the ohmic contacts short-circuit the Hall field so that near the contacts the current is not parallel to the channel axis [31]. The current contacts in our devices are located 80 μm away from the nearest voltage probe. The ohmic contacts extend from the 2DEG material over to the etched region to avoid Corbino-type currents around the contacts.

In Table 2.1 we give a summary of the fundamental length scales of the devices studied in this thesis. A comparison of the device dimensions with the electron mean free path situates the operation of the LSSL devices in a quasi-ballistic regime, in which wall collisions and internal impurity collisions are equally important in determining the channel resistance. It is generally considered that structures defined by wet-etching present predominantly specular wall reflections that have no effect on the resistance of the channel [32]. However, some degree of diffuse scattering is also present and as we shall see in Chapter 4 it has measurable effects on the magnetoresistance of our devices.

Comparison of magnitudes in table 2.1 with the typical dimensions of our devices (W, a) show that $l \sim W$ and, for moderate fields ($B < 1\,\mathrm{T}$), $R_c \sim a$. This regime leads to interesting commensurability effects that will be studied in Chapters 4 and 5. The period of the gratings in our devices is still too large compared with the electron Fermi wavelength for the observation of quantum effects of the periodic potential on electron transport.

Table 2.1: Fundamental length scales in the devices studied.

Parameter	Expression	A648	A601	Units
Cyclotron radius	$R_c = c\frac{\hbar k_F}{eB}$	$\frac{100}{B}$	$\frac{92}{B}$	nm Tesla
Magnetic Length	$l_m = \left(\frac{\hbar c}{eB}\right)^{\frac{1}{2}}$	$\frac{25}{B^{\frac{1}{2}}}$	$\frac{25}{B^{\frac{1}{2}}}$	nm Tesla$^{\frac{1}{2}}$
Mean free path	$l = v_F\tau$	12	6	μm
Fermi wavelength	$\lambda_F = \frac{2\pi}{k_F} = \sqrt{\frac{2\pi}{n_{2d}}}$	42	45	nm
Diffusion constant	$D = \frac{1}{2}v_F^2\tau$	1.7×10^4	7.8×10^3	cm^2/s
Thermal length	$l_T = \left(\frac{\hbar D}{k_B T}\right)^{\frac{1}{2}}$	$\frac{3.6}{T^{\frac{1}{2}}}$	$\frac{2.4}{T^{\frac{1}{2}}}$	μm K$^{\frac{1}{2}}$

In Table 2.2 we present the complete fabrication process of a LSSL device.

Table 2.2: Fabrication steps of a LSSL device by E-beam lithography, metallization and lift-off

LSSL fabrication steps					
Level	Preparation	Resists	Developer	Metallization	Other process
Alignment	Clean in trichloroethene and in acetone in ultrasonics bath	10%BDH 4%ELV	1:2 MIBK:IPA	33nm Ti 160nm Au	
Isolation	Clean in trichloroethene and in acetone in ultrasonics bath. Use adhesion promoter	10%BDH 4%BDH (baked overnight)	1:1 MIBK:IPA		Etch 1000:20:7 H_2O : NH_4^+ : H_2O_2 , 30 s. at 6C
Ohmic	Clean in warm acetone	15%BDH 4%ELV	1:1 MIBK:IPA	8nm Ni 120nm Ge 135nm Au 50nm Ni 45nm Au	Anneal at 360 °C , 30 s.
Connecting pads	Clean in warm acetone	8%BDH 4%ELV	1:2 MIBK:IPA	15nm Ti 30 nm Au	
Bonding pads	Clean in warm acetone	15%BDH 4%ELV	1:1 MIBK:IPA	30nm Ti 250nm Au	
Gates	Clean in trichloroethene and in acetone in ultrasonics bath. Deoxidise in 1:10 HCl:H_2O, 5s.	4%BDH 2.5%ELV. Bake overnight	1:2.5 MIBK:IPA	15nm Ti 15nm Au	Soak in acetone, several hours. Elliminate lift-off film very gently with squeezed acetone

Chapter 3

Experimental techniques

The experimental study of electron transport in a 2DEG requires exceptionally low temperatures. On the one hand the highest values of electron mean free path are achieved only at low temperatures, where $k_B T$ is less than the acoustic phonon energy and the scattering is dominated by elastic collisions with remote ionized impurities that are ineffective in limiting the electron mobility. On the other hand the thermal broadening of the Fermi level ($\sim 2k_B T$) must be much less than the separation between the electronic states under study. However, as we shall see in Chapter 5, the semiclassical resonances associated with the periodic potential are quite robust and can be observed for temperatures up to 10 K without significant degradation.

An external magnetic field, applied perpendicularly to the 2DEG plane, introduces a new fundamental length in the system: the cyclotron radius, R_c, at moderate fields, or its equivalent, the magnetic length, l_m, at quantizing magnetic fields. The magnetic fields necessary to enter into the classical resonance regime between R_c and a are quite moderate ($B < 1\,\mathrm{T}$).

We studied our LSSL devices in linear response regime, working with very

low levels of excitation to avoid the generation of *hot electrons* with energies well above the Fermi level. At $T = 70\,\mathrm{mK}$ the thermal energy $k_B T$ is only 6 μeV and therefore voltages across the device must be kept below that level. Severe noise problems are associated with low level measurements of this kind. The signal to noise ratio can be improved using lock-in techniques.

3.1 Cryogenic equipment

For the low temperature mesurements we used an *Oxford Instruments Kelvinox* He^3/He^4 dilution refrigerator. The system consists of a He^4 cryostat fitted with a superconducting 12 T magnet and the refrigerator circuit itself, mounted on an insert. The refrigeration cycle is based on the properties of the solutions of He^3 in He^4. Below 0.87 K the solution separates into two phases: a concentrated solution of He^3 in He^4 and a denser diluted solution. Given that the vapour pressure of He^3 is much larger than that of He^4, by pumping on the diluted phase He^3 can be removed from the solution. Then, to maintain the equillibrium of phases, He^3 from the concentrated solution has to dissolve in the diluted solution. This is an endothermic process that keeps the sample cell at temperatures below 100 mK. The He^3 removed from the diluted phase is then liquefied and pumped to the concentrated phase in a close circuit so that once stabilized the refrigeration cycle can be maintained for a long period of time. The temperature of the sample is monitored using a calibrated Ruthenium oxide resistor.

The same cryostat could be fitted with a variable temperature gas flow insert for temperature dependence measurements. In that system, a continuous flow of He^4 through the sample space is maintained to adjust the temperature of the sample. An *Oxford Instruments* intelligent temperature controller sup-

plies a resistor with the right ammount of current to stabilize the temperature at the desired value. A calibrated Rh-Fe resistor is used to monitor the sample space temperature and acts as a sensor for the temperature controller. The system has been used in this operation regime for measurements in the temperature range $4.2\,\mathrm{K} < \mathrm{T} < 40\,\mathrm{K}$. By filling the bottom of the VTI with liquid He^4 and pumping on it, the He undergoes a phase transition to its superfluid phase and the temperature is further reduced to 1.2 K. With fine tuning of the pressure and the He flow the temperature range between 1.2 K and 4.2 K can be covered as well.

The samples are mounted on a standard 18 contact ceramic capsule that fits in a specially designed spring-loaded socket (see Fig. 3.1). A copper cylinder pressed against the back of the capsule by a Be-Cu spring ensures a good thermal contact between the sample and the mixing chamber. The devices were connected to the capsule pins with gold wire using an ultrasonic friction bonder.

The cryostat is equipped with a superconducting solenoid sitting in a bath of He^4 that can generate magnetic fields up to 12.5 T. The sample is placed in the center of the magnetic field. When the refrigeration cycle is not in operation the sample space is below the He^4 level and the system can be used for measurements at $\mathrm{T} = 4.2\,\mathrm{K}$.

3.2 Magnetoresistance measurements

Low-level magnetoresistance measurements were performed using four-terminal lock-in techniques. In Lock-in or Phase Sensitive Detection (PSD) the sample response to an ac signal is measured using a very narrow detection bandwidth

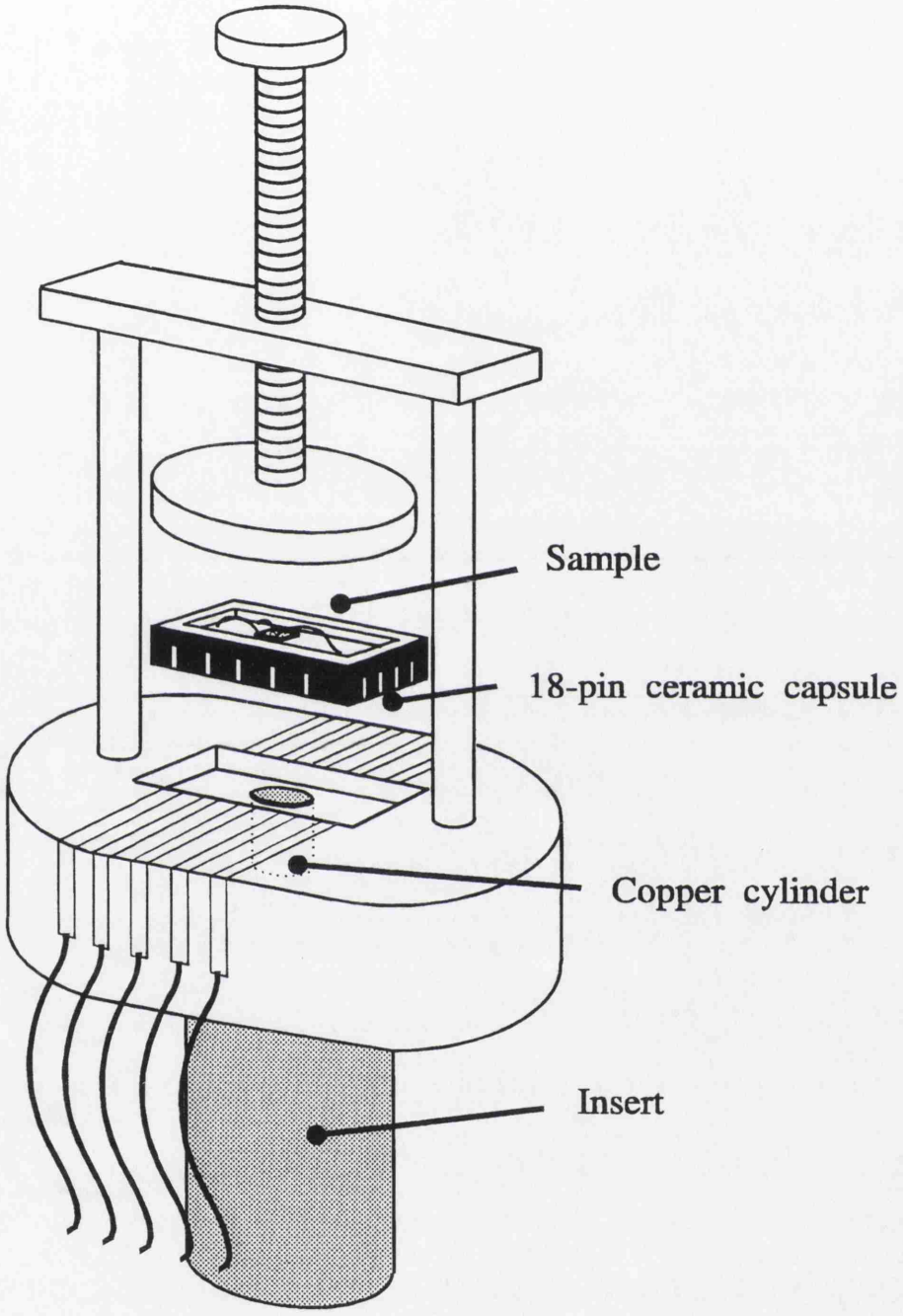

Figure 3.1: Sample mounting on a specially designed socket that was fitted to the dilution refrigerator insert.

centered on the excitation frequency. A low frequency ($\nu = 18\,\mathrm{Hz}$) sinusoidal current is fed through the device. The potential drop across the device is amplified, wide-band filtered and synchronously detected using the reference signal. The PSD circuit consists basically of a multiplier circuit and a low-pass filter. The output of a PSD is linear in the signal amplitude at the selected frequency:

$$V_{PSD} = \frac{V_{ref} V_s}{2} \cos\phi \tag{3.1}$$

For signals at different frequencies, the output of the PSD is an oscillating signal of frequency $\Delta\omega$:

$$V_{PSD} = \frac{V_{ref} V_s}{2} \cos\Delta\omega t \tag{3.2}$$

that is rapidly attenuated by the low-pass filter. A review of PSD techniques and their application to electric and optical measurements can be found in reference [33]. It must be stressed that Phase Sensitive Detection improves dramatically the signal to noise ratio but *it does not reduce the actual noise level in the sample* which can be heated well above fridge temperatures by pick-up noise. The measurement circuit has to be optimised to eliminate as much as possible the sources of electrical noise. To avoid the creation of earth loops the shields of the measuring circuit are grounded at a single point at the cryostat head and all the pumping lines have been electrically insulated.

It was found that the digital measuring equipment was an important source of the radio frequency noise that heats up the 2DEG above fridge temperatures. The inclusion of radio-frequency Π filters in the Lock-In amplifier input terminals improved significantly the noise level in the sample.

A schematic diagram of the measuring circuit is shown in Figure 3.2. The cryostat with the sample is located inside a screened room. The electronic instrumentation consisting of three EG&G PARC 5210 Lock-in amplifiers and

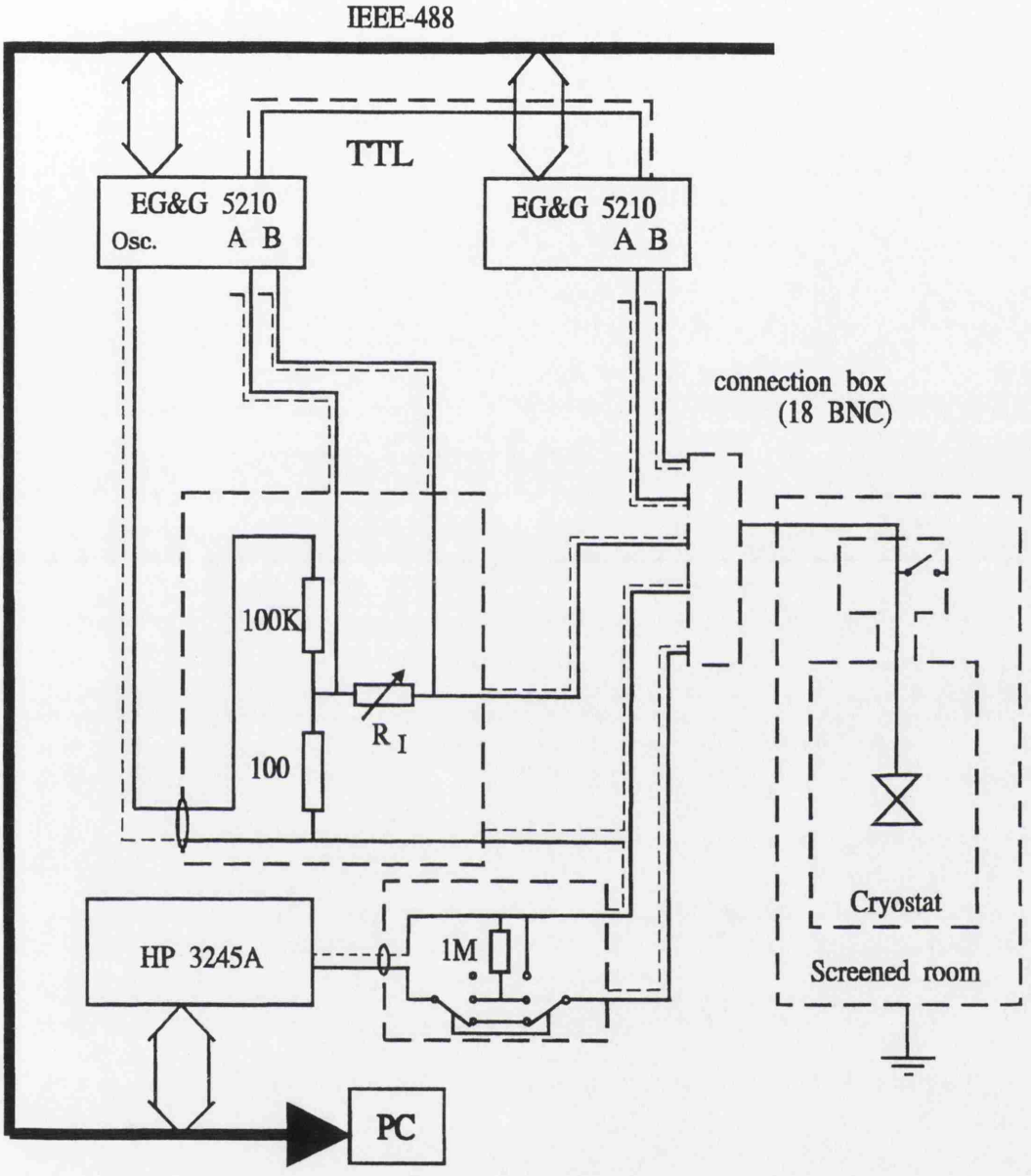

Figure 3.2: Schematic diagram of the measuring system. The cryostat with the sample is located inside a screened room in order to minimise pick-up noise.

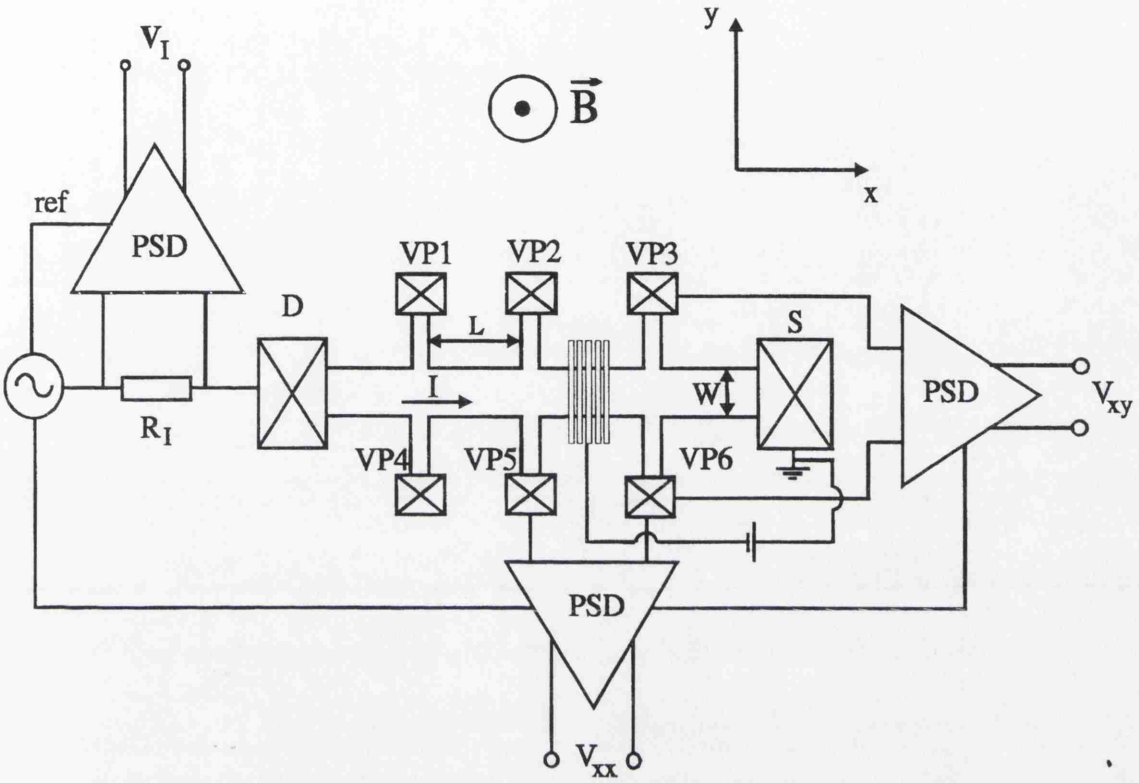

Figure 3.3: Schematic diagram of the configuration used in magnetoresistance measurements. The experimental set-up allows the simultaneous measurement of current and voltage drops across two different pairs of probes. Gates are biased wih respect to the source contact, which is used as a virtual ground.

two Hewlett-Packard 3245A universal voltage sources is outside the screened room. The measuring system is computer controlled by a PC via an IEEE488 interface. The excitation signal is provided by the internal oscillator of one of the Lock-in amplifiers that is attenuated in a 1:1000 voltage divider. A roughly constant current is fed to the device through a series resistor R_I. The voltage drop measured across R_I allows precise determination of the current. Current is passed between contacts D and S (see Fig. 3.3), with contact S acting as the circuit virtual ground. The gates can be shorted to S ($V_g = 0$) or maintained at a fixed potential using the HP 3245A voltage source.

It has been found that the LSSL devices are extremely sensitive to electrostatic discharges. Due to the small separation between the metal fingers electrostatic charging or spurious voltages can give rise to electric fields high enough to produce electrical rupture. A box of switches at the cryostat head allowed each of the sample leads to be grounded so that when loading the sample or when switching on and off electrical equipment *all* the device contacts are safely kept at ground potential. A 1MΩ resistor in parallel with the gates has been fitted to avoid charge build-up in the gates.

The current to energize the superconducting solenoid is provided by an *Oxford Instruments* power supply unit, which is computer controlled via a RS232 interface. The magnetic field resolution of this equipment is of the order of 1 mT. The current is linearly varied until the field reaches the target value. The ramp rate can be selected: we used 0.3 T/min in measurements up to 12 T and 0.1 T/min or 5×10^{-2} T/min in more precise measurements in the range $0 \leq B \leq 2$ T. For ramp rates ≤ 0.1 T/min the magnetic hysteresis of the coils was found to be negligible.

All the measurements were controlled by a PC running the Turbo-Pascal program IMS3 written by Mahfuzur Rahman. The computer successively takes the readings of the Lock-In amplifiers as the magnetic field is ramping to the target field value. The measuring configuration can be readily changed to perform gate bias sweeps.

Chapter 4

Magnetotransport in a 2DEG

4.1 Introduction

In this chapter we study the magnetotransport phenomena in an unmodulated two-dimensional electron gas in the presence of a perpendicular magnetic field. This study, interesting in itself because of the small dimensions of the samples which made possible to observe classical-size effects [32], yields useful information about the electrical characteristics of the 2DEG and serves as a point of reference to identify some features present in the LSSL magnetoresistance traces that are not associated with the periodic modulation.

We shall see that for moderate magnetic fields $B < 1$ T a semi-classical model for the electron dynamics is perfectly adequate for the description of commensurability resonances. This model does not explain, however, the strong negative magnetoresistance observed at very low temperatures and low magnetic fields. As its temperature dependence suggests, the origin of this negative magnetoresistance is quantum interference. The electron-electron interaction models developed by Altshuer and Aronov [34], Finkel'stein [35] and Fukuyama et al. [36], and studied experimentally by K. K. Choi et al. [37], are in reaso-

nable agreement with the negative magnetoresistance observed in our samples.

Stronger magnetic fields cause the quantization of electronic states and the semi-classical model is no longer valid. The formation of Landau levels and the coexistence of extended electronic states and localized states associated with impurities give rise to the quantization of Hall conductivity [38], one of the most significant discoveries of Solid State Physics in recent years. The Hall conductance shows *plateaux* at integer multiples of $e^2/h = (25.7\,\mathrm{k}\Omega)^{-1}$ with an error smaller than three parts in ten millions, independently of the sample geometry and the nature of the contacts. Quantization is reflected in the longitudinal resistivity as a series of oscillations periodic in B^{-1}, the well-known Shubnikov-de Haas oscillations [39]. In the quantum Hall effect regime the Hall *plateaux* correspond to *zeros* of the longitudinal resistivity, i.e., the system becomes non-dissipative. The Shubnikov-de Haas oscillations are used for the characterization of the 2DEG. The carrier concentration can be extracted from the periodicity and an analysis of the amplitudes gives information about the scattering time. The presence of a parallel layer of mobile charge, deleterious to gated device performance, can be detected as a rising residual resistance in the quantum Hall effect regime.

4.2 Semi-classical approximation

In the regime $\hbar\omega_c < 4k_BT$ magnetic quantization is not important and electron dynamics can be described by a semi-classical model in the relaxation time approximation. On average, the electrons travel a distance $l = v_F\tau$ before undergoing a collision, from which they emerge with an isotropic velocity distribution. Between collision events, in presence of a weak electric field, the

electrons acquire an average drift velocity

$$\mathbf{v} = -\frac{e\tau}{m}\mathbf{E} \equiv -\mu\mathbf{E} \tag{4.1}$$

where we have defined the electron mobility $\mu = e\tau/m$. The current is obtained summing the contributions of all the electrons

$$\mathbf{j} = \frac{ne^2\tau}{m}\mathbf{E} \equiv \sigma_o\mathbf{E} \tag{4.2}$$

where σ_o is the conductivity of the 2DEG.

Only electrons with energies near the Fermi level, E_F, contribute to electronic transport since the states much below E_F in the energy scale of k_BT are full and the electric field is unable to change their occupation. The Einstein relation [40]

$$\sigma_o = e^2\rho(E_F)D(E_F) \tag{4.3}$$

relates the transport coefficient σ_o with the density of states and the diffusion constant D at the Fermi energy.

In the relaxation time approximation it is assumed that collisions completely destroy velocity correlations. The problem of electric conduction is then analogous to the problem of the diffusion of a Brownian particle in a random walk. The diffusion constant [41], $D = \int_0^\infty dt\langle v_x(t)v_x(0)\rangle$, can be readily calculated to give

$$D = \frac{1}{2}v_F^2\tau \tag{4.4}$$

This formalism will be used in Chapter 5 to calculate the effect of the periodic potential on the resistivity of the devices.

In a perpendicular magnetic field the electron trajectories are curved by the Lorentz force $-e\mathbf{v} \times \mathbf{B}/c$ and between collisions the electrons follow circular

orbits with angular velocity

$$w_c = \frac{eB}{mc} \tag{4.5}$$

The current $\mathbf{j} = ne\mathbf{v}$ is no longer parallel to the electric field

$$\mathbf{j} = \sigma_o \mathbf{E} - \frac{\sigma_o}{nec}\mathbf{j} \times \mathbf{B} \tag{4.6}$$

From equation 4.6 we immediately obtain the classical resistivity tensor

$$\rho = \begin{pmatrix} \rho_o & \frac{B}{nec} \\ -\frac{B}{nec} & \rho_o \end{pmatrix} \tag{4.7}$$

The semi-classical model predicts a zero longitudinal magnetoresistance. The experimental magnetoresistance traces of Figure 4.1 show quite a different behaviour. A small local maximum of the resistance is observed at $B \approx 0.012\,\mathrm{T}$ that is not temperature dependent. Its origin can be explained in classical terms as discussed in the next subsection. A strong negative magnetoresistance is also observed which is more pronounced at the lowest temperatures. Its possible origin due to quantum interference is discussed in section 4.3.

4.2.1 Effect of wall collisions

When the electron mean free path is longer than the channel width the electrons may interact with the walls before undergoing internal collisions with the ionized impurities. In general, for predominantly specular boundary scattering, wall collisions do not contribute significantly to the resistance.

At very low magnetic fields the curvature of the electron trajectories is not enough to force the collision with the walls and the resistivity is dominated by

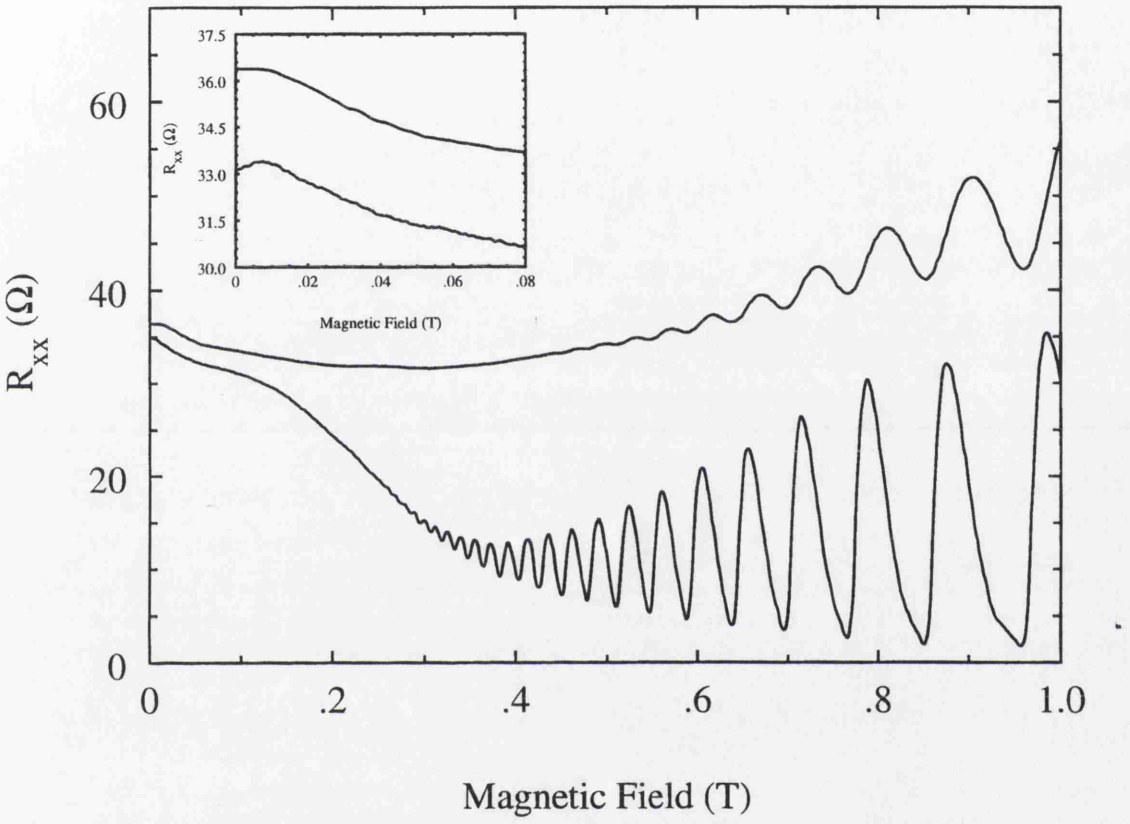

Figure 4.1: Longitudinal magnetoresistance measured at $T = 4.2\,\mathrm{K}$ and at $T = 70\,\mathrm{mK}$ in A648 samples showing the deviations from the semi-classical model. Inset: low B-field sweep that clearly shows a local maximum in the resistance associated with the presence of diffuse boundary scattering in wall collisions

the internal elastic collisions. At higher magnetic fields, when the cyclotron orbit diameter is smaller than the width of the channel and *skipping orbit* formation occurs, backscattering is only possible through internal collisions that connect the trajectories which travel independently in opposite directions along the channel edges. Therefore, in this situation the resistance is dominated once again by impurity scattering.

Only in a precise magnetic field range between the two limiting regimes discussed above is the contribution of wall collisions to the resistance significant. In this range an important number of trajectories interact with the walls before undergoing an internal collision. As illustrated in Figure 4.2 (a), a certain degree of diffuse reflection at the walls increases the channel resistance and originates a local resistance maximum.

Thornton et al. [42] have studied experimentally the maximum of $\rho_{xx}(B)$ in 2DEG narrow channels defined by low-energy ion exposure in which a higher degree of diffuse boundary scattering is present. The widths of the channels studied by Thornton et al. were between $0.2\,\mu$m and $0.6\,\mu$m so that electrons were able to interact several times with the walls before colliding with an internal impurity. They found their data to be in agreement with the theoretical result [43, 44] that for an arbitrary small amount of diffuse scattering the resistance reaches a maximum at

$$B_{max} = 0.55\frac{c\hbar k_F}{eW} \tag{4.8}$$

corresponding to a cyclotron radius roughly twice the width of the channel.

The position of the maximum of $R_{xx}(B)$ measured in the ungated device A648 (Figure 4.3) does not agree with expression 4.8. We find $B_{max} \approx 7 \times 10^{-3}\,$T, which corresponds to a cyclotron radius of $14\,\mu$m . The resistance

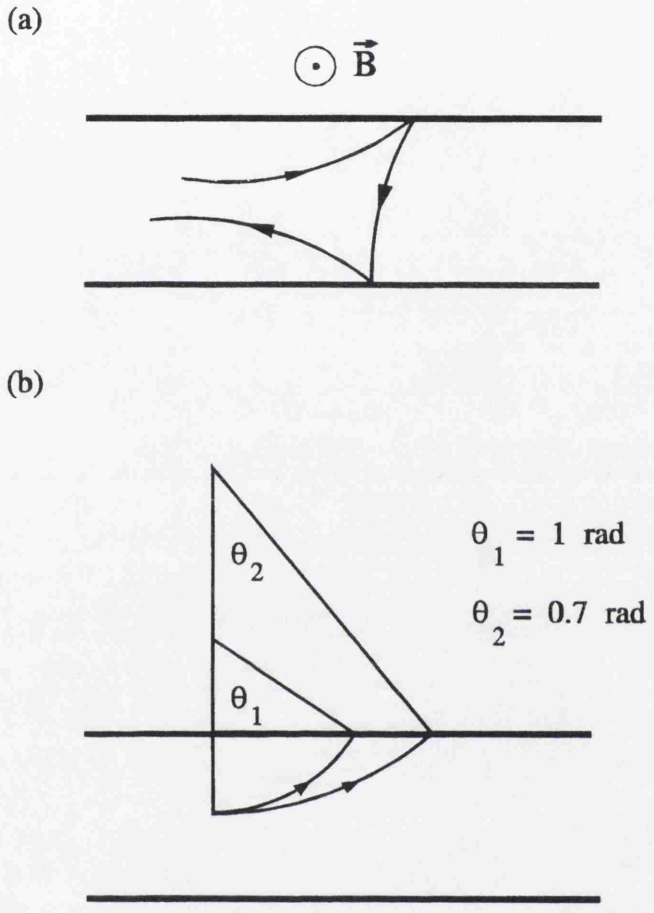

Figure 4.2: (a) Illustration of the increase of the backscattering probability due to non-specular reflections at the channel walls. (b) Curvature of the trajectories of an electron with $R_c = W$ and with $R_c = 2W$. The trajectory with $R_c = 2W$ will undergo a collision with an ionized impurity before reaching the channel wall

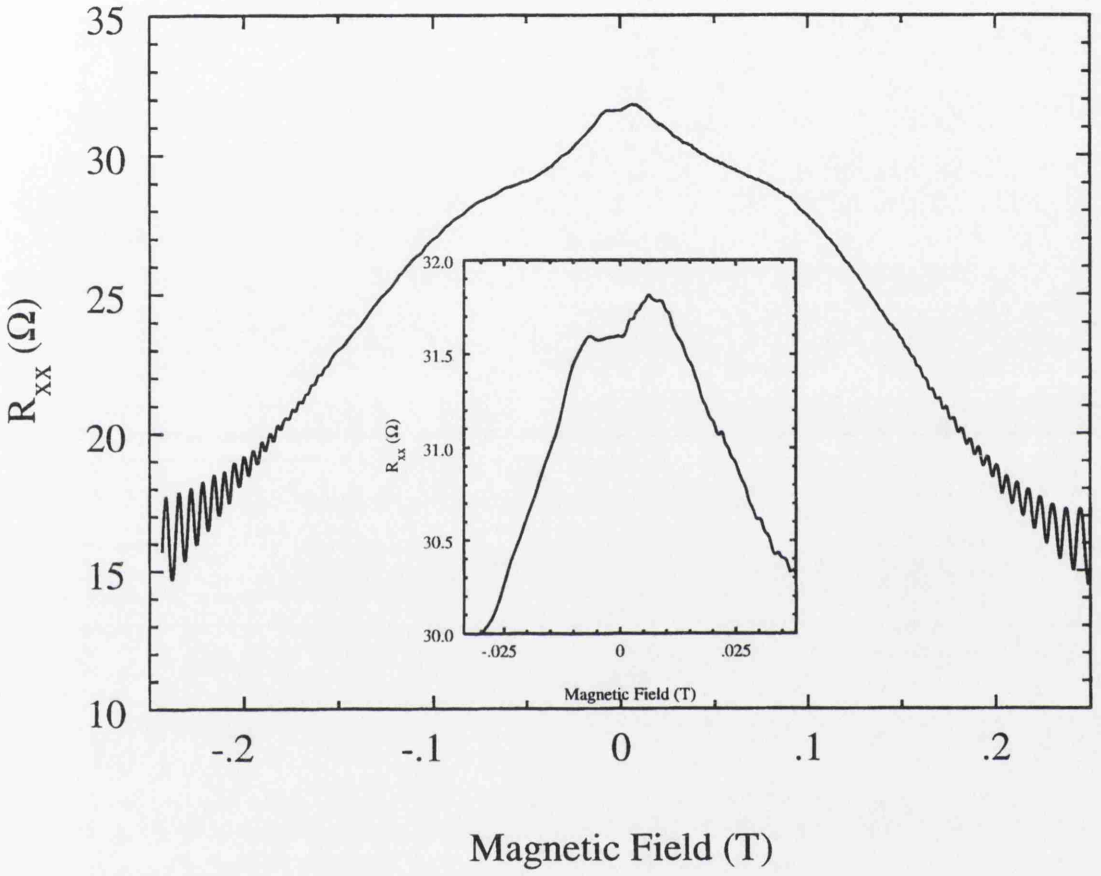

Figure 4.3: Magnetoresistance of a 14μm $\times$ 30μm Hall bar fabricated on standard HEMT A648. The local resistance maxima at $|B| \approx 7 \times 10^{-3}$ T are caused by diffuse boundary scattering

maximum appears in A648 at $R_c \approx W$ instead of at $R_c \approx 2W$ as predicted by equation 4.8.

The reason of this discrepancy is that the analysis presented in references [42, 43, 44] cannot be applied to the device A648 because the mean free path is just of the order of the width of the channel. As can be seen from Figure 4.2 when $R_c = W$ the trajectory of an electron travelling along the center of the channel can be curved until it collides with the channel wall. However, when $R_c = 2W$ the same electron follows a trajectory whose length becomes larger than the electron mean free path before reaching the channel wall and the probability of direct interaction with the channel walls decays exponentially. For magnetic fields above $B_{max} = 7 \times 10^{-3}\,\mathrm{T}$ ($\Leftrightarrow R_c = W$) the effect of boundary scattering on the conductivity starts to saturate and for $B > 1.4 \times 10^{-2}\,\mathrm{T}(\Leftrightarrow 2R_c = W)$ the conductivity is fundamentally limited by internal elastic collisions.

This low field magnetoresistance maximum is not observed in the devices made on A601 since the electron mean free path in that layer was $6\,\mu\mathrm{m}$, much shorter than the width of the channel, and thus the effect of boundary scattering is negligible.

4.3 Quantum interference corrections

Both devices, A601 and A648, exhibit a strong negative magnetoresistance at the lowest temperatures that is rapidly attenuated as the temperature is raised to 4.2 K. The sensitivity of the effect to the temperature suggests that the phenomenon has a quantum interference origin. Two different quantum interference mechanisms are known to produce negative magnetoresistance:

weak localisation and electron-electron interaction. In this section we discuss the possible sources of the negative magnetoresistance measured in our devices.

4.3.1 Weak localisation

At very low temperatures the dominant scattering mechanism is elastic impurity scattering, which is not very effective in destroying the correlation in the phase of the electron wavefunction. The electrons maintain phase coherence over distances $(D\tau_\phi)^{\frac{1}{2}}$ that can be larger than the mean free path. At $B = 0$ the interference of the electron wave functions increases the backscattering probability and therefore it causes an increase of the resistivity of the device. Time reversal invariance is the basis of the backscattering enhancement. Backscattered trajectories (which begin and end at the same point) can always be grouped in pairs of time-reversed trajectories. Since the trajectories in one pair are equivalent their probability amplitudes add coherently to the total backscattering probability.

A magnetic field destroys time-reversal symmetry and thus suppresses the effect. Magnetic field introduces a phase in the electron wavefunction that can be expressed as [45]

$$\phi = \frac{1}{\hbar}\int_{t_0}^{t_1} \mathcal{L}[\mathbf{r}(t), \dot{\mathbf{r}}(t); t]dt = \frac{1}{\hbar}\oint [\frac{1}{2}m\mathbf{v} - \frac{e}{c}\mathbf{A}]d\mathbf{l} \tag{4.9}$$

where $\mathcal{L}$ is the Lagrangian of the electron in a magnetic field and $\mathbf{A}$ is the vector potential of the magnetic field. The phase difference at the end of a closed loop traversed in opposite directions is

$$\Delta\phi = \frac{2e}{\hbar c}\oint \mathbf{A}\, d\mathbf{l} = \frac{2e}{\hbar c}\oint (\nabla \times \mathbf{A})\, dS = \frac{2eBS}{\hbar c} = \frac{2S}{l_m^2} \tag{4.10}$$

so that weak localisation effect vanishes when the area enclosed by the backscattered trajectory is of the order of the square of the magnetic length.

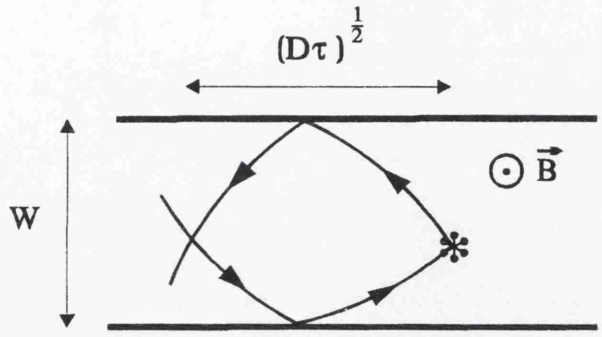

Figure 4.4: In quasi-ballistic regime the collision with a single impurity can lead to backscattered trajectories enclosing an area of the order of $(D\tau)^{\frac{1}{2}}W$. The magnetic field dephases the electron wavefunctions at the end of closed loop trajectories traversed in opposite directions so that coherent backscattering is lost when the magnetic field is turned on.

In high mobility channels in the quasi-ballistic regime, as it is the case for the devices studied here, the collision with a single impurity can lead to backscattered trajectories that enclose an area sufficient to dephase the wavefunction even in negligibly small magnetic fields (Figure 4.4). In the devices studied we find

$$\frac{W(D\tau)^{\frac{1}{2}}}{l_m^2} \approx 2 \times 10^5 \mathrm{T}^{-1} B \tag{4.11}$$

and we conclude that weak localisation does not contribute to the negative magnetoresistance observed at $0\,\mathrm{T} < B < 0.3\,\mathrm{T}$ (Figure 4.3).

4.3.2 e-e Interaction

The conductivity corrections arising from the Coulomb interaction between electrons have been studied theoretically for some time [34, 35, 36]. The e-e

correction can be visualized as the diffraction of the electron wavefunction by the electrostatic potential created by all the other electrons [32]. The fundamental length in the interaction mechanism is the thermal diffusion length, $l_T = (D\hbar/k_BT)^{\frac{1}{2}}$. At distances larger than l_T the uncertainty in the energy of the electrons is larger than the thermal energy k_BT and the coherent interference is lost. Thus, it is the width of the channel compared to l_T that determines the dimensionality of the e-e interaction [37].

The conductivity correction due to e-e interaction is independent of the magnetic field and affects only the diagonal components of the conductivity tensor [46]: $\delta\sigma_{xy} = \delta\sigma_{xy} = 0$, $\delta\sigma_{xx} = \delta\sigma_{yy} \equiv \delta\sigma_{ee}$. The inversion of the conductivity tensor yields, at first order in $\delta\sigma_{ee}$,

$$\rho_{xx} = \rho_0 \left(1 - [1 - (\omega_c\tau)^2]\frac{\delta\sigma_{ee}}{\sigma}\right) \tag{4.12}$$

and therefore a parabolic negative magnetoresistance

$$\Delta\rho(B) \approx \left(\frac{e\tau}{mc\sigma_0}\right)^2 B^2\delta\sigma_{ee} \tag{4.13}$$

The values of the correction δ_{ee} depend strongly on the dimensionality of the interaction. The theoretical predictions are, for 1D- and 2D- interaction, respectively [35, 36]

$$\delta\sigma_{1D} = -\frac{4.91e^2 l_T}{\sqrt{2}\pi^2\hbar W}\left[1 - 12\frac{1 + F/4 - (1 + F/2)^{\frac{1}{2}}}{F}\right] \tag{4.14}$$

$$\delta\sigma_{2D} = -\left(4 - 3\frac{2+F}{F}\ln\left[1 + \frac{F}{2}\right]\right)\left(\frac{e^2}{2\pi^2\hbar}\right)\left[\psi\left(\frac{1}{2} + \frac{\hbar}{k_BT\tau}\right) - \psi\left(\frac{1}{2}\right)\right] \tag{4.15}$$

where $\psi(z)$ is the digamma function [17] and

$$F = \int \frac{d\theta}{2\pi}\left[1 + \frac{2k_F}{\kappa}\sin\left[\frac{\theta}{2}\right]\right]^{-1} \tag{4.16}$$

where $\kappa = 2me^2/\epsilon\hbar^2$ is the inverse screening length in two dimensions [47].

Figure 4.5 shows a plot of the resistance of A648 Hall bar measured at $T = 70\,\mathrm{mK}$ and at $T = 4.2\,\mathrm{K}$ as a function of the square of the magnetic field. We can identify two magnetic field regions

- $0 < B^2 < 0.008\,\mathrm{T}^2$, where a strong, temperature-independent negative magnetoresistance can be seen
- $0.008\,\mathrm{T}^2 < B^2 < 0.03\,\mathrm{T}^2$, where the negative magnetoresistance is linear in B^2 and much more pronounced at $T = 70\,\mathrm{mK}$

The magnetoresistance in the first region has a semiclassical origin. In high mobility systems the regime $\omega_c\tau \equiv \mu B/c > 1$ is achieved at very low magnetic fields. In particular, for A648, with $\mu = 1.3 \times 10^6\,\mathrm{cm}^2/\mathrm{Vs}$, a magnetic field $B = 8 \times 10^{-3}\,\mathrm{T}$ is sufficient to make $\omega_c\tau = 1$. In this regime electron transport can occur only through scattering mechanisms that change the center of the cyclotron orbit, which otherwise would be constrained to move in a fixed orbit. The reflection of the cyclotron orbits at the channel walls favours the displacement of the orbit centers giving rise to the formation of skipping orbits and an enhanced diffusivity along the channel. A reduction of the device resistance occurs in the transition from a transport regime with wide cyclotron orbits, where the dominant scattering mechanism is the internal impurity scattering in the channel, to a regime with smaller cyclotron orbits that can be reflected several times by the walls of the channel before colliding with an impurity. The effect saturates very rapidly because the displacement of the orbit center is not determined by the cyclotron radius but by the electron mean free path.

In the second region we observe a negative magnetoresistance linear in B^2. For the device A648 the effective thermal length [37] $L_T \equiv \pi(\hbar D/k_B T)^{\frac{1}{2}}$ is $L_T = 43\,\mu\mathrm{m}$ at $T = 70\,\mathrm{mK}$, larger than the width of the channel, and

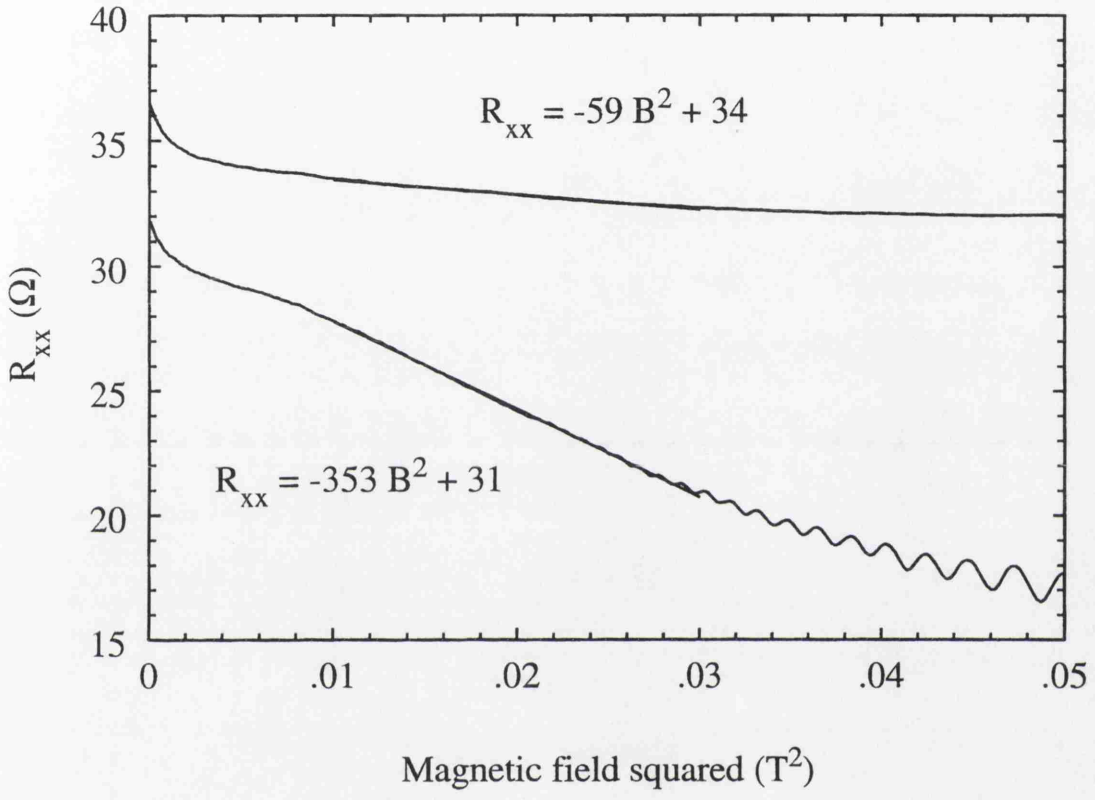

Figure 4.5: Longitudinal resistance of A648 Hall bar as a function of the square of magnetic field measured at $T = 4.2\,\mathrm{K}$ (upper trace) and at $T = 70\,\mathrm{mK}$ (lower trace). The parabolic negative magnetoresistance, much more pronounced at the lowest temperature, is attributed to electron-electron interaction. The temperature-independent magnetoresistance seen for magnetic fields close to zero is due to semi-classical size and boundary effects.

therefore the e-e interaction is one-dimensional. The evaluation of the integral 4.16 for this device gives $F = 0.54$, and substitution into equation 4.14 yields the e-e correction

$$\frac{\Delta\rho}{B^2}(T) = -\frac{48}{\sqrt{T}}\,\frac{\Omega \mathrm{K}^{\frac{1}{2}}}{\mathrm{T}^2} \tag{4.17}$$

Taking into account the geometrical factor of the Hall bar, $L/W = 2.3$, we obtain, for $T = 70\,\mathrm{mK}$, a resistance correction

$$\frac{\Delta R}{B^2} = -420\frac{\Omega}{\mathrm{T}^2} \tag{4.18}$$

The value of the correction measured experimentally (see Figure 4.5) in A648 is 16% lower than the the theoretical prediction. Similar results have been obtained by Choi et al. [37] who have justified the discrepancy by proposing a reduction of the relaxation time due to the collisions with the walls that reduces the effective interaction coefficient g_{1D}. Since in A648 Hall bar the channel width is approximately equal to the electron mean free path it is likely that wall collisions play a role in limiting e-e interaction.

At $T = 4.2\,\mathrm{K}$ the effective thermal length is $L_T = 5.5\,\mu\mathrm{m} < W$ and a two-dimensional e-e interaction correction ($\delta\sigma_{2D} \ll \delta\sigma_{1D}$) is expected. Unfortunately the experimental results cannot be compared with the theoretical predictions because the theory was derived in the approximation $k_B T\tau/\hbar < 1$ and this condition breaks down at $T \approx 170\,\mathrm{mK}$. In any case Figure 4.5 illustrates the strong reduction of the negative magnetoresistance when the temperature is raised a few degrees.

The same analysis has been repeated for the device A601, in which the channel width is more than twice the electron mean free path. For that device the theoretical e-e correction is

$$\frac{\Delta R}{B^2} = -338\,\frac{\Omega}{\mathrm{T}^2} \tag{4.19}$$

a value much closer to the measured magnetoresistance (see Figure 4.6) The reduced importance of boundary scattering due to the lower 2DEG mobility in A601 is also reflected in the absence of the semiclassical magnetoresistance region near $B^2 = 0$ in Figure 4.6.

4.4 Conductivity at quantizing magnetic fields

A strong magnetic field produces the quantization of the electronic levels and the semiclassical model is no longer valid. A quantum mechanical description is necessary. The Hamiltonian of an electron in a magnetic field is

$$\mathcal{H} = \frac{\mathbf{P^2}}{2m} \tag{4.20}$$

where

$$\mathbf{P} = -i\hbar\nabla + \frac{e}{c}\mathbf{A} \tag{4.21}$$

and $\mathbf{A}$ is the vector potential associated with the magnetic field ($\nabla \times \mathbf{A} = \mathbf{B}$). The components of the canonical momentum 4.21 verify the commutation relation

$$[P_x, P_y] = -\frac{i\hbar^2}{l_m^2} \tag{4.22}$$

Using 4.22 it is easy to show that the canonical transformation

$$a^\dagger = \frac{l}{2\sqrt{2}\hbar}(P_x + iP_y) \tag{4.23}$$

reduces the Hamiltonian 4.20 to the Hamiltonian of a harmonic oscillator

$$\mathcal{H} = \hbar\omega_c \left(a^\dagger a + \frac{1}{2}\right) \tag{4.24}$$

In the Landau gauge, $\mathbf{A} = (-yB, 0)$, the Schrodinger equation is separable and an analytical form for the electron wavefunction can be found

$$\psi(x,y) = e^{ikx} H_n(\frac{y}{l} - lk) \exp\left[-\frac{(y - l^2k)^2}{2l^2}\right] \tag{4.25}$$

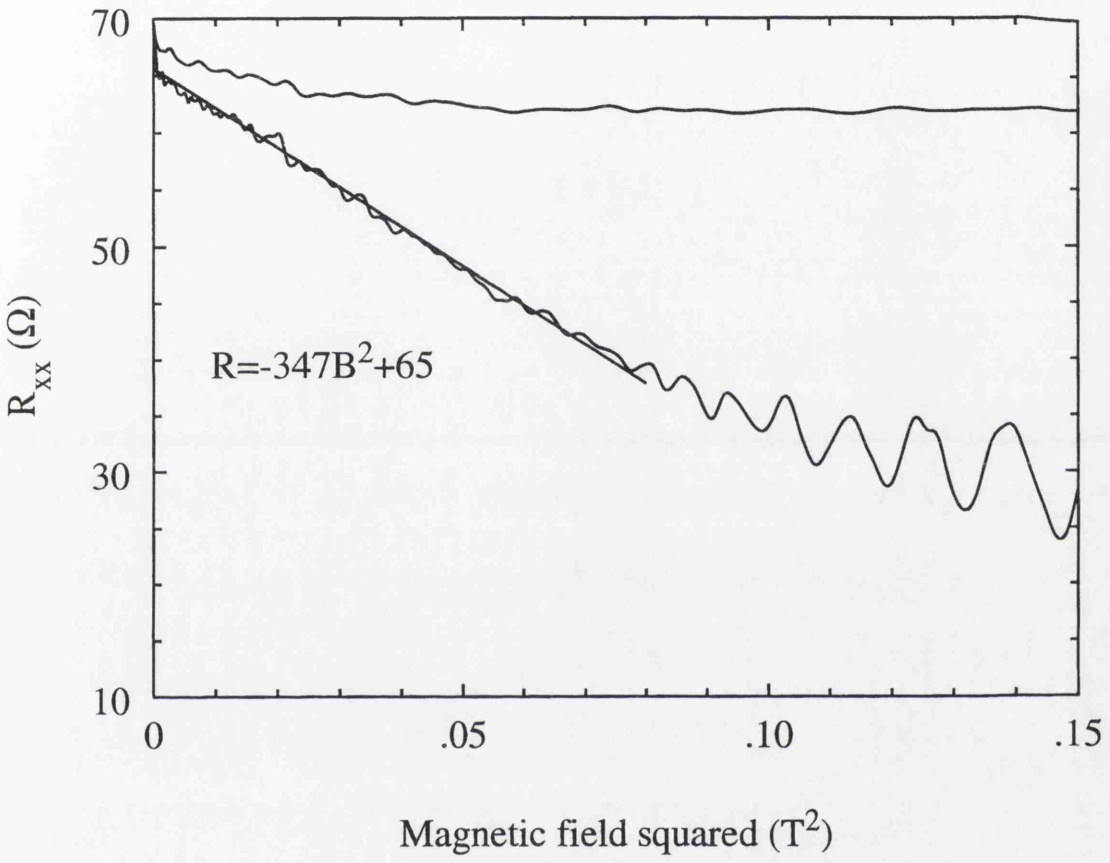

Figure 4.6: Resistance of a A601 Hall bar as a function of the square of magnetic field measured at $T = 4.2\,\mathrm{K}$ (upper trace) and at $T = 70\,\mathrm{mK}$ (lower trace).

where H_n is the Hermite polynomial of degree n. Equation 4.25 is the eigenfunction of a harmonic oscillator centered at $y = l^2k$. The states 4.25 are extended in the x direction but confined in the y direction. However, due to the Landau level degeneracy, it is possible to construct linear combinations of states that are localized in both directions. An impurity potential may lift Landau level degeneracy and limit the choice of wavefunctions to localized states.

The eigenvalues of operator 4.24 define Landau levels. Including the spin contribution Landau level energies are given by

$$E_n = \left(n + \frac{1}{2}\right)\hbar\omega_c \pm \frac{g}{2}\mu_B B \tag{4.26}$$

where g is the electron Landé factor and $\mu_B = e\hbar/2mc$ the Bohr magneton. g factor is 2 for free electrons but in a semiconductor it depends on the band-structure and on the spin-orbit coupling. For electrons in GaAs $g \approx 0.32$ [48]. In general the spin contribution is much smaller than the orbital contribution and Landau splitting is observed only at very low temperatures and high magnetic fields.

Landau level energy does not depend on k and therefore there is a high degree of degeneracy. The number of states in each Landau Level is equal to one state per magnetic quantum flux hc/e through the sample. The number of states per unit area (for each spin) is given by

$$n_B = \frac{1}{2\pi l_m^2} \tag{4.27}$$

The separation between Landau levels, $\hbar\omega_c$, and the level degeneracy, $1/2\pi l_m^2$, are proportional, so that the Landau level E_n contains the same number of states as the energy range $(E_n - \frac{1}{2}\hbar\omega_c, E_n + \frac{1}{2}\hbar\omega_c)$ of the 2DEG in absence of magnetic field.

By the effect of the impurity potentials the Landau levels broaden. Close to the original Landau level there is a core of extended states capable of carrying current. Between Landau levels there is an energy gap filled by localized states which act as electron reservoirs but cannot contribute to the current. When the Fermi level lies in the energy gap an increase of magnetic field causes the depopulation of localized states without altering the extended state occupation. In this situation the Hall resistance maintains a constant value

$$R_H = \frac{1}{N}\frac{h}{e^2} \qquad (N \text{ integer}) \tag{4.28}$$

When a Landau level is full the Fermi Level is in the middle of the energy gap, where the density of states $\rho(E_F)$ is minimum. The scattering rate, which in the Born approximation is proportional to $\rho(E_F)$, is negligible and the system becomes non-dissipative. The longitudinal resistivity of the 2DEG vanishes for integer values of the occupation factor $\nu = n_{2D}/n_B$.

The Landau level separation increases linearly with magnetic field and the states that traverse the Fermi energy are redistributed among the Landau levels below E_F. The crossing of successive Landau levels through the Fermi level gives rise to an oscillatory longitudinal magnetoresistance, the well known Shubnikov-deHaas effect, with zeros at $\nu = 1, 2, \ldots$ and $1/B$ periodicity determined by the electron density

$$\Delta\left(\frac{1}{B}\right) = \frac{e}{chn_{2D}} \tag{4.29}$$

The width of the zeros of ρ_{xx} depends on the temperature and on the spectrum of localized states. The effect of temperature is clearly seen in the measurements displayed in Figure 4.7, where much wider Hall plateaux, as well as spin-split plateaux, are revealed at the lowest temperature. Also, much sharper, spin-split magnetoresistance maxima are observed at the lowest temperature, for magnetic fields at which the transition from a spin-split Hall

plateau to the next takes place.

The maxima of longitudinal resistivity occur when the Fermi level is at the center of a spin-split Landau level, where the density of states is maximum. According to 4.26 the position of the maxima of ρ_{xx} are given by

$$B_{\pm} = \frac{E_F}{[(2n+1) \pm \frac{g}{2}]\mu_B} \tag{4.30}$$

In table 4.1 the measured B field position of the maxima (Figure 4.7) are compared with the predictions of equation 4.30. A good agreement is observed at low fields. However at high fields the ρ_{xx} maxima associated with the high energy spin-split Landau levels occur at lower magnetic fields than those predicted by 4.30 whereas the maxima assiciated with the low energy spin-split Landau levels are observed at higher magnetic fields. The reason of these discrepancies lies in the oscillations of the Fermi level due to the continuous rearrangement of electronic states in Landau levels as the magnetic field is increased. Figure 4.8 illustrates the effect. In the maximum of ρ_{xx} associated with $N\uparrow$ the electrons fill three quarters of the Landau level. As a result of the collapse of electronic states into Landau levels the Fermi level of the electrons in magnetic field lies below the Fermi level of the free 2DEG. Therefore the level $N\uparrow$ traverses E_F at a magnetic field higher than the one given by 4.30. Similarly, in the maximum associated with the low energy level, $N\downarrow$, E_F lies above the Fermi level of the 2DEG and the maximum occurs at a higher magnetic field. The correction in the position of E_F is given, assuming a perfectly symmetric density of states, by

$$\delta E_F = \frac{1}{4}\hbar\omega_c - \frac{1}{2}\mu_B g B \tag{4.31}$$

and is more significant at high magnetic fields. The precise value of the correction depends on the particular shape of the density of states. The fact that the correction is more important for the maxima associated with the levels $N\uparrow$ (see Table 4.1) suggests an asymmetric density of states with tails

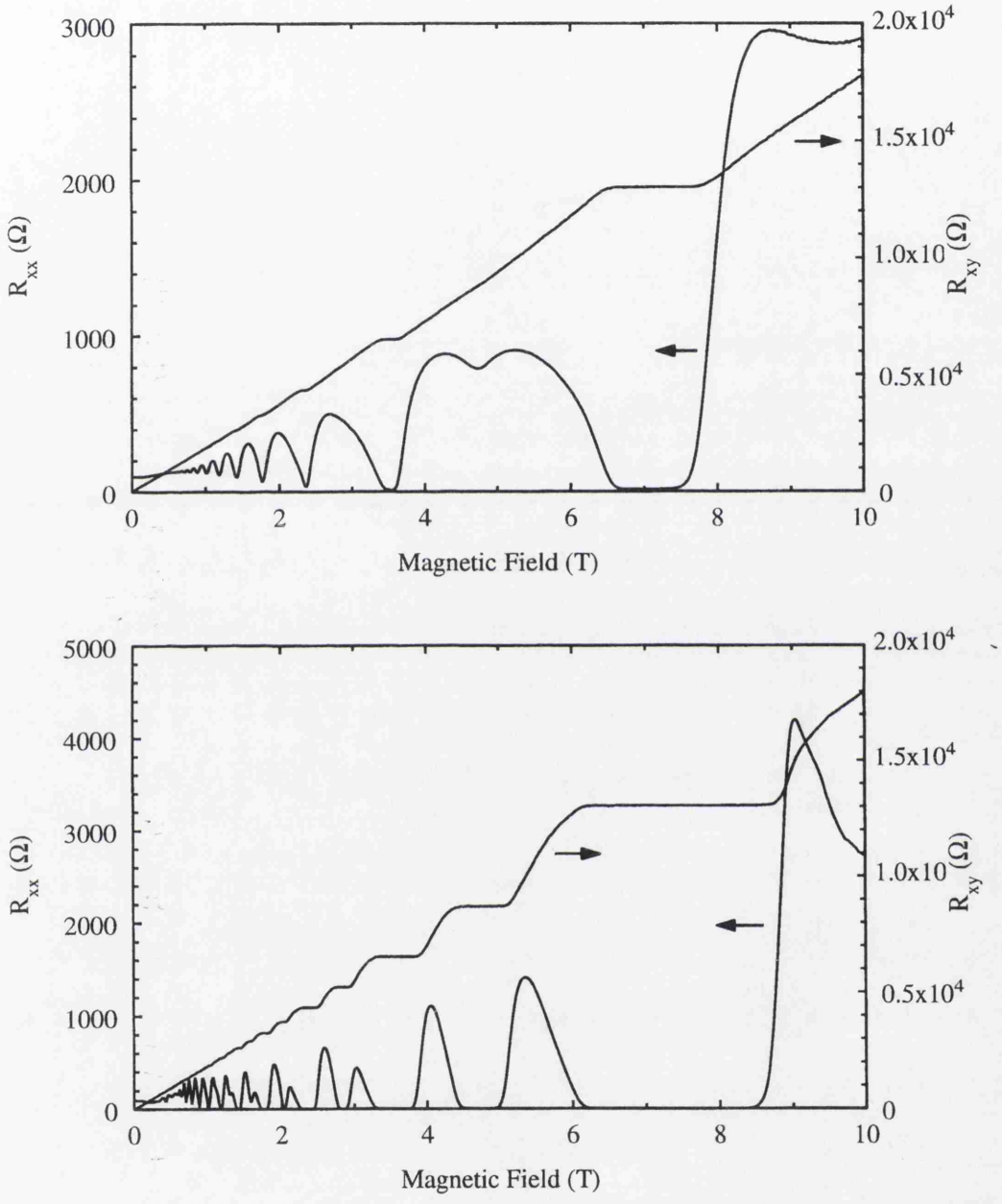

Figure 4.7: Shubnikov-deHaas oscillations and Hall resistance measured in the device A601 at $T = 4.2\,\mathrm{K}$ (a) and $T = 70\,\mathrm{mK}$ (b). The observation of flat, well-defined Hall plateaux and the corresponding zeroes of the longitudinal resistivity show that the good quality 2DEG present in this layer is preserved after processing the devices. Spin-split levels are clearly resolved at the lowest temperature even for moderate fields.

Table 4.1: Position of the ρ_{xx} maxima. The experimental values were measured in a A601 Hall bar (see Figure 4.7), and the theoretical predictions were calculated using 4.30 with $E_F = 13.0\,\text{meV}$ and $g = 0.32$

N	B_{max}(T) (theory)	B_{max}(T) (experimental)
$1\downarrow$	5.34	5.59
$1\uparrow$	4.80	4.26
$2\downarrow$	3.13	3.17
$2\uparrow$	2.94	2.71
$3\downarrow$	2.22	2.23
$3\uparrow$	2.12	2.00
$4\downarrow$	1.71	1.72
$4\uparrow$	1.65	1.59
$5\downarrow$	1.40	1.40
$5\uparrow$	1.36	1.31
$6\downarrow$	1.18	1.18
$6\uparrow$	1.15	1.12

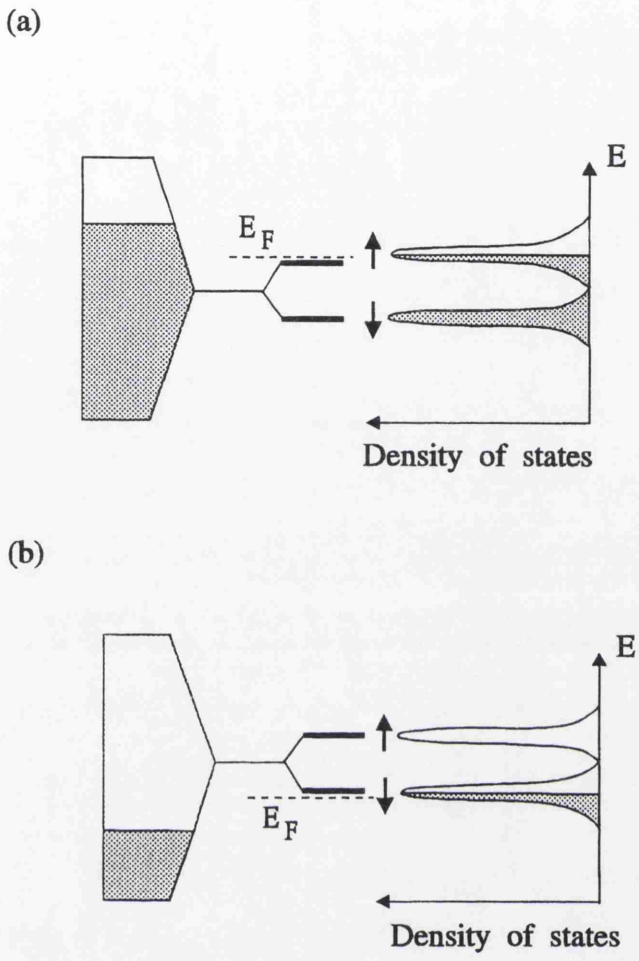

Figure 4.8: Fermi energy correction due to the rearrangement of electronic states in Landau levels. (a) Situation corresponding to the low-field spin-split maxima of ρ_{xx} $(N \uparrow)$. (b) Situation corresponding to the high-field spin-split maxima of ρ_{xx} $(N \downarrow)$. The oscillation of the Fermi Energy due to the rearrangement of electronic levels results in a shift towards lower magnetic fields of the ρ_{xx} maxima associated with the high-energy spin-split Landau Levels and a shift towards higher magnetic fields of the maxima associated with the low-energy spin-split Landau Levels.

towards the low-energy edge.

The effect of scattering centers on the shape of the density of states distribution has been investigated theoretically by T. Ando [49, 50]. The calculations show that the density of states has a low-energy tail in presence of a low concentration of attractive scattering centers whereas a small concentration of repulsive centers produces a high-energy tail. In AlGaAs/GaAs both kinds of scattering center are present: ionized Si donors in the doped layer act as attractive centers while the small concentration of residual acceptors in the GaAs supply the repulsive centers. In low enough concentrations (high mobility samples) the impurity distribution is responsible for the asymmetries in the Shubnikov-de Haas oscillations [51]. The results obtained in the material A601 suggest a dominance of collisions with positive scattering centers.

4.5 2DEG characterization

The study of the magnetoresistance at moderate fields, where the Hall plateaux are not yet fully developed, yields useful information about the 2DEG electric characteristics. The 2DEG carrier density can be obtained from the periodicity of the oscillations of ρ_{xx} while an amplitude analysis of those oscillations gives an estimation of the scattering rate.

Isihara and Smrčcka [52] have developed a magnetoconductivity model based on the coherent potential approximation. In this model, many Landau levels and multiple collisions are incorporated in the impurity configuration averages so that it is especially suited to describe low magnetic fields. The

resulting density of states acquire an oscillatory component

$$\frac{\Delta\rho(E)}{\rho_0} = 2\sum_{n=1}^{\infty}\exp(-\pi n/\omega_c\tau_q)cos\left[\frac{2\pi nE}{\hbar\omega_c} - n\pi\right] \tag{4.32}$$

where $\tau_q = \hbar/2\Gamma$ is the lifetime of an electron in a Landau level represented by a Lorentzian of width Γ. As a result, both the number of electrons participating in transport and the scattering rate acquire an oscillatory component. At first order in $\delta\rho(E)/\rho_0$ it is found, at $T = 0\,\mathrm{K}$,

$$\rho_{xx} = \rho_{xx}^{(0)}\left[1 + 2\frac{\Delta\rho(E_F)}{\rho_0}\right] \tag{4.33}$$

At finite temperatures the thermal average of the oscillatory component introduces a damping factor $D(X) = X/\sinh(X)$, where $X \equiv 2\pi^2 k_B T/\hbar\omega_c$ [48]. Thus, the oscillatory component of the magnetoresistance can be written

$$\frac{\Delta\rho_{xx}}{\rho_{xx}^{(0)}} = D(X)\frac{\Delta\rho(E_F)}{\rho_0} \tag{4.34}$$

The 2DEG carrier concentration is obtained from the periodicity in B^{-1} of the oscillations (equation 4.32). The magnetic frequency of $\rho_{xx}(B^{-1})$ can be determined with precision using a Fast Fourier Transform (FFT) [63] of the experimental magnetoresistance data (see *Appendix* for details). According to equations 4.32 and 4.33 the 2DEG density is given by

$$N_{2D} = \frac{2e\nu}{hc} \tag{4.35}$$

where ν is the peak position in the Power Spectral Density (PSD) of $R_{xx}(B^{-1})$. The electron mobility is calculated from the zero-field resistance R_0 as

$$\mu = \frac{1}{N_{2D}eR_0}\frac{L}{W} \equiv \frac{e\tau}{m} \tag{4.36}$$

Figure 4.9 shows the spectral analysis of SdH oscillations measured in A601 at

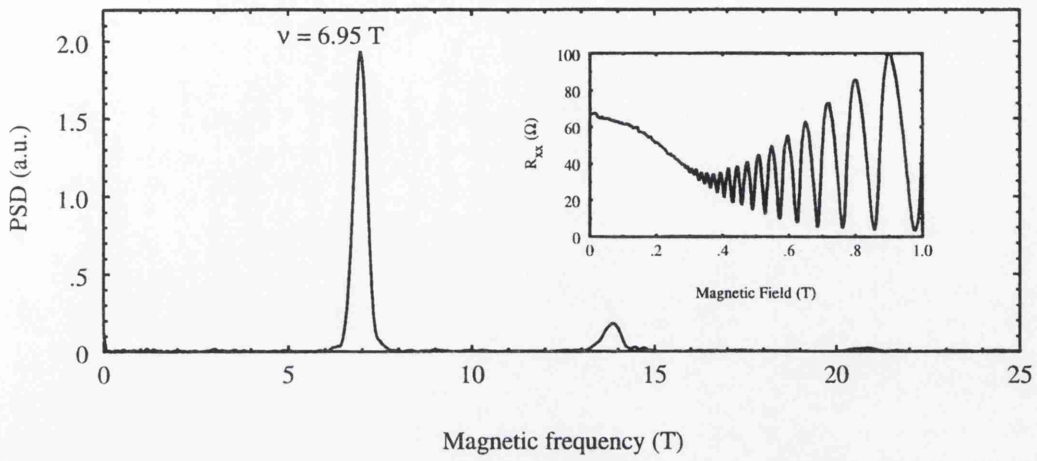

Figure 4.9: Power Spectral Density of the SdH oscillations (inset) measured in A601 at 70 mK

$T = 70\,\mathrm{mK}$. Equation 4.35 gives $N_{2D} = 3.37 \times 10^{11}\,\mathrm{cm}^{-2}$ and with $R_0 = 67\,\Omega$ equation 4.36 gives $\mu = 6.52 \times 10^5\,\mathrm{cm}^2/\mathrm{Vs}$ and a corresponding relaxation time of $\tau = 25\,\mathrm{ps}$.

The value of τ deduced from equation 4.36 is the transport relaxation time

$$\tau^{-1} \propto \int_{-\pi}^{\pi} \sigma(\theta)(1 - \cos\theta)d\theta \tag{4.37}$$

where the factor $(1-\cos\theta)$ reflects the fact that the small-angle collisions have a reduced effect on the electric current [53]. The high mobility in AlGaAs/GaAs heterostructures is achieved precisely by separating the ionized donors from the 2DEG with an undoped spacer layer. However, all collisions contribute to the Landau level broadening [52] and therefore the relaxation time appearing in equation 4.32 is not the transport relaxation time 4.37 but the electron lifetime in a Landau level, which is given by an expression analogous to 4.37 without the factor $(1 - \cos\theta)$. This lifetime can be determined using Dingle plots [54]. According to equations 4.32 and 4.34 a plot of $\ln(\Delta R_{xx}/D(T))$ as

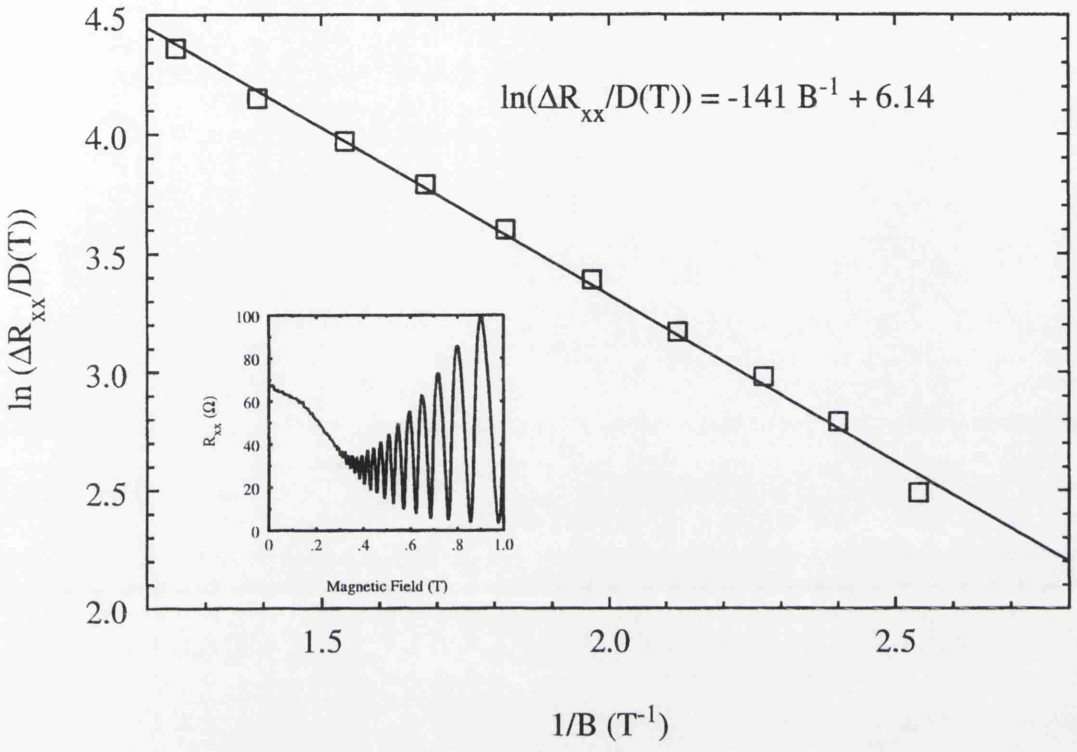

Figure 4.10: Dingle plot constructed from the SdH oscillations measured in A601 at $T = 70\,\mathrm{mK}$ (inset). The slope of the plot gives a determination of the quantum relaxation time of an electron in a Landau Level.

a function of $1/B$ gives a straight line of slope

$$-\frac{\pi mc}{e\tau_q} \tag{4.38}$$

which allows the determination of the quantum relaxation time τ_q. Figure 4.10 shows a Dingle plot for the SdH oscillations measured in A601 at $T = 70\,\mathrm{mK}$. The value of the relaxation time deduced from the slope is $\tau_q = 8.5 \times 10^{-13}\,\mathrm{s}$, much smaller than the transport relaxation time estimated from the mobility. The ratio $\tau/\tau_q \approx 29$ is consistent with theoretical calculations by Das Sarma and Stern [53]. However, there is experimental evidence that in high purity samples ratios of $\tau/\tau_q \approx 10$ or less can be achieved. The relatively high value of τ/τ_q measured in A601 may be indicative of the presence of impurities in

the spacer layer which are likely to have diffused from the δ-doped layer during the growth of the sample.

Chapter 5

Magnetotransport in LSSL devices

In this chapter we study the effect of a weak periodic modulation in the x-direction on the electronic transport in the 2DEG. As described in Chapter 2 the modulation is achieved by means of a periodic array of metal gates deposited on the semiconductor surface. The gates can be kept at the same potential as the 2DEG by interconnecting the gate and source contacts. Even in that configuration a relatively strong modulation can be observed in the 2DEG. Alternatively, the gate potential can be fixed relative to the 2DEG using a universal voltage source so that the effect of the electrostatic field on the 2DEG modulation can be studied.

The weak periodic modulation is reflected in the longitudinal magnetoresistance of the LSSL devices as a series of novel oscillations periodic in $1/B$ [10, 11, 14, 29]. The origin of these oscillations is now well understood, either from a semiclassical description [12] or from a quantum-mechanical treatment [13]. In the next section we give an overview of the semiclassical theory since it yields analytical expressions for the magnetoresistivity that will be used to

relate the magnetoresistance oscillations to the characteristics of the periodic modulation. In the rest of the chapter we present the experimental magnetoresistance traces measured in our LSSL devices and discuss the sources of modulation that give rise to the periodic potential at the 2DEG. The temperature dependence of these oscillations is also studied.

5.1 Theory of electronic transport in a weak periodic modulation

The ultimate objective of superlattice devices is to exploit artificially induced bandstructure effects. However, because of the relatively high position of the Fermi energy E_F relative to the energy $E_B = (\hbar\pi/a)^2/(2m)$ at which the fundamental band gap occurs, artificial bandstructure effects are not seen in devices fabricated using existing nanostructure technology.

The Schrödinger equation for an electron in a 1D periodic potential $V(x) = V_0 \cos(k_B x)$ is

$$\left(-\frac{\hbar^2}{2m}\frac{d^2}{dx^2} + V(x) - E\right)\psi(x) = 0 \tag{5.1}$$

Introducing

$$2z = k_B x$$

$$\alpha = \frac{E}{E_B}$$

$$2q = \frac{V_0}{E_B}$$

equation 5.1 can be written as

$$\frac{d^2\psi}{dz^2} + (\alpha - 2q\cos 2z)\psi = 0 \tag{5.2}$$

Table 5.1: Characteristic values of Mathieu's equation for a typical LSSL device: $\alpha = 9.52 \times E(\text{meV})$, $q = 2.86$. The corresponding band gap energies (in meV) are also displayed.

n	0	1	2	3	4	5	6
a_n	-2.6401	2.5216	5.9260	9.8248	16.3048	25.1726	36.1172
b_n		-2.5847	3.3408	9.2137	16.2499	25.1701	36.1171
$\Delta E_G^{(n)}$		0.536	0.271	0.064	0.006	2.7×10^{-4}	7.6×10^{-6}

which is the canonical form of Mathieu's differential equation [17]. Solutions to this equation can be found as Fourier series and exist only for certain values of $\alpha = a_0 < b_1 < a_1 < \ldots < b_r < a_r \ldots$, which can be calculated using a continued fraction expansion in terms of the quantities $V_m = (\alpha - m^2)/q$. In the region between $a_r(q)$ and $b_{r+1}(q)$ Floquet'solutions of the form $\exp(i\nu z)P(z)$ have a real exponent and are thus bounded for real z. The characteristic exponent ν is complex in the regions between b_r and a_r. For a given q the energies $a_r E_B < E < b_{r+1} E_B$ form bands of allowed states while the energies $b_r E_B < E < a_r E_B$ correspond to energy gaps. Table 5.1 shows the values of α calculated for a typical LSSL device with $N_{2D} = 3.5 \times 10^{11}\,\text{cm}^{-2}$, $a = 230\,\text{nm}$ and $V_0 = 0.6\,\text{meV}$. It is clearly seen that the band gap energies $\Delta E_G^{(n)}$ decrease very rapidly with the index of the miniband. Given that the thermal energy at $T = 70\,\text{mK}$ is $k_B T = 6\,\mu\text{eV}$ only the first three minigaps can be resolved at fridge temperatures. The Fermi energy in such a device is $E_F = 12.4\,\text{meV}$ whereas $E_B = 0.10\,\text{meV}$. This means that the Fermi level is close to the 11th miniband, where the band gaps are totally negligible and therefore no band-

Table 5.2: Characteristic values of Mathieu's equation for an ideal LSSL device: $\alpha = 0.64 \times E(\text{meV})$, $q = 0.32$, $E_F = 7.1\,\text{meV}$, $E_B = 1.55\,\text{meV}$. The corresponding band gap energies (in meV) are also displayed.

n	0	1	2	3	4
a_n	-0.0506	1.3067	4.0421	9.0069	16.0034
b_n		0.6670	3.9915	9.0059	16.0034
$\Delta E_G^{(n)}$		0.992	0.051	0.002	1.4×10^{-5}

structure effects should be expected.

True superlattice devices would require excellent high mobility material with a shallow 2DEG and low carrier concentration, and ultra-fine nanolithography. Even if making use of present state-of-the-art technology it were possible to fabricate an ideal device with, say, $N_{2D} = 2 \times 10^{11}\,\text{cm}^{-2}$, $a = 60\,\text{nm}$ and $V_0 = 1\,\text{meV}$ the observation of minigap effects would be very difficult and would require temperatures well below 10 mK. Table 5.2 shows the band gap characteristics of such a device, in which the Fermi level would lie in the fifth miniband. Apart from the enormous fabrication challenge the performance of these short-period devices is likely to be affected by irregularities of the gates, strong attenuation of the periodic potential at depths larger than the period and the effect of random impurity potential. It appears very unlikely that LSSL devices can be used in transport experiments aimed at detecting bandstructure formation.

LSSL devices have proved to be a much more fruitful system in magnetotransport experiments. The interplay of the different length scales: λ_F, R_c, a in the mesoscopic system gives rise to commensurability resonances that reflect the perturbing periodic potential [10, 11, 14, 29]. There have been recent experiments [7] that demonstrate the formation of magnetically induced bandstructure in a corrugated split-gate device in the quantum Hall effect regime.

We concentrate on the commensurability resonances that appear at low fields ($B < 1\,\mathrm{T}$). Next we give an outline of the semi-classical model due to C. W. Beenakker [12]. This model yields analytical expressions for the magnetoresistance that we shall use in the interpretation of our data.

In crossed electric and magnetic fields ($|\mathbf{E}| < |\mathbf{B}|$) the cyclotron orbit of the electron acquires a uniform drift perpendicular to $\mathbf{E}$ and $\mathbf{B}$ [57]

$$\mathbf{u} = c\frac{(\mathbf{E}\times\mathbf{B})}{B^2} \tag{5.3}$$

that corresponds to the velocity associated with the Lorentz transformation to a reference frame in which the only field acting is a static magnetic field $\mathbf{B}' = \sqrt{1-(E/B)^2}\mathbf{B}$.

In the case of a weak periodic potential $V(x) = V_0\sin(Kx)$ the electron will experience alternating $\mathbf{E}\times\mathbf{B}$ drifts (see Figure 5.1). The average of the drift velocity along a cyclotron orbit is given by

$$u(x_0) = \frac{c}{2\pi B}\int_0^{2\pi} d\phi V_0 K\cos\left(K(x_0 + R_c\cos\phi)\right) \tag{5.4}$$

The integral can be calculated analytically and it gives

$$u(x_0) = \frac{\sqrt{2}cV_0}{aB}2\pi J_0(KR_c)\sin(Kx_0) \approx \frac{2cV_0}{B\sqrt{aR_c}}\cos\left(KR_c - \frac{\pi}{4}\right)\sin(Kx_0) \tag{5.5}$$

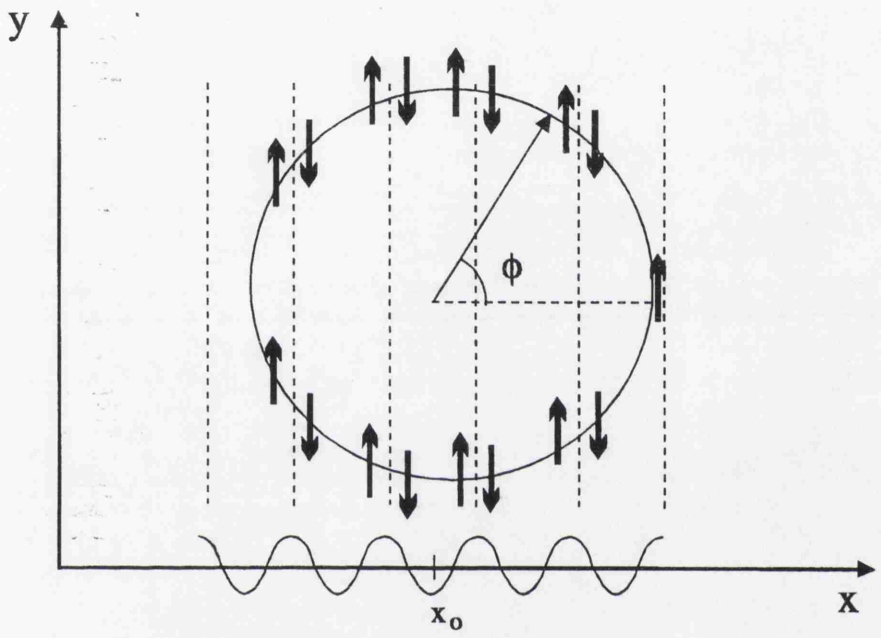

Figure 5.1: $\mathbf{E} \times \mathbf{B}$ drift of the cyclotron orbits caused by a periodic electrostatic potential. The electron experiences alternating drifts that approximately cancel out along the orbit, except those acquired at the extremal points, which, depending on the radius of the orbit and the position of its center, can lead to guiding-center-drift resonances.

where $J_0(z)$ is a Bessel function, and the approximation [17]

$$J_0(KR_c) \approx \sqrt{2/(\pi KR_c)}\cos(KR_c - \frac{1}{4}\pi)$$

has a remarkable accuracy for $R_c > a$ [1]. From equation 5.5 it is clear that the drift velocity depends both on the ratio R_c/a and on the position of the center of the orbit x_0. It is maximum for orbits of diameter $2R_c = (n + \frac{1}{4})a$ centered at $x_0 = (2j + 1)(a/4)$. In these conditions the electric field at the extrema $x_0 \pm R_c$ has the same sign and therefore the extremal points contribute to a net drift velocity. Along the rest of the orbit the electric field has alternating signs and the drift approximately cancels out.

The guiding-center drift of the cyclotron orbits contributes to increase the diffusion in the y-direction, along the equipotential lines. The enhancement of diffusion along the y-direction is incorporated into the diffusion tensor as an additional contribution to the yy element of the unperturbed diffusion tensor [2]

$$\delta D_{yy} \equiv \tau\langle u^2(x_0)\rangle = \left(v_F\frac{eV}{E_F}\right)^2 \frac{R_c}{a}\cos^2\left(KR_c - \frac{\pi}{4}\right) \tag{5.6}$$

where the angular brackets denote an average over all possible orbit centers. The resulting diffusion tensor of the modulated 2DEG is

$$\mathbf{D} = \frac{\frac{1}{2}\tau v_F^2}{1 + (\omega_c\tau)^2}\begin{pmatrix} 1 & -\omega_c\tau \\ \omega_c\tau & 1 + \dfrac{1 + (\omega_c\tau)^2}{\frac{1}{2}\tau v_F^2}\tau\langle v_d^2\rangle \end{pmatrix} \tag{5.7}$$

The correction to the longitudinal magnetoresistivity can be calculated by

[1] Better than 0.15% relative to the maximum of $J_0(z)$ at $z \approx 7.01$

[2] This assumption is supported by a rigorous solution of the Boltzmann equation given in ref. [12]

inverting 5.7 and using Einstein's relation. In the approximation $\omega_c\tau \gg 1$, $eV_0/E_F \ll 1$ one finds, to second order in eV_0/E_F,

$$\frac{\delta\rho_{xx}}{\rho_0} = 2\left(\frac{eV}{E_F}\right)^2 \frac{l^2}{aR_c}\cos^2\left(\frac{2\pi R_c}{a} - \frac{\pi}{4}\right) \tag{5.8}$$

It is important to realize that the expression 5.8 can be immediately generalized to an arbitrary periodic potential. Because of the orthogonality properties of the circular functions, each of the Fourier components of an arbitrary potential contributes independently to the magnetoresistance correction. The crossed terms that appear in the integral analogous to 5.4 are all orthogonal. Thus, the magnetoresistance correction due to an arbitrary periodic potential

$$V(x) = \sum_{n=0}^{\infty} V_n \cos\left(n\frac{2\pi}{a}x\right) \tag{5.9}$$

is given by

$$\frac{\delta\rho_{xx}}{\rho_0} = 2\sum_{n=1}^{\infty}\left(\frac{eV_n}{E_F}\right)^2 \frac{nl^2}{aR_c}\cos^2\left(\frac{2\pi nR_c}{a} - \frac{\pi}{4}\right) \tag{5.10}$$

Equation 5.10 shows that the functional form of the magnetoresistance oscillations directly reflects that of the perturbing potential. Therefore a Fourier analysis of the magnetoresistance data makes it possible to reconstruct the modulation potential at the 2DEG [3] [14] and it provides useful information to check the assumptions usually made in current models of surface-gated devices [56]

The expression 5.8 was also obtained by Winkler et al. [10] using quantum mechanics and first-order perturbation theory. In a quantum-mechanical formalism the periodic potential lifts Landau level degeneracy and induces an energy dependence in the quantum number k_y. The Landau levels become

[3] apart from the phase of the Fourier coefficients V_n

Landau energy bands $\epsilon_n(k_y)$ which have an associated group velocity

$$\langle k_y n|v_y|k_y n\rangle = \frac{1}{\hbar}\frac{d\epsilon_n}{dk_y} \tag{5.11}$$

In a semi-classical approximation, in which matrix elements are replaced by averages along cyclotron orbits, the Landau bands can be expressed as

$$\epsilon_n(k_y) = (n+\frac{1}{2})\hbar\omega_c + V\left(\frac{a}{\pi^2 R_c}\right)^{\frac{1}{2}} \cos\left(\frac{2\pi R_c}{a} - \frac{\pi}{4}\right)\cos\left(\frac{2\pi l_m^2 k_F}{a}\right) \tag{5.12}$$

The bandwidth of Landau bands is an oscillatory function of R_c/a and it vanishes for $2R_c = (m-\frac{1}{4})a$. The oscillatory band conductivity is reflected in the longitudinal resistivity since, for $\omega_c\tau \gg 1$ and in absence of Hall quantization, the longitudinal resistivity is given by

$$\rho_{xx} = \frac{\sigma_{yy}}{\sigma_{xy}^2} \tag{5.13}$$

The approaches of references [10, 12] are basically equivalent and illustrate the clasical nature of the commensurability oscillations. However the use of the semi-classical theory to describe experimental results has important limitations:

1. It is assumed that $\omega_c\tau \gg 1$. This assumption may not hold at low magnetic fields in devices with a negative gate bias.

2. The theory breaks down for $B \to 0$. This can be seen either in the initial quantum-mechanical formulation of refs. [10, 13], where the first-order perturbation theory approximation is increasingly inaccurate for $B < 0.1\,\mathrm{T}$, or in a purely classical approach, where the Lorentz force at low magnetic fields is not strong enough to overcome the periodic potential barriers and the electron trajectory is trapped between two equipotential lines forming *streaming orbits* [29].

3. As stressed by C. W. J. Beenakker [12], the mechanism leading to the oscillations follows from classical mechanics and does not require Landau band quantization. Classical theory totally ignores the discreteness of Landau levels. In high mobility devices at very low temperatures, commensurability oscillations are observed in coexistence with Shubnikov-de Haas oscillations and the interference between the two phenomena is apparent. Only a fully quantum-mechanical theory that treats both kinds of oscillations on the same footing, like the one proposed by C. Zhang and R. Gerhardts [13], can explain the experimental results.

5.2 Commensurability oscillations in a conventional HEMT

5.2.1 Experimental data

We present here magnetoresistance measurements made on a 250 nm period LSSL fabricated on the standard HEMT material A648, where the 2DEG is formed at 90 nm below the surface. All the measurements discussed in this section were performed at 70 mK with the gates connected to the source contact and after illumination of the device using an IR LED. This particular device did not show commensurability oscillations in the dark.

Figure 5.2 shows a magnetoresistance trace measured at $T = 70\,\mathrm{mK}$ after a short illumination using an infra-red LED. Some of the features of Figure 5.2 are already known from our study of the unmodulated 2DEG. For $B > 0.3\,\mathrm{T}$ the Shubnikov-de Haas oscillations are clearly visible and indicative of the high mobility of the 2DEG ($1.2 \times 10^6\,\mathrm{cm^2/Vs}$). The strong negative magnetoresistance background was also observed in the ungated device and ascribed to the effect of e-e interaction in the narrow channel. For $0.1\,\mathrm{T} < B < 0.5\,\mathrm{T}$ a new

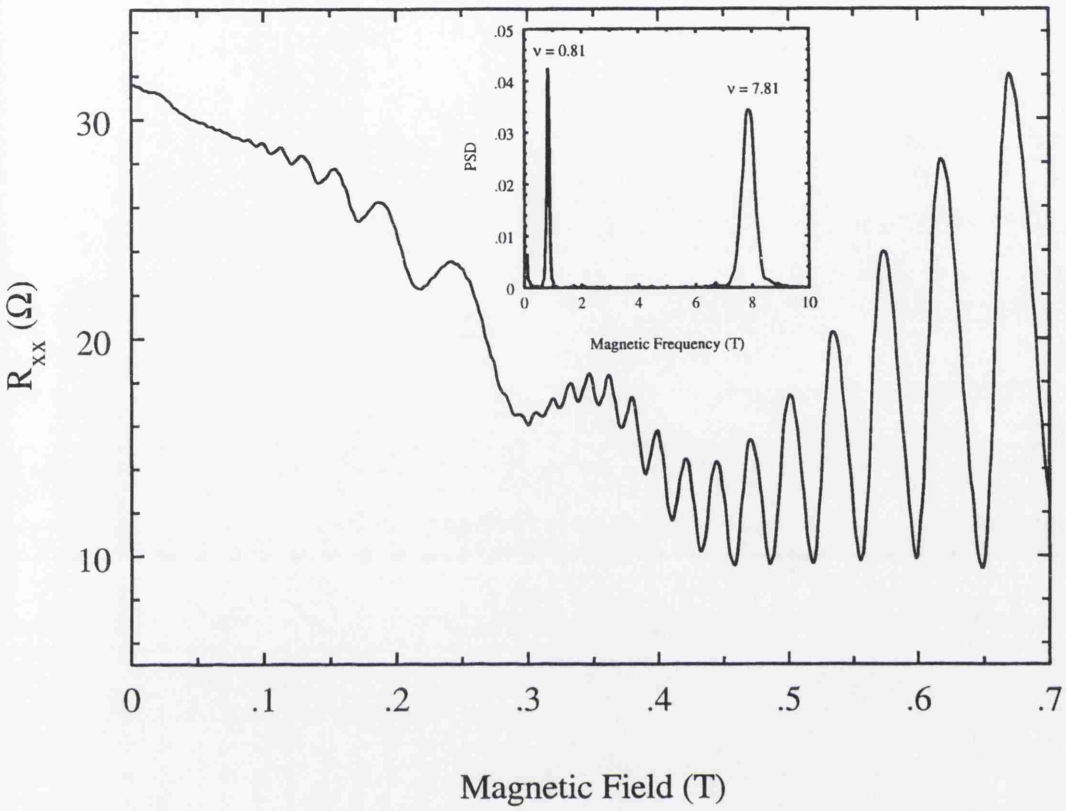

Figure 5.2: Magnetoresistance trace of a 250 nm-period LSSL device on a standard HEMT (2DEG depth: 90 nm) measured at $T = 70\,\mathrm{mK}$ with the gates connected to the source, after a brief IR illumination. Apart form the well-known SdH oscillations a new series of oscillations periodic in 1/B can be observed down to $B = 0.1\,\mathrm{T}$. A small local maximum is also observed at $B \approx 1.5 \times 10^{-2}\,\mathrm{T}$. All the structure is seen on a strong negative resistance background. Inset: a FFT power spectral density estimation of the magnetoresistance as a function of $1/B$.

series of oscillations develop which are periodic in $1/B$ and different from the SdH. These oscillations arise from the commensurability resonances between the cyclotron orbit and the periodic potential. They were first observed by Weiss et al. making use of the persistent photoconductivity effect in a sample under holographic illumination [9, 11], and by R. W. Winkler and J. P. Kotthaus in a microstructured gated device [10]. Finally, one should notice a small local maximum at $B \approx 0.015\,\mathrm{T}$ which does not coincide with the similar low field maximum associated with wall collisions observed in the unmodulated device. The origin of this local maximum is indeed different and it will be discussed below.

The power spectral density estimation (inset in Figure 5.2), calculated using Fast Fourier Transform techniques (see *Apendix*), clearly shows the spectral purity of the commensurability oscillations. As discussed above, this fact confirms the assumption of a purely sinosoidal effective potential at the 2DEG that is made in all available theories [10, 12, 13, 58, 59]. Equation 5.8 gives the relation between the position of the FFT peak and the device parameters

$$\nu = \frac{2\hbar\sqrt{2\pi N_{2D}}}{ae} \tag{5.14}$$

The 2DEG carrier density can be obtained from the FFT peak associated with the SdH oscillations using equation 4.35. We find for this device $N_{2D} = 3.8 \times 10^{11}\,\mathrm{cm}^{-2}$. Equation 5.14 predicts a magnetic frequency $\nu = 0.81\,\mathrm{T}$, in excellent agreement with the experimental data. The phase of the oscillations can be deduced from a plot of the values of B^{-1} at the maxima vs. the oscillation index. According to equation 5.8 magnetoresistance maxima occur at

$$\frac{1}{B_{max}} = \frac{1}{\nu}(k - \phi) \qquad (k = 1, 2, \ldots) \tag{5.15}$$

where $\phi = -0.25$. Figure 5.3 shows such a plot for the experimental data. The phase deduced from the zero intercept is $\phi_{exp} = -0.26$, in good agreement

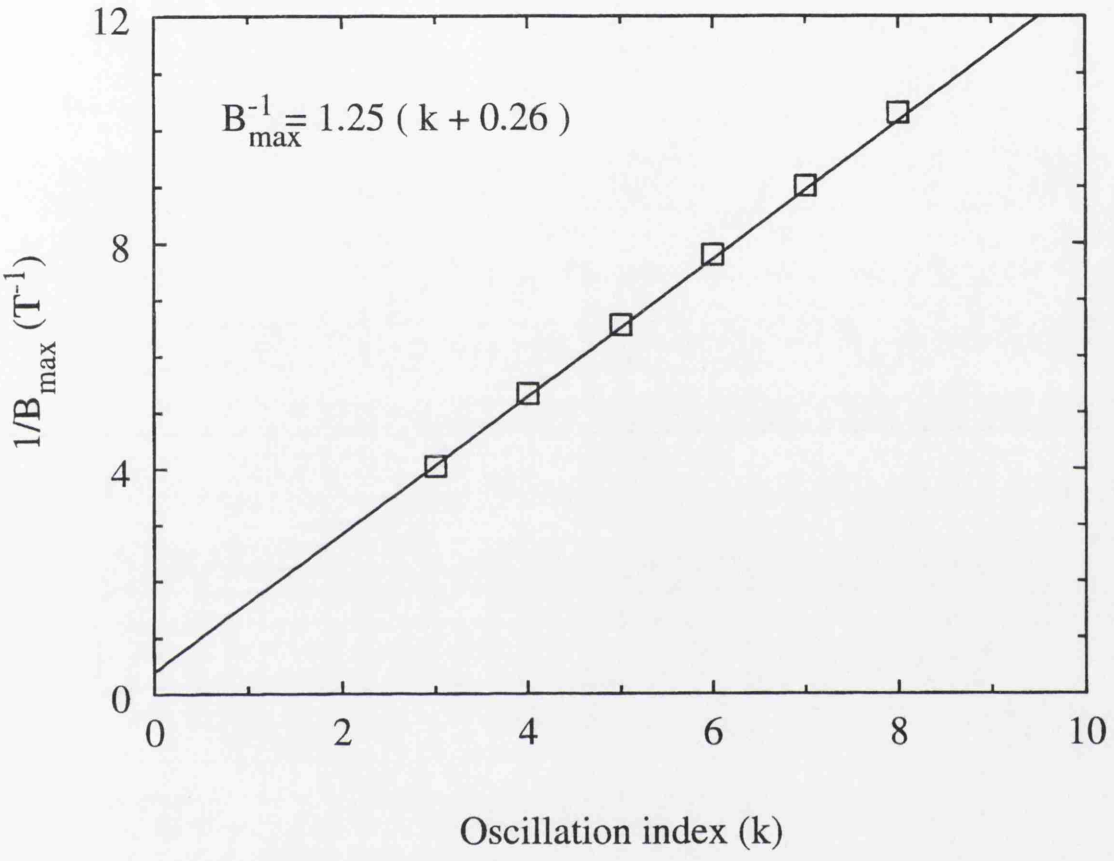

Figure 5.3: Plot of the inverse of the magnetic field at maxima of oscillations vs. the index of the oscillation. The inverse of the slope gives the magnetic frequency of the oscillations and the zero intercept determines the phase.

with the theoretical value $\phi = -0.25$. The determination of the phase of the oscillations is extremely sensitive to inaccuracies in the values of magnetic field since the values of B_{max} are small and they enter in the calculation as $1/B_{max}$. In the data presented in Figure 5.3 we have included a B-field lag of 4 mT to account for the delays introduced by the digital data acquisition process. The value is quite reasonable for the experimental set-up used in this measurement:

- B-field ramp rate $= 6 \times 10^{-2}$ T/min
- delay between measurements = 1 s
- measurement sequence = B-field, current Lock-in, voltage Lock-in

and is consistent for several data sets taken under the same conditions. Indeed, the value of the phase of commensurability oscillations could be used for fine-tuning the system for low-field precision measurements.

Further illumination of the device does not have any significant effect on the 2DEG carrier density but increases the mobility from 1.22×10^6 cm^2/Vs to 1.34×10^6 cm^2/Vs. The data is shown in Figure 5.4. The commensurability oscillations become stronger and better defined, and it is possible to distiguish up to the $k = 14$ oscillation (corresponding to a cyclotron orbit enclosing 14 periods of the superlattice).

The increase of electron mobility is due to the generation of free charge in the AlGaAs that improves the screening of the ionized impurities. The presence of a parallel sheet of low mobility electrons is apparent in the Shubnikov-de Haas oscillations. The parasitic channel gives rise to a parabolic increasing background resistance that precludes the observation of the zeros of ρ_{xx}.

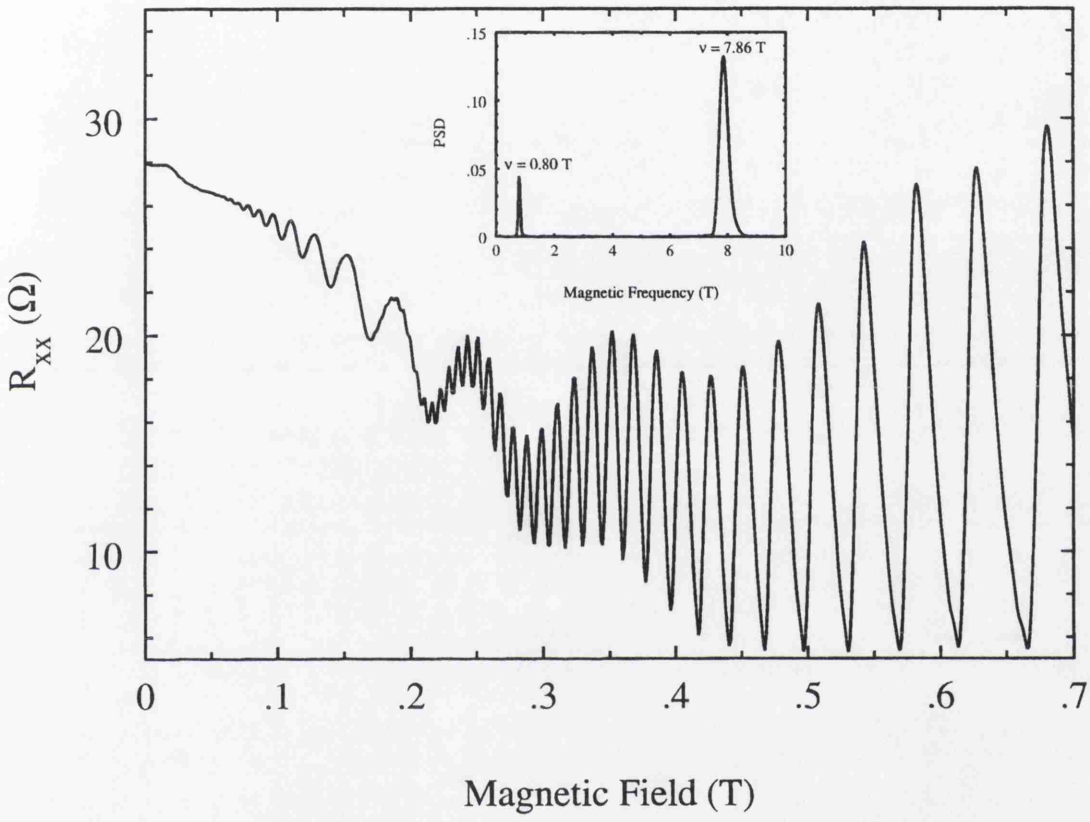

Figure 5.4: Measurement identical to the one shown in Figure 5.2 after IR illumination for 60 s. There is a significant increase of mobility due to the generation of free carriers in the AlGaAs layer that improve screening and the commensurability oscillations become much better defined.

5.2.2 The source of 2DEG modulation

In the light of the experimental observations we turn now to the origin of the 2DEG modulation. It is usually assumed [29, 56] that the metal-semiconductor contacts that constitute the gates induce a change in height of the Schottky barrier on the surface of GaAs which acts as an effective gate voltage, so that even at $V_g = 0$ there is some electrostatic modulation at the 2DEG. This is very unlikely in this device because it has a parasitic conducting layer between the gates and the 2DEG which is electrically connected to the 2DEG. Such a layer prevents the electric field generated at the gates from penetrating into the 2DEG region. Moreover, the improved screening of the impurities observed after a prolonged illumination of the device should screen out the electrostatic gate potential too, in contradiction with the experimental finding of much better defined commensurability oscillations. An alternative source of 2DEG modulation is the persistent photoconductivity effect. The array of gates acts as a mask so that the IR irradiation ionizes preferentially the donors in the spacings between the metal fingers. As a result, a modulated positive charge background appears in the AlGaAs doped layer which is responsible for an additional 2DEG periodic modulation. The screened electrostatic potential due to the modulated background of ionized donors is presumably very small, but because of its proximity to the 2DEG it has measurable effects. A prolonged illumination increases the number of ionized donors between the fingers giving rise to an electrostatic potential that adds to the gate potential. This mechanism explains the enhancement of the commensurability oscillations seen in our devices after IR illumination (compare Figures 5.2 and 5.4). The persistent photoconductivity effect was first used to achieve a periodic modulation in a 2DEG in D. Weiss' original experiment [9, 11], where commensurability oscillations were measured on an ungated device under holographic illumination.

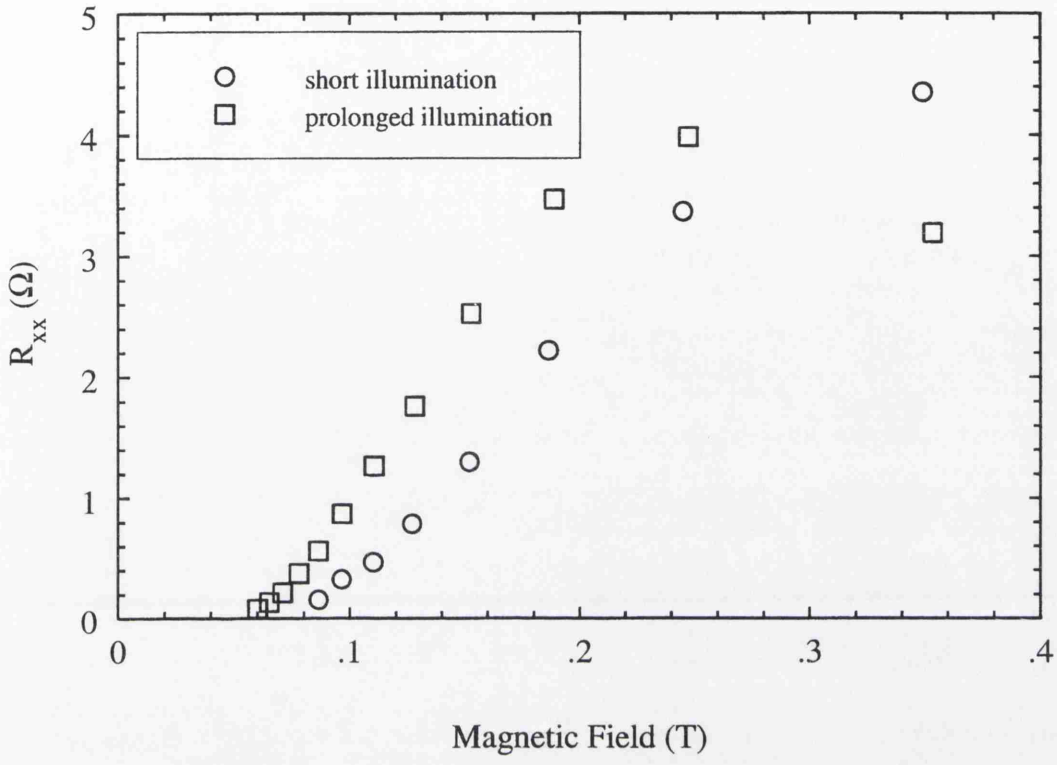

Figure 5.5: Amplitude of the commensurability oscillations vs. magnetic field for different duration of the IR illumination. The deviation from linear behaviour clearly seen in the prolonged illumination data is due to the interaction of Landau quantization with the mechanism leading to the commensurability oscillations.

From equation 5.8 we can obtain an estimation of the strength of the 2DEG modulation. The experimental oscillation amplitudes decay more rapidly with decreasing magnetic field than predicted by theory . This feature is common to all published data [10, 11, 14, 29] and it is not well understood. Certainly the theory breaks down at $B \to 0$, but even in the range $0.1\,\mathrm{T} < B < 0.3\,\mathrm{T}$ the amplitudes decay faster than B. In Figure 5.5 we have plotted the amplitudes of the commensurability oscillations vs. magnetic field for the device

after a short illumination and after a prolonged illumination. When Landau quantization is not resolved, the amplitudes have an approximately linear dependence in magnetic field $\sim (B - B_0)$ with a lower cut-off value B_0 for the higher mobility sample. We attribute this behaviour to the effect of scattering in uncorrelating the drifts acquired by the electrons. Physically, the resistivity correction 5.8 is proportional to B because smaller cyclotron orbits cross more frequently the extremal points and therefore accumulate more uncompensated drift than larger ones, in which the alternating drift cancels out along most of their length. If scattering prevents the completion of cyclotron orbits the drifts acquired by an electron are uncorrelated and the oscillations vanish. When the mean free path is large enough to permit the accumulation of the $\mathbf{E} \times \mathbf{B}$ drifts along the orbit at B_0 the oscillations begin and their amplitude increases linearly with B. The cut-off values deduced from Figure 5.5 are consistent with the condition

$$2\pi R_c|_{B_0} \approx l \tag{5.16}$$

At magnetic fields where the Landau quantization is resolved there is a significant decrease in the commensurability oscillation amplitudes. In fact, in Figures 5.2 and 5.4 only oscillations with $k \geq 3$ are visible. In fact, oscillations $k = 1$ and $k = 2$ (corresponding to cyclotron orbits enclosing one and two superlattice periods, respectively) are completely buried in SdH oscillations. The interaction between Landau level quantization and the mechanism leading to the commensurability oscillations can only be explained within a model that treats Shubnikov-de Haas and commensurability oscillations on the same footing. The fully quantum-mechanical theory of C. Zhang and R. R. Gerhardts [13] is based on the self-consistent Born approximation for the scattering by random impurities. The Shubnikov-de Haas oscillations arise from the variations in the scattering rate due to the oscillatory B-field dependence of the density of states at the Fermi level. As discussed above, the periodic modula-

tion of the 2DEG leads to the formation of Landau bands of oscillating width (see Equation 5.12). Since the number of states per Landau level depends only on the magnetic field, the oscillation of the Landau bandwidth leads to a modulation of the peak height of the density of states, with maxima near flat-band energies. The DOS modulation is directly reflected in the resistivity via the scattering rate, giving rise to the commensurability oscillations. The resistivity correction is proportional to the thermal average of the density of states *squared.* In the unmodulated system at low magnetic fields, when $k_B T > \hbar\omega_c$, the thermal average extends over several Landau levels and since all Landau levels contain the same number of states the DOS oscillations are completely washed out. By contrast, in the modulated case, the area under the peaks of $D(E)^2$ strongly depends on the Landau bandwidth and the thermal average enhances the oscillatory behaviour. At higher fields, where the individual Landau bands are well resolved, the thermal average extends only over a single peak and the Shubnikov-de Haas oscillations dominate the magnetoresistance. Because of the numerical nature of the results presented in Ref. [13] a direct comparison with our experimental data is not possible. However, the calculated resistivity plotted in Figure 5 of Ref. [13] clearly shows an amplitude reduction of those commensurability oscillations that coexist with Shubnikov-de Haas oscillations, in agreement with our experimental results.

We estimate the modulation strength using the amplitude of the $k = 5$ oscillation, the one having largest amplitude and being free of superimposed SdH oscillations. From Equation 5.8 we obtain $V_{eff} \approx 0.10\,\mathrm{meV}$ for the short illumination and $V_{eff} \approx 0.13\,\mathrm{eV}$ for the prolonged illumination case. In view of the preceeding discussion on the B-field dependence of the amplitudes it would be appropriate to substitute B by $(B - B_0)$ in the prefactor of expression 5.8. In that case, we obtain $V_{eff} \approx 0.14\,\mathrm{meV}$ and $V_{eff} \approx 0.15\,\mathrm{meV}$ for the short and prolonged illumination, respectively.

5.2.3 Streaming orbit effects

Finally we look at the small local maximum of the magnetoresistance at $B \approx 0.015\,\mathrm{T}$. It is due to the confinement of the electron trajectories along the equipotential lines [29]. The effect has been seen in samples with a stronger modulation as a positive magnetoresistance at $B \to 0$ [11, 14, 29]. An explanation based in the formation of *streaming orbits* has been put forward by P. H. Beton et al. [29]. Streaming orbits are formed at low magnetic fields when the Lorentz force is not strong enough to overcome the potential barriers of the periodic potential and the electron is confined between two equipotential lines. The electrons trapped in streaming orbits travel in the y-direction with a velocity $v \approx v_F$ and therefore have a significant contribution to σ_{yy} ($\propto \rho_{xx}$). The effect disappears for $B > B_c$ where

$$B_c = \frac{1}{v_F}\frac{2\pi}{a}V_{eff} \tag{5.17}$$

is the magnetic field for which the Lorentz force is larger than the electric force at all points of the orbit. Equation 5.17 gives an independent estimation of the periodic potential strength. For the parameters of device A648 we obtain, from equation 5.17, $V_{eff} \approx 0.16\,\mathrm{meV}$, in excellent agreement with the estimation based on the amplitude of commensurability oscillations.

5.3 Commensurability oscillations in a shallow HEMT

In this section we present the results obtained in a LSSL device fabricated on the shallow HEMT material A601. In this novel layer design the 2DEG is formed at an interface only 28 nm below the surface so that a sharper periodic

Table 5.3: Values of carrier concentration and mobility in the A601 shallow HEMT layer at $T = 70\,\mathrm{mK}$.

	Hall Bar		Gated device	
	Dark	Illuminated	Dark	Illuminated
N_{2D} (cm^{-2})	3.33×10^{11}	3.33×10^{11}	3.29×10^{11}	3.35×10^{11}
$\mu(\mathrm{cm}^2/\mathrm{Vs})$	6.37×10^5	7.83×10^5	3.28×10^5	5.43×10^5

potential at the 2DEG is expected. The layer A601 showed a surprisingly high mobility for the reduced thickness of the spacer layer (see Table 5.3). We think that this unusually high value of mobility is due to a low mobility sheet of electrons around the δ-doping layer that screens the ionized impurity potential. Since the mobility of the electrons in the parasitic channel is very low they do not contribute to transport and parallel conduction is not detected in the Shubnikov-de Haas oscillations (see Figure 4.7). The parallel sheet of electrons contributes to an additional screening of the electrostatic potential of the surface gates.

5.3.1 Experimental data

Figure 5.6 shows the magnetoresistance of an A601 LSSL device with the gates connected to the source. The commensurability oscillations are far from being sinusoidal and the FFT Power Spectral estimation[1] reveals a very strong second Fourier component, indicative of an enhanced coupling with the gate potential. The presence of the second Fourier component is even more apparent in

[1] The magnetoresistance was differentiated before the FFT. This increases the relative magnitude of the second harmonic.

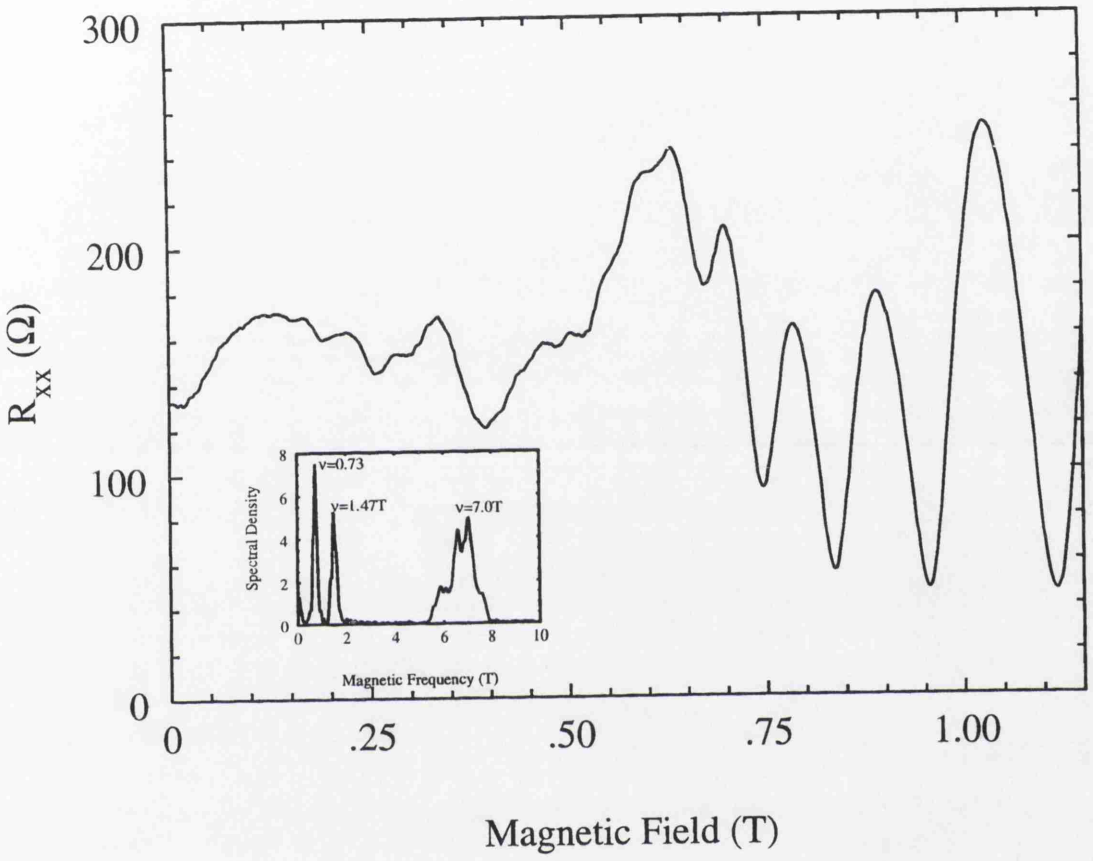

Figure 5.6: Commensurability oscillations measured in a 2DEG confined at 28 nm below the surface. The period of the superlattice was 265 nm and the measurements were performed at $T = 70$ mK, in the dark and with the gates connected to the source. Inset: Power Spectral Density of the data as a function of $1/B$. It clearly shows a strong second Fourier component that reflects the enhanced contrast of the modulation potential.

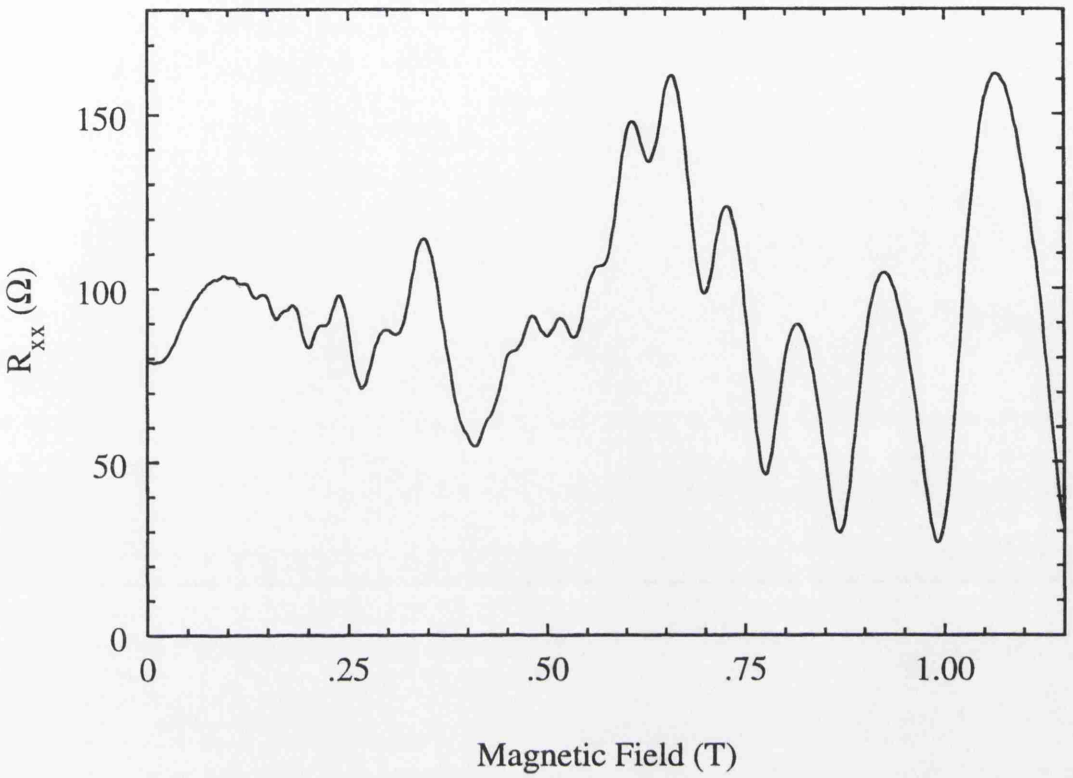

Figure 5.7: Commensurability oscillations measured in the device A601 after a short illumination. There is a significant increase of the electron mobility that results in better defined oscillations down to lower fields.

the data taken after a short illumination (Figure 5.7). The improved definition of the commensurability oscillations is caused by the increase of electron mobility due to a more effective screening of the impurity potential by photoexcited electrons around the donors. Again, we can estimate the strength of the modulating potential from the amplitudes of the commensurability oscillations. First we have to separate the first and second Fourier components of the magnetoresistance data. We achieve this by digitally filtering the data using FFTs (see *Appendix*). Figure 5.8 demonstrates the filtering process with the data of Figure 5.7. In Figure 5.9 we have plotted the amplitude of each Fourier component vs. magnetic field. Both components show a linearly incre-

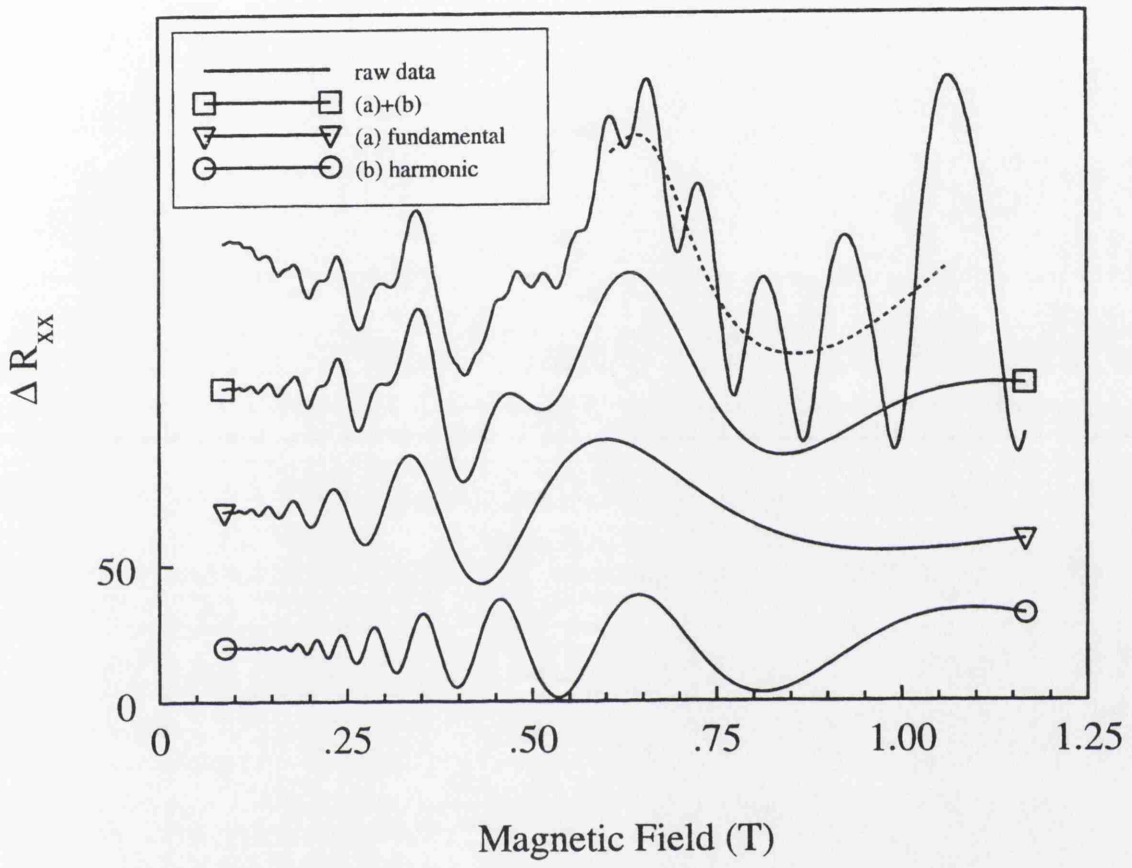

Figure 5.8: Separation of the magnetoresistance data (top curve) into first and second Fourier components using digital filtering based on FFT techniques. The dashed line that joins the midpoints of the Shubnikov-de Haas oscillations is a guide to the eye. Adding up the two filtered components the original commensurability oscillations are recovered.

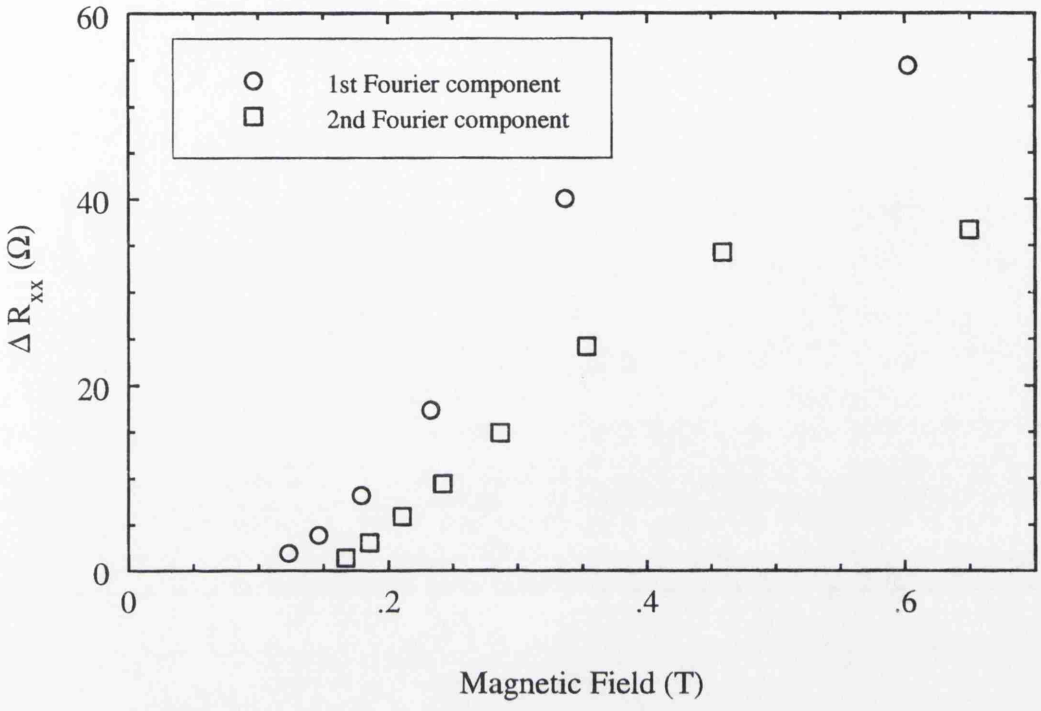

Figure 5.9: Amplitude of first and second Fourier components of the commensurability oscillations measured on A601 at 70 mK against magnetic field.

asing amplitude at intermediate magnetic fields with approximately the same extrapolated cut-off value. At low magnetic fields ($B < 0.15\,\mathrm{T}$) the second Fourier component is quenched more rapidly because the electrons sample a great number of periods and therefore they are more sensitive to fabrication irregularities in the superlattice. At high magnetic fields ($B > 0.4\,\mathrm{T}$) the effect of Landau quantization reduces the amplitude of both Fourier components. We use the amplitude of the oscillation at $B \approx 0.35\,\mathrm{T}$ to estimate the amplitude of the first and second Fourier components of the potential at the 2DEG. We summarize the results in Table 5.4.

The potential amplitude estimated from the position of the low field magnetoresistance maximum (Equation 5.17) is $V_{eff} \approx 1.3$ meV in the dark and

Table 5.4: Estimation of the Fourier components of the effective periodic potential at the 2DEG. In the "corrected" values $V_c^{(i)}$ an allowance is made to account for the deviations of the measured amplitudes from the linear B-dependence predicted by theory.

	$V^{(1)}$(meV)	$V^{(2)}$(meV)	$V_c^{(1)}$(meV)	$V_c^{(2)}$(meV)
In the dark	0.54	0.27	0.71	0.35
After illum.	0.45	0.24	0.58	0.31

$V_{eff} \approx 1.0\,\text{meV}$ after illumination. These values, corresponding to the total effective potential, are in good agreement with the "corrected" values for the Fourier components listed in Table 5.4 and support the *ad hoc assumption* of considering a cut-off magnetic field in the amplitude prefactor. In any case, the effective potential has an unusually strong second Fourier component. We shall look closely at this feature in the next subsection.

5.3.2 The source of 2DEG modulation

The results obtained in the shallow LSSL device present the challenge of finding out the origin of a modulation with such a high harmonic content. The simplest model of a LSSL consists of a Dirichlet problem with the boundary conditions specified by (see Figure 5.10)

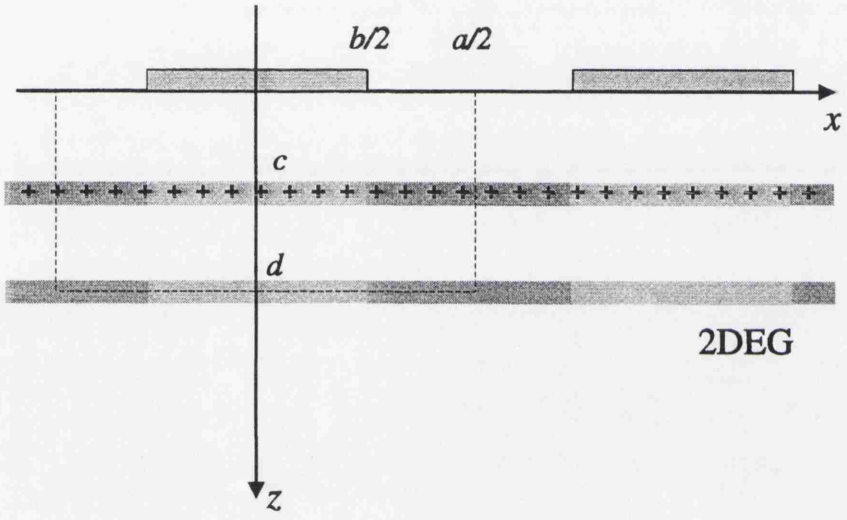

Figure 5.10: Schematic cross-section of a LSSL device showing the unit cell for the electrostatic calculation.

$$\phi^g(x,0) = \begin{cases} V_g & |x| < \dfrac{b}{2} \\ \\ 0 & |x| > \dfrac{b}{2} \end{cases} \tag{5.18}$$

The model defined by the boundary conditions 5.18 is known as a "pinned" surface model since it assumes that the free surfaces remain pinned to E_F in the 2DEG. This simple model was used by J. P. Kotthaus and D. Heitman to discuss the feasibility of fabricating LSSL devices on different semiconductor substrates [55]. The general solution of the Laplace equation that satisfies the boundary conditions 5.18 can be written as

$$\phi^g(x,z) = \frac{1}{2}\phi_0^g + \sum_{m=1}^{\infty} \frac{2V_g}{\pi m} \sin\left(q_m \frac{b}{2}\right) \cos(q_m x) \exp(-q_m z) \tag{5.19}$$

where $q_m = 2\pi m/a$. It has to be noted from Equation 5.19 that the higher order Fourier components are attenuated exponentially with depth so that for standard HEMT layers only the $m = 1$ component is significant and the usual assumption of a sinusoidal potential [9, 10, 11] is justified. Moreover, we see from equation 5.19 that the attenuation is stronger for shorter period potentials. Short-period superlattices can only be effective on shallow HEMT layers in which $a/d \gg 2\pi$. Another feature of expression 5.19 is that for a ratio $a/b \approx 2$, as is the case in our devices, the potential at the 2DEG has a very low content of even Fourier components. Thus, we already see that a purely electrostatic model will have difficulties explaining the experimental results.

The effective periodic potential is further smoothed due to the screening by the 2DEG. The screening properties of the 2DEG at low magnetic fields can be described using Thomas-Fermi theory (linear approximation) [47, 60, 56]. The Fourier components of the 2D potential induced by an external perturbation

on a 2DEG embedded in an infinite medium can be written as

$$V(q,d) = \frac{V_{ext}(q)}{\epsilon(q,d)} \tag{5.20}$$

where the dielectric function is given by

$$\epsilon(q,d) = 1 + \frac{Q}{q} \tag{5.21}$$

and the Thomas-Fermi wave vector is

$$Q = 2\pi \frac{e^2}{\epsilon} \frac{m}{\pi\hbar^2} \equiv \frac{2}{a_B} \tag{5.22}$$

with a_B the effective Bohr radius ($a_B = 9.8\,\text{nm}$ for GaAs). In a real HEMT layer the equipotential at the surface reduces the effectiveness of screening at long wavelengths (through image charge) and it yields

$$\epsilon(q,d) = 1 + \frac{2}{a_B q}[1 - \exp(-2qd)] \tag{5.23}$$

The polarization of the parasitic channel of electrons around the δ-doping layer, at a distance $c \approx 17\,\text{nm}$ below the surface, provides an additional screening of the surface gate potential. The charge density induced can be calculated in the Thomas-Fermi approximation as

$$\sigma_m = -e^2 \frac{m}{\pi\hbar^2} V_m(c) \tag{5.24}$$

The polarization originates an additional contribution to the self-consistent potential

$$V_m(par) = \frac{2\pi\sigma_m}{\epsilon q_m} \exp[-q_m(d-c)] - \exp[-q_m(d+c)] \tag{5.25}$$

Taking into account this contribution, the effective dielectric function can be found to be [56]

$$\epsilon_{eff}(q,d) = \epsilon(q,c)\epsilon(q,d) - \exp[-2q(d-c)][\epsilon(q,c) - 1]^2 \tag{5.26}$$

The numerical values for the A601 device are

$$\epsilon(\frac{2\pi}{a}, d) = 28.8 \quad \epsilon(\frac{4\pi}{a}, d) = 18.1$$

The experimental finding of a relatively strong modulation even at $V_g = 0$ could be explained by the change of the surface Schottky barrier height due to the formation of the metal-semiconductor contact that would act as an effective gate voltage. For $V_g = 0.1\,\mathrm{V}$ the screened potential Fourier components in the 2DEG are $V(q,d) = 1.14\,\mathrm{meV}$ and $V(2q,d) = 2.76 \times 10^{-2}\,\mathrm{meV}$. $V(q,d)$ is of the right order of magnitude but the ratio $V(2q,d)/V(q,d)$ is far too small.

The use of the "pinned" model appears to be justified since the sample was cooled from room temperature with the gates connected to the source. At room temperature charge can move to the surface to keep its potential constant. At low temperatures the charge is likely to be "frozen" and the free surfaces should be treated as dielectric boundaries with a fixed charge density in response to an applied gate voltage. This complicates the electrostatics, since it yields mixed boundary conditions

$$\left.\begin{array}{ll} \phi = V_g & |x| < \frac{b}{2} \\ \frac{\partial \phi}{\partial n} = 0 & |x| > \frac{b}{2} \end{array}\right\} \tag{5.27}$$

The "frozen" surface model, which has been analitically solved by J. H. Davies and I. A. Larkin [56], yields a higher second Fourier component than the "pinned" model but it is still much smaller than our estimations from experimental data. In Figure 5.11 we compare the potential at the 2DEG, reconstructed from experimental oscillation amplitudes, with the predictions

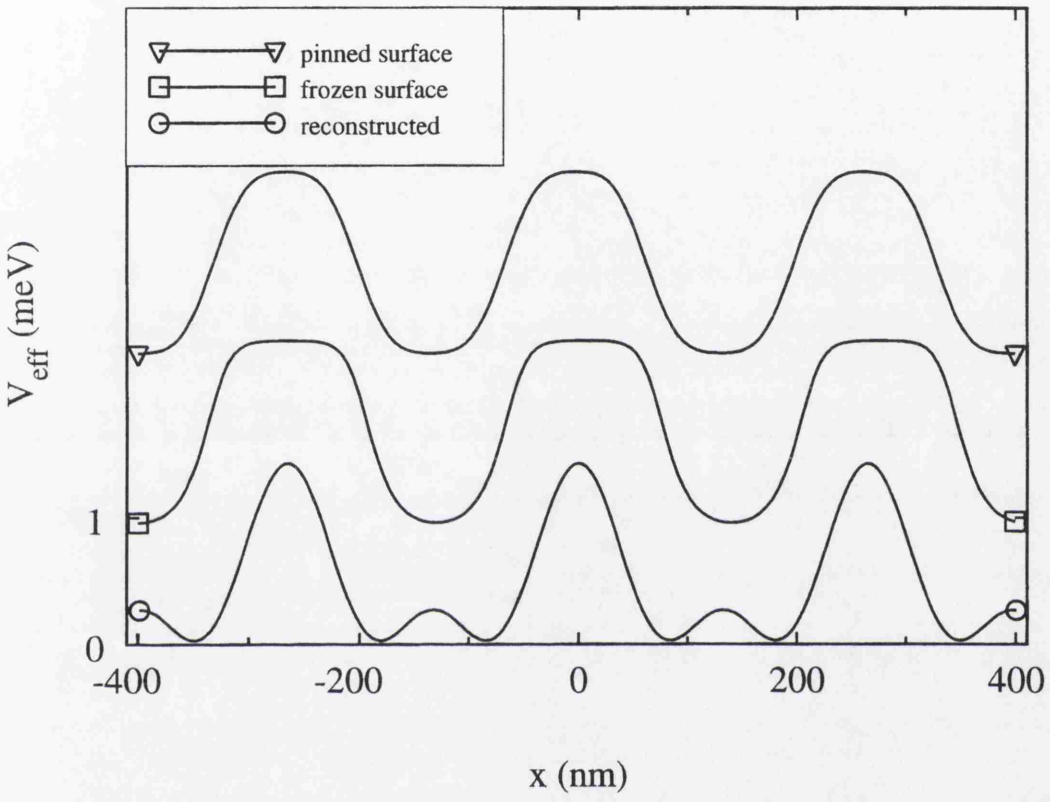

Figure 5.11: Comparison of the 2DEG potential recostructed from experimental data with the results of "pinned" and "frozen" electrostatic theory. The "pinned" model gives a perfectly symmetric potential practically without even Fourier components. The "frozen" model gives an asymmetric profile, with narrower troughs, but the ratio between the second and the first Fourier components is still far below the experimental estimation.

of the "pinned" and "frozen" electrostatic models. It is clear that electrostatic models cannot explain the harmonic contents of the commensurability oscillations measured in the shallow HEMT device.

Elastic strain [14, 56] has been suggested as an alternative source of periodic potential in LSSL devices. The surface gates are made of thin layers ($\approx 15\,\text{nm}$) of Ti and Au evaporated on the semiconductor at a high but not precisely known temperature. The different average values of the coefficient of expansion of GaAs and Ti ($\alpha_{GaAs} \approx 4 \times 10^{-6}\text{K}^{-1}$ and $\alpha_{Ti} \approx 7 \times 10^{-6}\text{K}^{-1}$) causes a differential shrinking of Ti of the order of 10^{-3} as the device is cooled down to fridge temperatures. The resulting compression on the GaAs produces a change in energy of the band edge which, given the deformation potential constant in GaAs, $\Xi \approx -8\,\text{eV}$, may come close to 8 meV. Screening by the 2DEG reduces the effective potential to about 1 meV, the right order of magnitude for the amplitude of the oscillations measured in the experiment.

An elastic strain theory for an array of gates has recently been developed by J. H. Davies and I. A. Larkin [56]. We give next a brief outline.

The relation between stresses and strains is given by Hooke's law [61]

$$E\eta_{ii} = P_{ii} - \sigma(P_{jj} + P_{kk}) \tag{5.28}$$

where E is Young's modulus and σ the Poisson's ratio. The components of the stress tensor P_{ij} can be written as [62]

$$P_{xx} = \frac{\partial^2\chi}{\partial y^2}, \quad P_{xy} = -\frac{\partial^2\chi}{\partial x \partial y}, \quad P_{yy} = \frac{\partial^2\chi}{\partial x^2} \tag{5.29}$$

where $\chi(x, y)$ is an arbitrary function that verifies the biharmonic equation.

By symmetry we assume that η and P depend only on x and y, and that $\eta_{zz} = 0$. Under these assumptions, the dilation can be written as

$$E\delta = E(\eta_{xx} + \eta_{yy}) = (1+\sigma)(1-2\sigma)(P_{xx} + P_{yy}) \tag{5.30}$$

The boundary conditions are taken to be

$$\begin{aligned} \frac{\partial^2 \chi}{\partial y^2} &= \frac{E}{1-\sigma^2}\eta^0_{xx} \quad \text{under the gates} \\ \frac{\partial^2 \chi}{\partial x \partial y} &= 0 \qquad \text{between the gates} \\ \frac{\partial^2 \chi}{\partial x^2} &= 0 \qquad y = 0 \end{aligned} \tag{5.31}$$

With the substitution $\chi = y\phi$, where ϕ satisfies Laplace's equation, the dilation is given by

$$\delta = \frac{2(1+\sigma)(1-2\sigma)}{E}\frac{\partial \phi}{\partial y} \tag{5.32}$$

and the problem is defined by the boundary conditions

$$\begin{aligned} \frac{\partial \phi}{\partial y} &= \frac{E}{2(1-\sigma^2)}\eta^0_{xx} \quad \text{under the gates} \\ \frac{\partial \phi}{\partial x} &= 0 \qquad \text{between the gates} \end{aligned} \tag{5.33}$$

The problem with mixed boundary conditions can be solved using a pair of conformal sine transformations $z \rightarrow w$ [56] that map the boundaries between the regions with zero potential and zero normal derivative on the corners of a semi-infinite square region. In that map, $\Im w$ is a trivial solution to the boundary value problem and by inverting the transformations the solution of Laplace's equation $\phi(z)$ is readily obtained

$$\phi(z) = z + \frac{a}{\pi}\arccos\frac{\cos[\pi z/a]}{\cos[\frac{1}{2}\pi(a-b)/a]} \tag{5.34}$$

The bare potential is finally given by

$$V(x) = \Xi\delta = \Xi\eta_{xx}^{0}\frac{1-2\sigma}{1-\sigma}\Re\frac{dw}{dz} \tag{5.35}$$

where

$$\frac{dw}{dz} = 1 - \frac{\sin\left(\frac{1}{2}\pi z/(a+b)\right)}{\sqrt{\sin^2\left[\frac{1}{2}\pi z/(a+b)\right] - \sin^2\left[\frac{1}{2}\pi a/(a+b)\right]}} \tag{5.36}$$

Screening by the 2DEG reduces the Fourier components of the bare potential by a factor given by the inverse effective dielectric constant (Equation 5.23). In Figure 5.12 we compare the screened strain potential calculated for $\Xi = -8\,\mathrm{eV}$, $\eta_{xx}^{0} = -2.3 \times 10^{-3}$, $\sigma = 0.31$, with the reconstructed potential inferred from commensurability oscillations. The agreement with the measured potential is very good. The ratio between the second and the first Fourier components is $V_{str}^{(2)}/V_{str}^{(1)} \approx 0.43$, very close to the value $V^{(2)}/V^{(1)} \approx 0.53$ deduced from the experiment. The deformation potential due to the surface gates gives a high second Fourier component even in the case of a ratio between gate width and spacing close to one and thus constitutes the best explanation of the potential measured in the experiment.

5.4 Gate bias dependence

We have seen that the main source of modulation in the LSSL devices studied in this work is not the electric field induced by the surface gates as it was originally intended. This constitutes a serious limitation for the performance of the devices as tunable 2DEG modulators since the "controllable" electric field from the gates has to compete with an "uncontrollable" background modulation that is relatively strong. In this section we study the effect that a bias applied to the gates has on the 2DEG modulation.

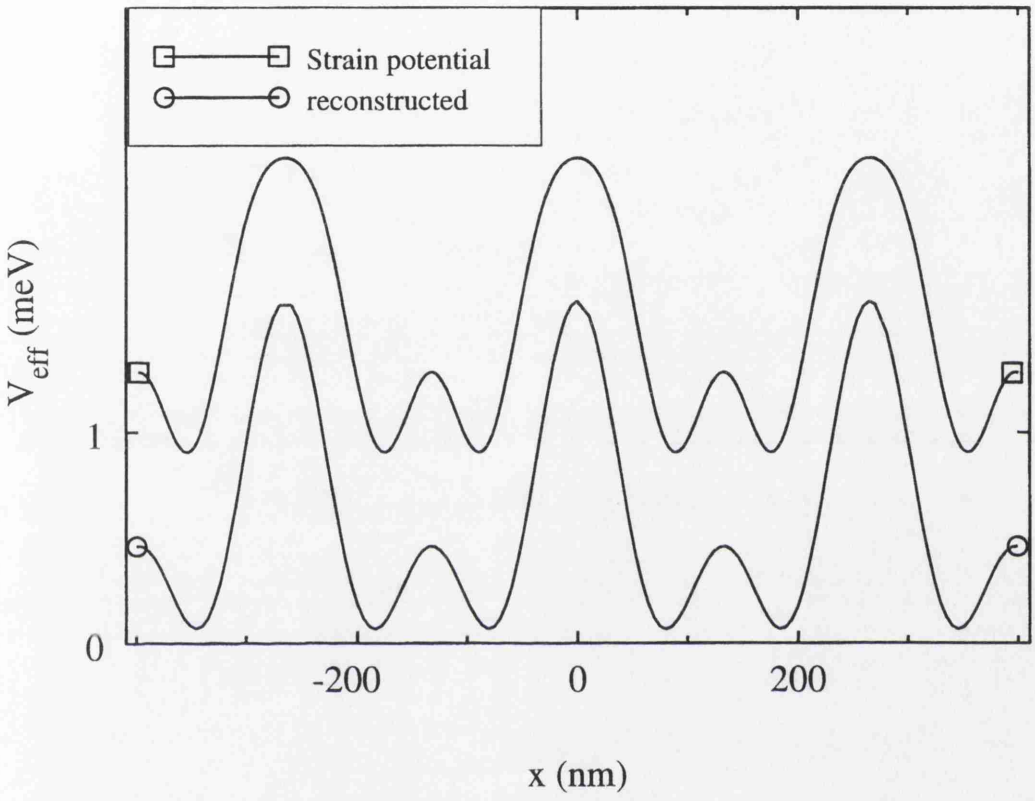

Figure 5.12: Comparison between the reconstructed potential and the theoretical screened potential arising from the differential contraction of the surface metal gates. The agreement with the experimental results is quite good. The deformation potential appears to be the best explanation of the potential measured in the experiment.

A601 device

The relatively high mobility of this shallow layer is due to a parasitic sheet of electrons around the donors in the δ-doping layer that screens the random impurity potential. This parasitic sheet does not contribute to transport as demonstrated by the good Shubnikov-de Haas zeroes measured in this layer. We may assume that the ohmic contacts provide good electric contact to the 2DEG and a very poor contact to the parasitic layer, which acts merely as an additional source of screening for the surface gate potential. We have demonstrated that the main source of modulation at $V_g = 0$ is the deformation potential. The metal gates compress the GaAs and this results in sharp potential barriers under the gates and double minima in the spacings between the gates (see Figure 5.12). Any electrostatic potential due to the gates will be superimposed to this background modulation.

Figure 5.13 shows the low-field magnetoresistance traces for different gate voltages. We point out some significant features:

1. As seen from the periodicity of the Shubnikov-de Haas oscillations there is very little change of 2DEG carrier density with gate bias. However the longitudinal resistance consistently increases with negative gate bias.

2. The low-field positive magnetoresistance increases and it peaks at a higher value of B_c with increasingly negative gate bias.

3. The amplitude of the commensurability oscillations decreases with negative gate bias and increases with positive gate bias.

4. At high negative gate bias a series of $1/B$ oscillations, that were not present at $V_g = 0$, develop in the range $0.4\,\mathrm{T} < B < 0.7\,\mathrm{T}$.

From the experimental data we conclude that the negative gate bias has two main effects. On one hand it enhances the potential barriers under the

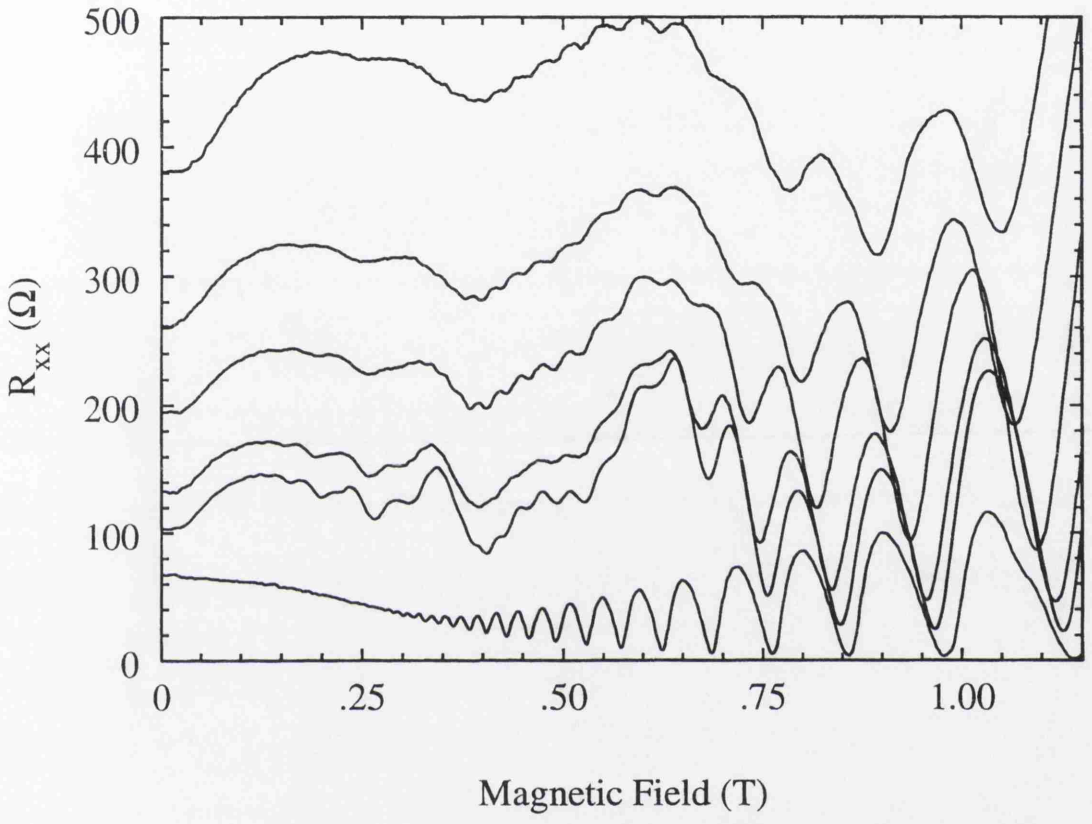

Figure 5.13: Commensurability oscillations measured at $T = 70\,\mathrm{mK}$ for different gate voltages. From top to bottom, $V_g = -0.2\,\mathrm{V}$, $-0.15\,\mathrm{V}$, $-0.1\,\mathrm{V}$, $0\,\mathrm{V}$, $+0.1\,\mathrm{V}$, and ungated device.

gates and on the other hand it depletes the parasitic channel. As a result, the screening of the random impurity potential becomes less effective and there is a drop of electron mobility while the 2DEG density changes very little. The effect of the mobility drop on the amplitude of the commensurability oscillations [4] compensates the increase of the periodic potential amplitude and the overall amplitude of the magnetoresistance oscillations decays with negative gate bias. The increase of the low-field positive magnetoresistance and the shift of B_c to higer values clearly indicates the increase of the amplitude of the periodic modulation. As an illustration we can estimate the increase of potential amplitude from the position of the peak of low-field positive magnetoresistance using Equation 5.17. We obtain

$$V_{eff}(V_g = -0.2\,\mathrm{V})/V_{eff}(V_g = 0\,\mathrm{V}) \approx 1.6$$

This amplitude increase is compensated by the mobility drop, that can be estimated from the increase in $B = 0$ resistance. We obtain

$$l(V_g = -0.2\,\mathrm{V})/l(V_g = 0\,\mathrm{V}) \approx R_0(V_g = 0\,\mathrm{V})/R_0(V_g = -0.2\,\mathrm{V}) \approx 0.3$$

Since $\delta R/R_0 \propto (V_{eff}l)^2$ the combined effect of δV_{eff} and $\delta\mu$ yields an oscillation amplitude reduction of $\delta R/\delta R_0 \approx 0.8$. The actual reduction measured in the experiment is higher ($\delta R/\delta R_0 \approx 0.5$) because the low mobility makes $l < 2\pi R_c$ and the theory breaks down. The application of a positive gate bias has the opposite effect. It draws electrons to the parasitic layer that improve screening and as a result there is a mobility increase and the enhancement of the commensurability oscillations. However, in this case, the electrostatic potential lowers the strain-potential barriers under the gates and therefore enhances the double-minima feature of the strain potential in the spacings between the gates (see Figure 5.12). This can be seen in the Fourier Transforms of Figure 5.14. A positive gate bias enhances the mobility and as a consequence

[4]The amplitude of commensurability oscillations is proportional to the mean free path squared

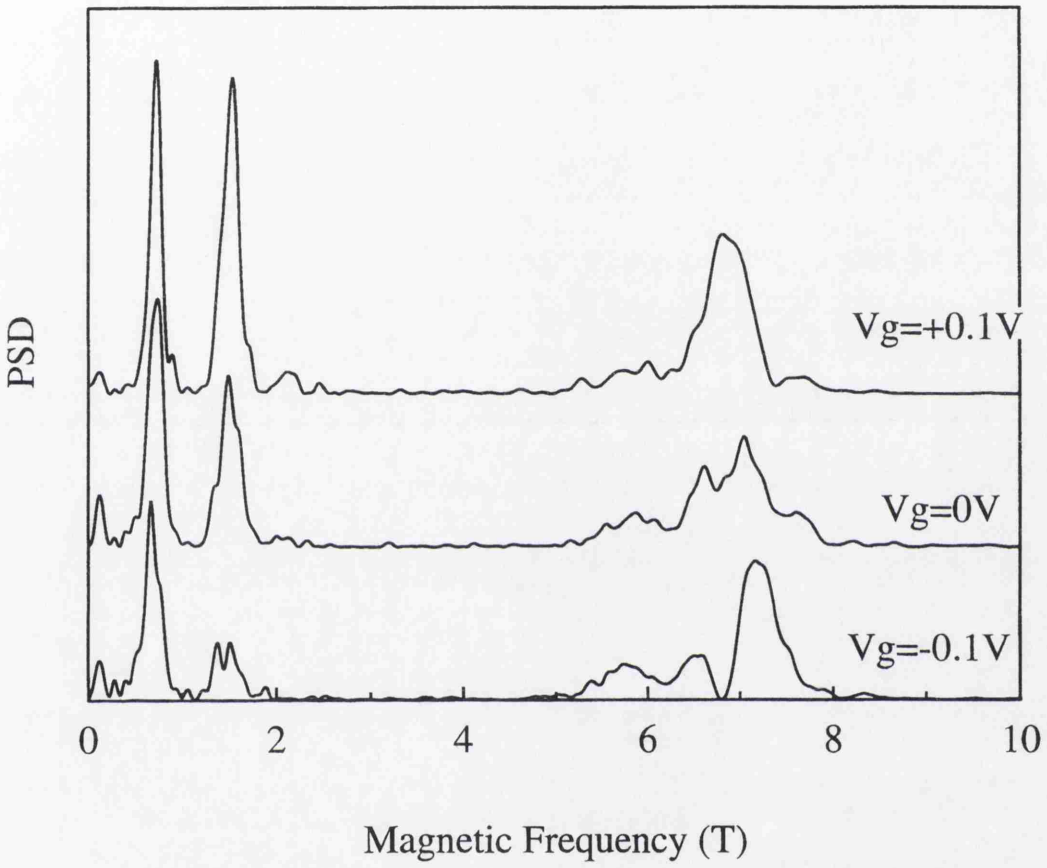

Figure 5.14: Fourier Transforms of the commensurability oscillations for different gate voltages. A positive gate bias increases the overall amplitude of the FFT peaks and the relative strenght of the harmonic. By contrast, a negative gate bias reduces the relative strenght of the harmonic. This behaviour can be explained by the combined effect of the electrostatic potential due to the gate bias and the strain potential.

the amplitude of the commensurability oscillations increases. This is reflected in the overall height of the FFT peaks. It also increases the relative strength of the second Fourier component because the electrostatic potential tends to reduce the strain-potential barriers under the gates so that the double-minima structure, responsible for the high harmonic contents of the magnetoresistance oscillations, becomes more pronounced. On the other hand, a negative gate bias depletes the parasitic layer and increases the strain-potential barrier under the gates. The overall amplitude of the FFT peaks is reduced because of the mobility drop, and a further reduction of the relative amplitude of the second Fourier component is observed, due to the contribution of the electrostatic potential.

In Figure 5.15 we have plotted the amplitude of the first and second Fourier components of the magnetoresistance oscillations as a function of gate bias. The trend of monotonically decreasing amplitudes with negative gate bias is apparent. Deviations from this trend are observed in the $k = 1$ fundamental oscillation and in the $k = 2$ harmonic oscillation. These are probably due to the quenching of the SdH oscillations with negative gate bias that prevents the interference of Landau quantization with the mechanism leading to the commensurability oscillations.

Finally we comment on the oscillations periodic in $1/B$ that start to develop at high negative gate bias between $B = 0.4\,\mathrm{T}$ and $B = 0.7\,\mathrm{T}$. These oscillations cannot be the usual SdH because the negative gate bias degrades the mobility and tends to quench SdH oscillations. Moreover, their periodicity is slightly higher than the periodicity of the true SdH observed at higher fields. We believe that these oscillations arise from backscattering of electrons at the entrance barrier of the superlattice region (zero Fourier component of the potential). The backscattering probability depends on the density of final states and thus reflects the Landau levels of the unpatterned 2DEG regions that are

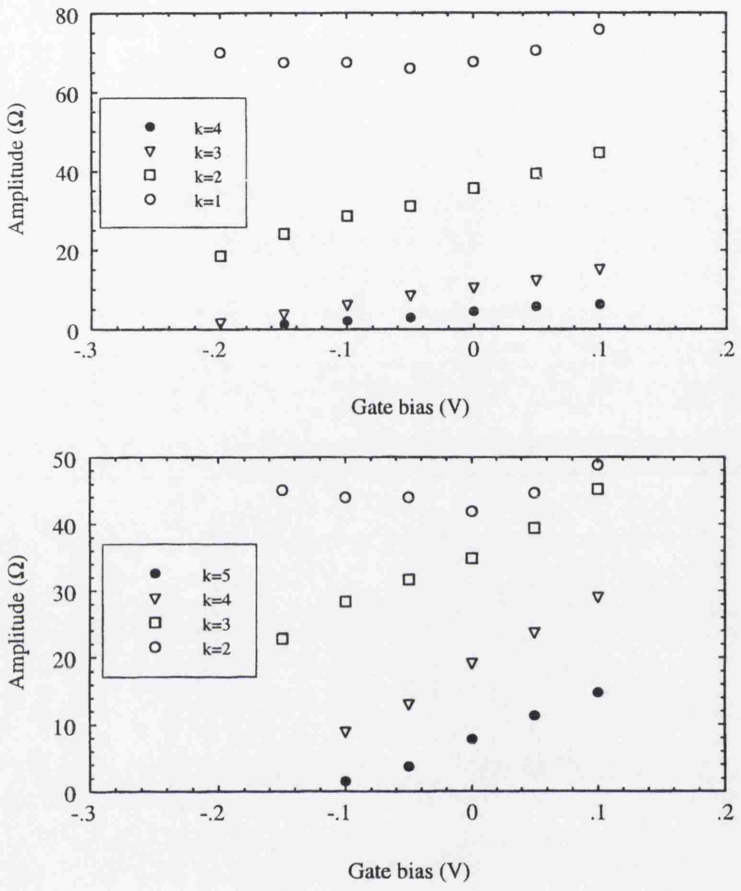

Figure 5.15: Plots of the first (top) and second (bottom) Fourier components of the commensurability-oscillation amplitudes vs. gate bias. The amplitude of commensurability oscillations increases with positive gate bias due to the mobility enhancement. All oscillations, except the one with lowest index (corresponding to the smallest cyclotron orbit), decrease in amplitude with negative gate bias.

used as connections to the superlattice area. This explanation is supported by the fact that these oscillations follow closely the SdH oscillations measured in the unpatterned device (bottom trace of Figure 5.13).

A648 device

The standard HEMT device showed commensurability oscillations only after IR illumination. The photo-ionization of the DX centers led to the appearance of a parallel sheet of electrons in the AlGaAs. In this case the ohmic contacts made a good electric contact to this parasitic layer and its effects could be clearly seen in the Shubnikov-de Haas, in the form of a raising background magnetoresistance that precluded the observation of the ρ_{xx} zeros. Therefore, in this device we have a conducting layer at the same potential as the 2DEG [5] between the gates and the 2DEG. This situation makes it virtually impossible for the electric field induced by the gate bias to penetrate into the 2DEG region and the gates are rendered ineffective in controlling the periodic potential at the 2DEG. Figure 5.16 shows the magnetoresistance traces measured at $T = 70\,\mathrm{mK}$ for different gate voltages. The 2DEG mobility and carrier concentration are practically unaffected for gate biases up to $-1.6\,\mathrm{V}$. However, the commensurability oscillations, clearly visible at $V_g = 0\,\mathrm{V}$, are gradually quenched by an increasingly negative gate bias. This effect is consistent with the hypothesis that the periodic modulation in this device arises from the selective ionization of the donors located in the spacings between the metal gates. The array of metal gates acts as a mask and the illumination of the device results in a modulated positive background due to ionized donors. The application of a negative gate bias depletes the parasitic layer in the regions under the gates and reduces the screening of the donors in these regions. The contribution of

[5] the 2DEG and the parasitic layer are electrically connected by the ohmic contacts that go all the way down to the 2DEG

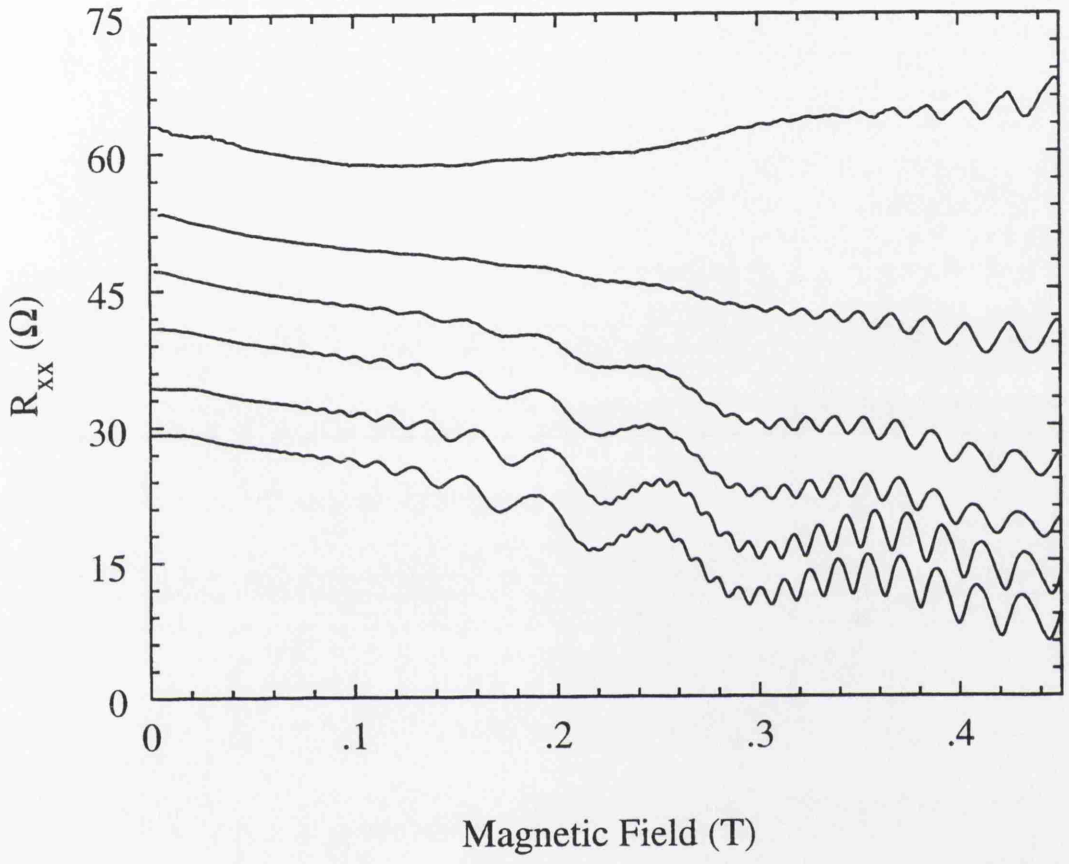

Figure 5.16: Commensurability oscillations measured in A648 LSSL device at $T = 70\,\mathrm{mK}$ for different gate voltages. From top to bottom, $V_g = -1.6\,\mathrm{V}$, $-1.4\,\mathrm{V}$, $-1.2\,\mathrm{V}$, $-1.0\,\mathrm{V}$, $-0.6\,\mathrm{V}$, $0\,\mathrm{V}$. The curves are shifted by $5\,\Omega$ from each other for clarity.

the ionized donors under the gates to the total background potential is thus enhanced and the contrast is gradually lost.

5.5 Differential gate bias

The gate structure of our LSSL device was originally designed to allow the application of different voltages to each set of interdigitated fingers so that an independent control of the amplitude of the modulation and the mean potential could be possible in principle. However we have seen in the preceding sections that the presence of a parasitic layer of electrons and the built-in potential due to strain severely disrupt the electrostatic control of the potential at the 2DEG by the gates. In particular, the independent control of the Fermi level and the modulation strength has not been possible in the devices studied in this work due to the deleterious effect of the parasitic layer.

Another possible result of the differential gate bias is the period-doubling of the superlattice potential. This should be immediately reflected in the periodicity of the commensurability oscillations. Figure 5.17 shows the magnetoresistance trace measured in A648 device with $V_{g1} = -1.3\,\mathrm{V}$ and $V_{g2} = -1.6\,\mathrm{V}$. The change of periodicity is confirmed by the FFT PSD estimation showing a distinct peak at $\nu \approx 0.47\,\mathrm{T}$. Figure 5.18 shows the results of the same experiment with the A601 device, with $V_{g1} = -0.2\,\mathrm{V}$, $V_{g2} = 0\,\mathrm{V}$.

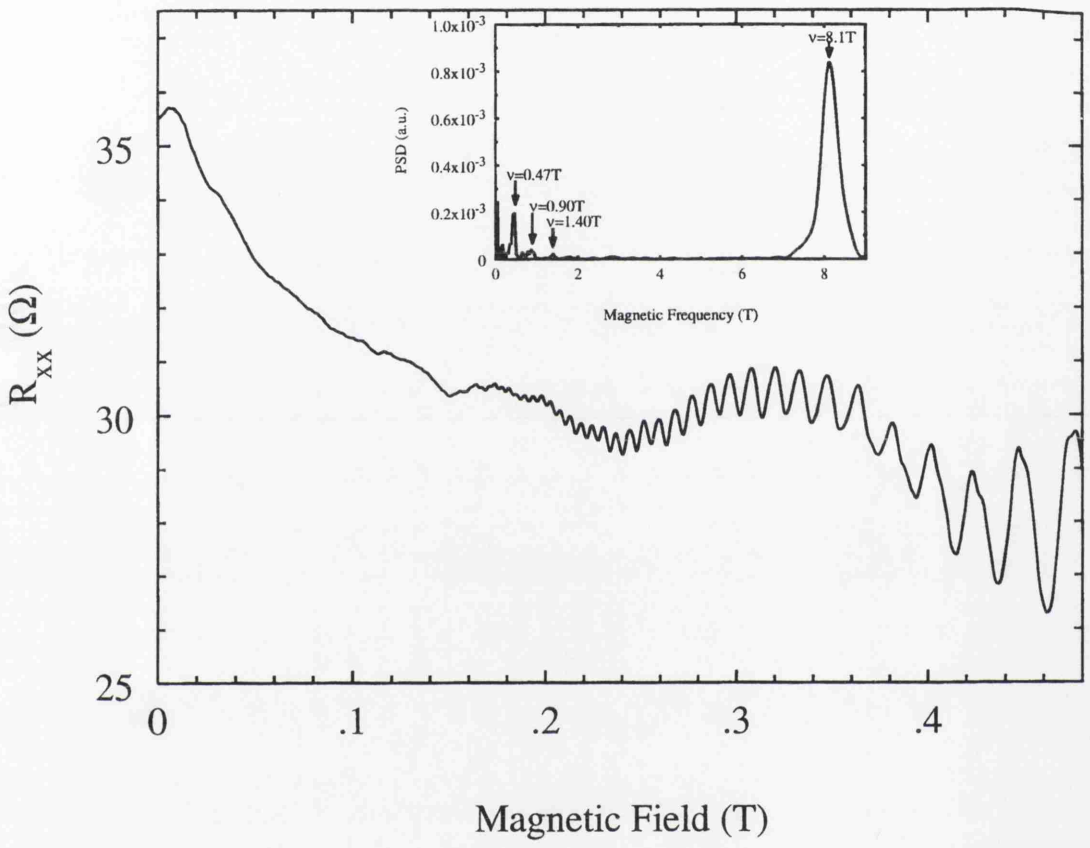

Figure 5.17: Magnetoresistance trace measured in A648 LSSL device at $T = 70$ mK with differential gate bias: $V_{g1} = -1.3\,\mathrm{V}$, $V_{g2} = -1.6\,\mathrm{V}$. Inset: Power Spectral Density showing a peak corresponding to a subharmonic of the periodicity of the array of gates.

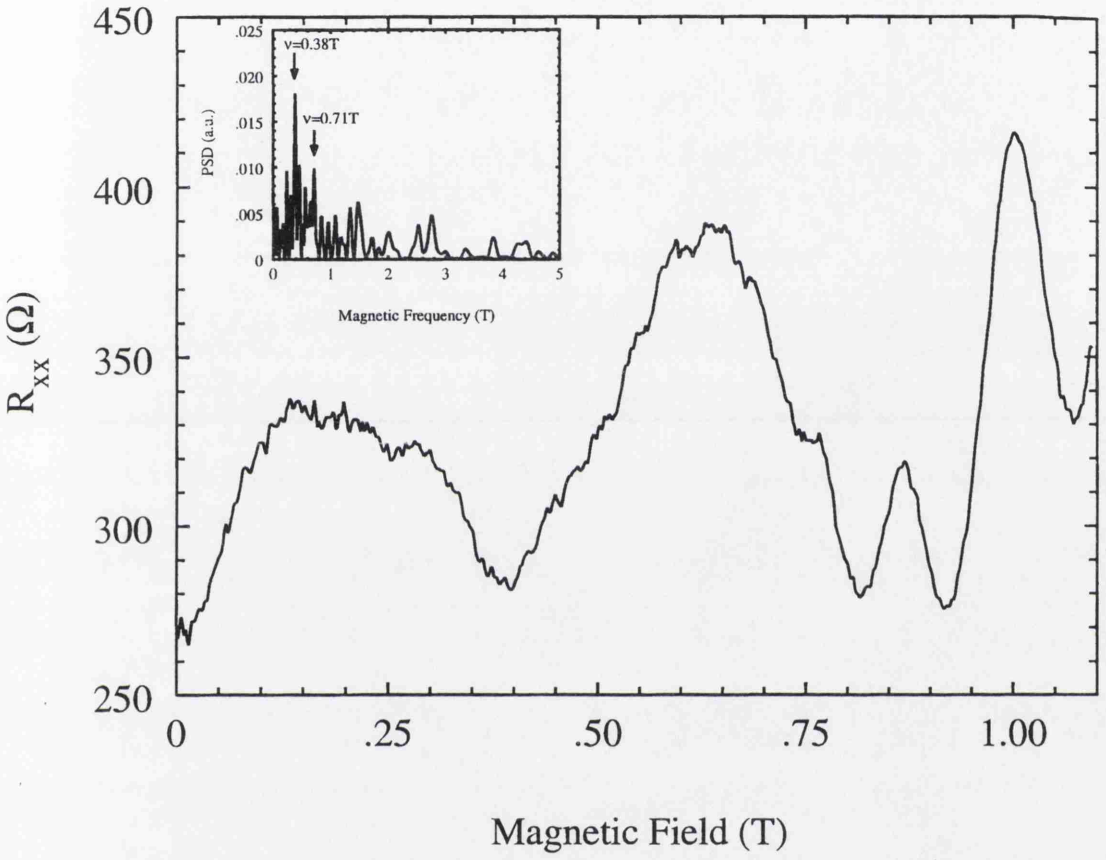

Figure 5.18: Magnetoresistance trace measured in A601 LSSL device at $T = 70\,\mathrm{mK}$ with differential gate bias: $V_{g1} = -0.2\,\mathrm{V}$, $V_{g2} = 0\,\mathrm{V}$. Inset: Power Spectral Density showing a peak corresponding to a subharmonic of the periodicity of the array of gates.

5.6 Temperature dependence of commensurability oscillations

A characteristic feature of commensurability oscillations that differentiates them from the SdH oscillations is that they are relatively unaffected by a temperature increase of a few degrees Kelvin. The study of the temperature dependence gives information about the relevant energy scales in the mechanism leading to the oscillations and confirms their semi-classic origin.

Figure 5.19 shows the magnetoresistance traces measured on A601 at $V_g = 0\,\mathrm{V}$ for different temperatures between 1.6 K and 21 K. Both the commensurability oscillations and the low-field positive magnetoresistance are clearly visible up to $T \approx 12\,\mathrm{K}$. The main effects of a temperature increase are

1. the smearing of the Fermi distribution
2. the reduction of electron mean free path

Using the semi-classical model we can see how the smearing of the Fermi distribution affects the amplitude of the oscillations. The electrons that contribute to transport have a distribution of velocities around v_F of the order of $\delta v = 2k_BT/\hbar k_F$. Then, for a given magnetic field, there will be a distribution of cyclotron radii that will smear out the resonance condition for the $\mathbf{E} \times \mathbf{B}$ drift. When the dispersion of cyclotron diameters, $\delta(2R_c) \approx 4k_BT/\hbar k_F\omega_c$, is of the order of the period of the superlattice the corresponding magnetoresistance oscillation is quenched. This picture predicts that the oscillations at low fields disappear first because the dispersion of cyclotron diameters is inversely proportional to magnetic field, and also that the harmonic signal is more affected by a temperature increase than the fundamental.

We can derive an analytical expression for the temperature dependence of the

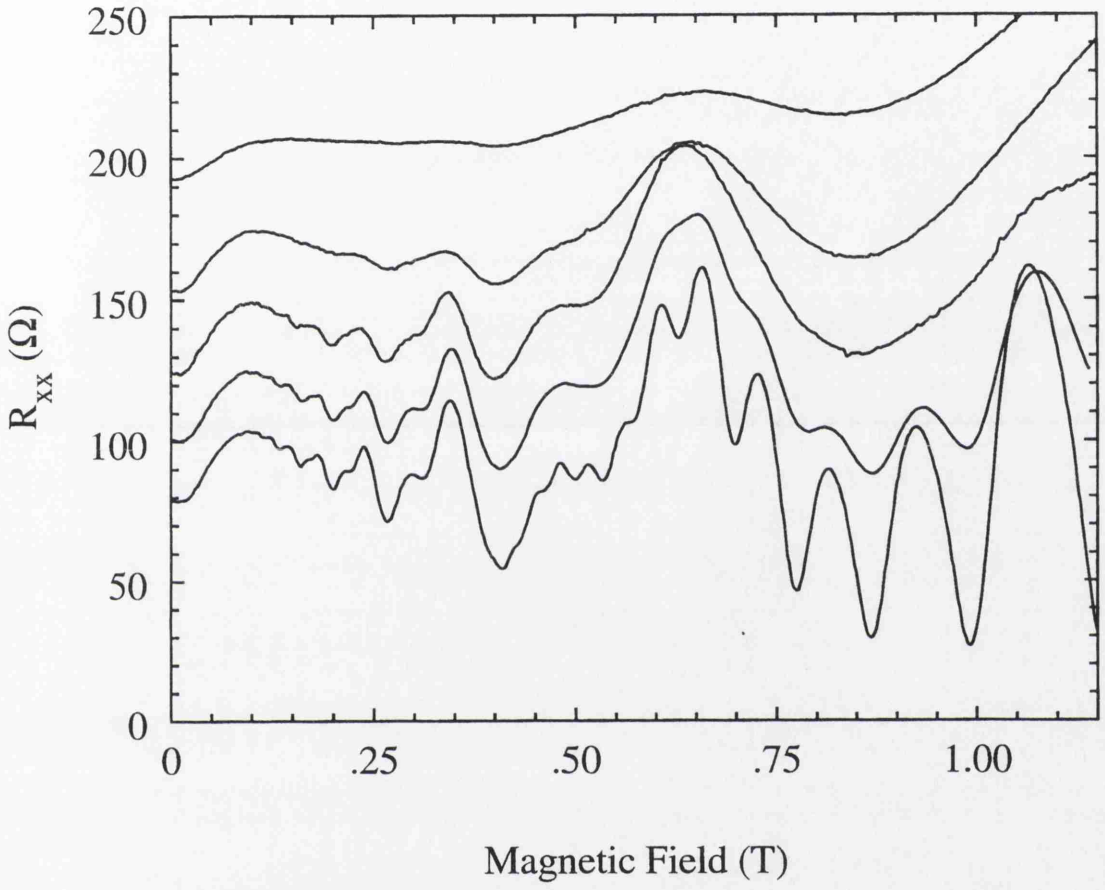

Figure 5.19: Magnetoresistance traces measured on A601 with $V_g = 0$ for different temperatures. From bottom to top, $T = 1.6\,\mathrm{K}$, $3.7\,\mathrm{K}$, $5.5\,\mathrm{K}$, $11.7\,\mathrm{K}$ and $21.0\,\mathrm{K}$. The curves are shifted by $20\,\Omega$ for clarity.

oscillations taking the thermal average [64]

$$\langle F(\epsilon)\rangle = -\int_0^\infty d\epsilon F(\epsilon)\frac{\partial f(\epsilon)}{\partial \epsilon} \tag{5.37}$$

of the expression 5.8, where $f(\epsilon)$ is the Fermi distribution.

Given that $E_F \gg k_B T$ we need to consider only the oscillatory part of 5.8 and can make use of the expansion

$$R_c = \frac{c\sqrt{2m}}{eB}E^{\frac{1}{2}} \approx \frac{c\sqrt{2m}}{eB}E_F^{\frac{1}{2}}\left(1+\frac{1}{2}\frac{E-E_F}{E_F}\right) \tag{5.38}$$

We find

$$\langle \cos^2\left(\frac{2\pi}{a}R_c\right)\rangle = \frac{1}{2}\left(1+\cos\left(\frac{4\pi}{a}R_c(E_F)\right)\int_0^\infty dx\frac{x^{i\alpha}}{[1+x]^2}\right) \tag{5.39}$$

where

$$\alpha = \frac{4\pi k_B T}{\hbar\omega_c k_F a} \tag{5.40}$$

The integral can be evaluated by contour integration [61] and we finally obtain

$$\langle \cos^2\left(\frac{2\pi}{a}R_c\right)\rangle = \frac{1}{2}\left(1-\frac{\alpha\pi}{\sinh(\alpha\pi)}\right)+\frac{\alpha\pi}{\sinh(\alpha\pi)}\cos^2\left(\frac{2\pi}{a}R_c\right) \tag{5.41}$$

The oscillation amplitude is reduced by a factor $\alpha\pi/\sinh(\alpha\pi)$ by effect of the thermal average. In Figure 5.20 we have plotted the temperature dependence of the oscillation amplitudes. The fit of the experimental data to a function of the form $\alpha\pi/\sinh(\alpha\pi)$ requires a value of α much larger than the predictions of Equation 5.40. This is partly due to the reduction of the mean free path with temperature and partly to a decrease of the strain-potential caused by a reduced differential shrinking of Ti gates. In Figure 5.21 we have plotted the amplitudes of $k = 1$ oscillation together with the thermal average prediction and the corrections due to the mobility drop. The measured oscillation amplitudes decrease faster than predicted because the strain potential,

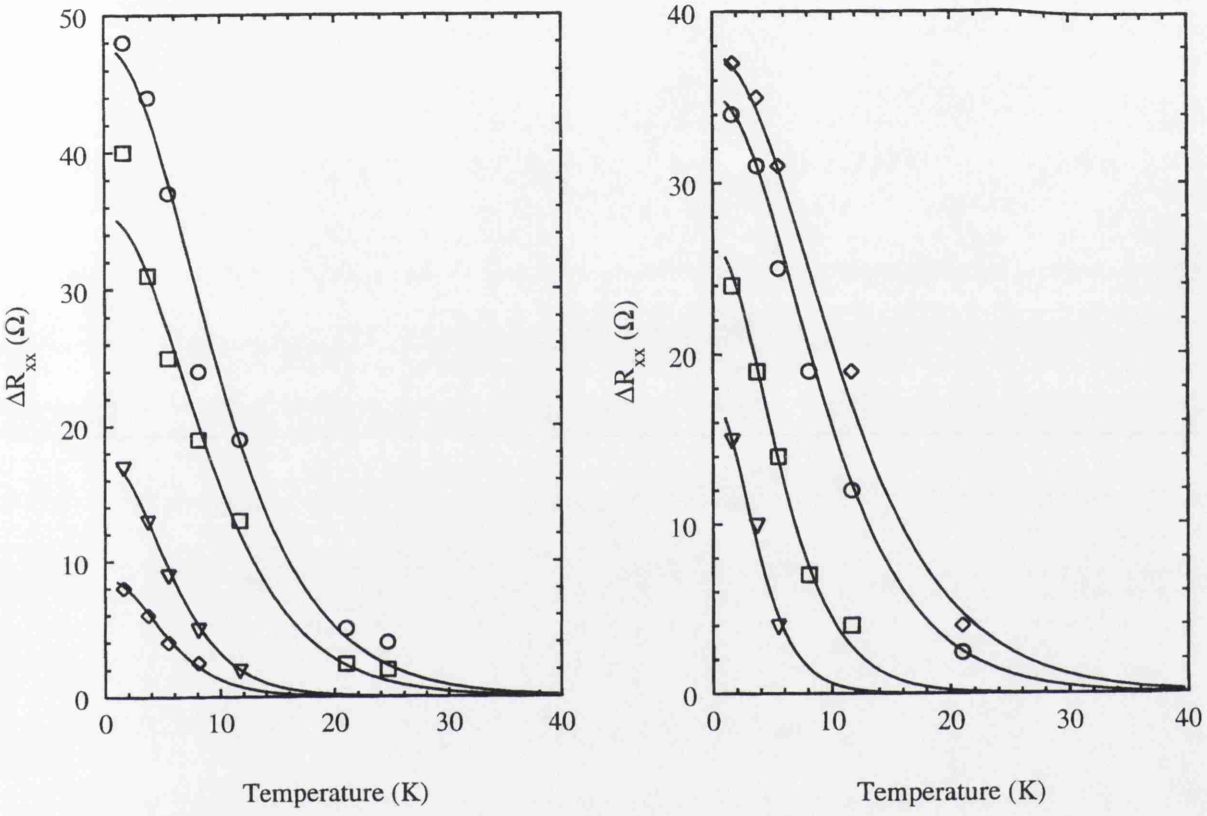

Figure 5.20: Temperature dependence of the oscillation amplitudes measured in A601. Solid lines are fits to functions of the form $\alpha\pi/\sinh(\alpha\pi)$.

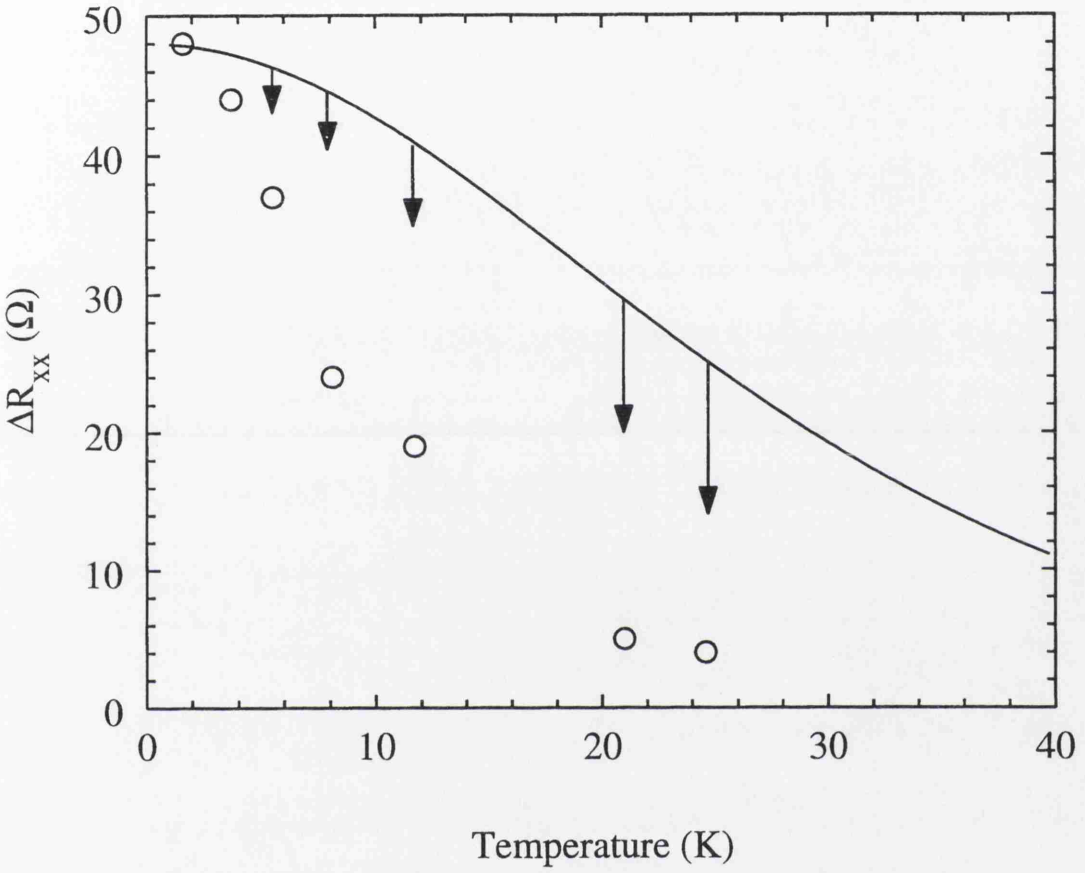

Figure 5.21: Temperature dependence of the fundamental $k = 1$ oscillation. The solid line is the theoretical prediction due to the smearing of the Fermi distribution. The arrows indicate the correction due to the decrease of mean free path. The amplitude of the oscillations is decreasing faster than expected because the strain potential decreases with temperature.

which enters quadratically in the amplitude, is being reduced by the increase of temperature.

Appendix

Fourier analysis of experimental data

The good quality of the data obtained from the LSSL devices has made it possible to use Fourier techniques to analyse the experimental results. These techniques have proven to be most useful in the analysis of the commensurability oscillations measured in the A601 shallow HEMT device where two Fourier components of the same order of magnitued are present in the magnetoresistance signal. It has been possible to extract accurate values for the relative strength of each component to be checked against the theoretical predictions. In this apendix we give a brief description of the numerical techniques involved.

The discrete Fourier Transform of N experimental points $\{ f_i \}$,

$$F_k = \sum_{j=0}^{N-1} \exp(2\pi ijk/N) f_j \tag{5.42}$$

has been calculated using the Fast Fourier Transform (FFT) algorithm due to Danielson and Lanczos [63]. The algorithm is based on the recursive subdivision of the original Fourier Transform into Fourier Transforms of even and odd data points down to Fourier Transforms of length 1, which are just the input data points. The complete Fourier Transform is then reconstructed combining the suitably reordered data points with the relevant phase factors. The

algorithm requires the function to be transformed to be sampled at equally spaced intervals. The result of the FFT can be viewed as the sampling of the continuous transformation

$$F(\nu) = \int_{-\infty}^{+\infty} f(t) \exp(2\pi i \nu t) dt \tag{5.43}$$

at frequencies

$$\nu_n \equiv \frac{n}{N\Delta}, \quad n = -\frac{N}{2}, \ldots, \frac{N}{2} \tag{5.44}$$

where Δ is the sampling rate. The relation between the continuous and the discrete Fourier Transforms is

$$F(\nu_n) \approx \Delta \; F_n \tag{5.45}$$

The magnetoresistance signal is periodic in $1/B$ whereas the experimental data is sampled at equally spaced B-field values. The inversion of B values yields a data set with an increasing density of data points towards the origin. A cubic-spline interpolation routine [63] is used to generate $N = 2048$ equally spaced points to be used in the FFT. The resulting FFT covers the "magnetic frequency" range $|\nu| < N/[4(B_0^{-1} - B_1^{-1})]$.

The Power Spectrum of the signal can be easily calculated from the FFT using the periodogram estimator

$$\begin{aligned} P(0) &= \frac{1}{N^2}|F_0|^2 \\ P(\nu_k) &= \frac{1}{N^2}\{|F_k|^2 + |F_{N-k}|^2\}, \quad k = 1, \ldots, \frac{N}{2} - 1 \\ P(\nu_{N/2}) &= \frac{1}{N^2}|F_{N/2}|^2 \end{aligned} \tag{5.46}$$

The periodogram is normalized to the mean squared amplitude of the signal and therefore the height of the Power Spectrum peaks depends on the magnetic field range used in the FFT. The effects of *frequency leakage* are reduced using a Parzen window [63]. The zero offsets and slow varying background that obscure the Power Spectrum calculation can be readily eliminated by differentiating the data. This procedure enhances the higher frequency peaks so that the ratio between the peak heights of second and first Fourier components for the differentiated data is four times its value for the raw data. All the FFT spectra shown in this work correspond to differentiated data.

The separation of the Fourier components from the magnetoresistance signal was achieved by digitally filtering the experimental data. The FFT of the raw data was multiplied by a Welch window centered at the frequency of the relevant PSD peak. An inverse FFT yields the component of the signal at the selected frequency. Figure 5.8 illustrates the filtering process on experimental data.

Conclusions

We have developed a fabrication process to realize Lateral Surface Superlattices devices for transport experiments at low temperatures. The fabrication of LSSL devices is a technologically demanding process involving high-resolution electron beam lithography and several other standard techniques of microelectronics that have been pushed to their limits because of the small dimensions of the devices. The difficulty of obtaining a good LSSL device like the ones studied in this work is considerable due to the proximity of the 80 submicron fingers that form the interdigitated gate structure. This fact poses severe problems for the lithography and especially for lift-off, since a few breaks in the gate structure completely ruin the superlattice device. Moreover, the requirements of low temperature operation and high mobility 2DEG demand high standards in the ohmic contacts and in the epitaxial HEMT layers that are not easily attainable. A great deal of time and effort has been devoted to the fabrication of the devices.

The small dimensions of the device, imposed by the limitations of the lithographic technique, have made it possible to study classical-size effects in the magnetoresistance of the ungated device structure due to the interaction

of the cyclotron orbit with the walls of the conduction channel. The study of the low field magnetoresistance of the ungated device has been taken as a reference point for the analysis of the periodic modulation effects on the 2DEG.

The commensurability oscillations of the magnetoresistance, arising from classical resonances between the cyclotron orbit and the period of the superlattice, have been studied on LSSL devices with different 2DEG depths. We have demonstrated that the proximity of the 2DEG to the surface leads to a stronger coupling between the electron gas and the surface potential that is directly reflected in the commensurability oscillations. An exceptionally strong second Fourier component in the commensurability oscillations has been measured that is not present in the "control" standard HEMT device nor in the data published in the literature. The Fourier analysis of the experimental data has made it possible to reconstruct the effective potential and we have found a first harmonic content much larger than the value predicted by electrostatics. The remarkable agreement between the potential deduced from experiment and theoretical calculations based on deformation potential shows that 2DEG modulation is mainly due to the compression of the GaAs caused by the differential shrinking of the metal gates. The presence of the "uncontrollable" strain potential in LSSL devices may constitute a limitation for LSSL device operation where electrostatic control of the effective potential is required. The temperature dependence of the commensurability-oscillation amplitudes confirms its semi-classical origin. We find that the amplitudes decay faster than the semi-classical theory predicts, which is consistent with the reduction of differential shrinking as temperature is risen.

LSSL devices have not fullfilled the initial expectations in terms of versatility and controllability of the 2DEG. In this respect, good quality 2DEG layers without parasitic free electrons between the surface and the 2DEG are essen-

tial. We have shown that shallow 2DEGs, which are essential for short-period superlattice devices, provide an enhanced coupling with the surface potential. However, the high mobility of the shallow device is achieved thanks to a parasitic layer of electrons around the donors. The depletion of this layer by the gate voltage causes a significant mobility drop. Moreover, the presence of a large built-in stress potential makes the electrostatic control of the 2DEG potential very poor. Research on shallow 2DEG layers has recently attracted much attention and it may lead to improved structures in the future. The success of "high-temperature" quantum point contacts on shallow structures has arisen the interest on the application of shallow 2DEG layers to other kind of devices, and the measurement of commensurability oscillations in LSSLs is a very direct means of assessing the effective potential at the 2DEG level.

Suggestions for future work

The establishment of a technological process to fabricate LSSL devices opens up many possibilites for further research on periodically-modulated 2DEGs. In turn, low-temperature (4 K) magnetoresistance measurements on LSSL devices yield direct information on the potential at the 2DEG level, making LSSL devices ideal for testing the behaviour of novel material structures and guiding the research for an improved shallow 2DEG layer design. The growth, fabrication and measuring facilities available in the Department bring the opportunity to make progress in this direction.

By making use of the new, state-of-the art lithography system which has recently become available in the Department, lower periodicity devices could be studied. Again, commensurability oscillations could be used to probe the effective potential at the 2DEG level. These short-period devices are expected to induce considerably smaller modulation of the 2DEG and could give some information on the effect of the random impurity potential on gated devices. Short-period devices on shallow 2DEG material could also be used to test the "strain theory", since it predicts that the second Fourier component of the commensurability oscillations is strongly attenuated for small-period super-

lattices ($a \leq 100\,\mathrm{nm}$). A systematic gate-bias study of different period and different mark-space ratio superlattices could yield relevant information in order to separate the effects of strain and electrostatic potential.

To take full advantage of the milliKelvin and high magnetic field facilities of the Physiscs Department some more experiments on LSSL devices could be attempted. At fridge temperatures and for a fixed magnetic field, a gate sweep should allow the observation of edge-state reflection. For a fixed value of magnetic field, the gate bias could be adjusted so that only one edge-channel is allowed through the gates. This would transform the transport through the device into a one-dimensional problem and would increase the probability of observing quantum effects.

The study of a series of 3, 5, 7, ...interdigitated finger devices could be interesting in order to observe the transition from resonant-tunneling devices to a true superlattice device.

Bibliography

[1] L. Esaki and R. Tsu, *IBM J. Res. Dev.* **14**, 61 (1970)

[2] L. Esaki and L. L. Chang, *Phys. Rev. Lett.* **33**, 495 (1974)

[3] F. Bloch,*Z. Phys.* **52**,555 (1928)

[4] S. E. Ulloa, E. Castaño, and G. Kirczenow, *Phys. Rev. B* **41**, 12350 (1990)

[5] K. Ismail, D. A. Antoniadis, and H. I. Smith,*Appl. Phys. Lett.***54**, 1130 (1989)

[6] D. R. Hofstader, *Phys. Rev. B* **14**, 2239 (1976)

[7] L. P. Kowenhoven, F. W. J. Hekking, B. J. van Wees, C. J. P. Harmans, C. E. Timmering, and C. T. Foxon, *Phys. Rev. Lett.* **65**, 361 (1990)

[8] J. H. Davies and J. A. Nixon, *Phys. Rev. B* **39**, 3423

[9] D. Weiss, K. vom Klitzing, K. Ploog, and G. Weimann, *Europhys. Lett.* **8**, 179 (1989)

[10] R. W. Winkler and J. P. Kotthaus, *Phys. Rev. Lett.* **62**, 1177 (1989)

[11] R. R. Gerhardts, D. Weiss, and K. von Klitzing, *Phys. Rev. Lett.* **62**, 1173 (1989)

[12] C. W. J. Beenaker, *Phys. Rev. Lett.* **62**, 2020 (1989)

[13] C. Zhang and R. R. Gerhardts, Phys. Rev. B **41**, 12850 (1990)

[14] R. Cusco, M. C. Holland, J. H. Davies, E. Skuras, A. R. Long and S. P. Beaumont, *Surface Science (in press)* (1994)

[15] P. M. Solomon and H. Morkoç, *IEEE Trans. Electron. Devices* **ED**-31, 10105 (1984)

[16] L. D. Landau and E. M. Lifshitz, *Quantum Mechanics*, Pergamon Press, Oxford, 1977

[17] M. Abramowitz and I. A. Stegun, eds., *Handbook of Mathematical Functions*, Dover Publications, New York, 1965

[18] B. J. van Wees, H. van Houten, C. W. J. Beenakker, J. G. Williamson, L. P. Kowenhowen, P. van der Marel, and C. T. Foxon, *Phys. Rev. Lett.* **60**, 848 (1988)

[19] D. A. Wharam, T. J. Thornton, R. Newbury, M. Pepper, H. Ahmed, J. E. F. Frost, D. G. Hasko, D. C. Peakock, D. A. Ritchie, and G. A. C. Jones, *J. Phys. C* **21**, L209 (1988)

[20] J. E. F. Frost, D. A. Ritchie, and G. A. C. Jones, *J. Crystal Growth* **111**, 305 (1991)

[21] G. L. Snider, I-Hsing Tan, M. S. Miller, M. J. Rooks, E. L. Hu, *Superlattices and Microstructrures* **11**, No. 3, (1992)

[22] P. M. Mooney, *J. Appl. Phys.* **67** (3) (1990)

[23] P. M. Solomon, S. L. Wright and C. Lanza. *SuperLattices and Microstructures* **2**, 521 (1986)

[24] E. H. Rhoderick and R. H. Williams, *Metal Semiconductor Contacts*, 2^{nd} edition, Clarendon Press, Oxford, 1988

[25] M. Born and E. Wolf, *Principles of Optics*, Pergamon Press, Oxford, 1975

[26] T. J. Thornton, M. Pepper, , H. Ahmed, D. Andrews, and G. D. Davies, *Phys. Rev. Lett.* **56**, 1198 (1986)

[27] H. Z. Zheng, H. P. Wei, D. C. Tsui, and G. Weimann, *Phys. Rev. B* **34**, 5635 (1986)

[28] B. J. van Wees, H. van Houten, C. W. J. Beenakker, J. G. Williamson, L. P. Kouwenhoven, D. van der Marel, and C. T. Foxon, *Phys. Rev. Lett.* **60**, 848 (1988).

[29] P. H. Beton, E. S. Alves, P. C. Main, L. Eaves, M. W. Dellow, M. Henini, O. H. Hughes, S. P. Beaumont, and C. D. W. Wilkinson, *Phys. Rev. B***42**, 9229 (1990)

[30] P. L. McEuen, A. Szafer, C. A. Richter, B. W: Alphenaar, J. K. Jain, A. D. Stone, R. G. Wheeler, and R. N. Sacks, *Phys. Rev. Lett.* **64**, 2062 (1990)

[31] H. Weiss, *Semiconductors and Semimetals*, Vol. 1, Academic Press, New York, 1966

[32] C. W. J. Beenakker and H. van Houten, *Solid State Physics*, Vol. 44, 1, Academic Press, 1991

[33] D. P. Blair and P. H. Sydenham, *J. Phys. E: Scientific Instruments*, **8**, 1975

[34] B. L. Altshuer and A. G. Aronov,*Sov. Phys. -JETP* **50**, 968 (1979)

[35] A. M. Finkel'stein, *Sov. Phys. -JETP* **57**, 97 (1983)

[36] H. Fukuyama, Y. Isawa, and H. Yasuhara, *J. Phys. Soc. Jpn.* **52**, 16 (1983)

[37] K. K. Choi, D. C. Tsui, and S. C. Palmateer, *Phys. Rev. B*, **33**, 8216 (1986)

[38] K. von Klitzing, G. Dorda, and M. Pepper. *Phys. Rev. Lett.* **45**, 494 (1980)

[39] E. N. Adams and T. D. Holstein, *J. Phys. Chem. Solids*, **10**, 254

[40] N. W. Ashcroft and N. D. Mermin, *Solid State Physics*, Holt, Rinehart and Wilson, New York (1976)

[41] R. K. Pathria, *Statistical Mechanics*, Pergamon Press (1972)

[42] T. J. Thornton, M. L. Roukes, A. Scherer, and B. P. Van de Gaag, *Phys. Rev. Lett.* **63**, 2128 (1989)

[43] E. Ditlefsen and J. Lothe, *Philos. Mag.* **14**, 759 (1966)

[44] A. B. Pippard, *Magnetoresistance in Metals*, Cambridge University Press (1989)

[45] R. P. Feynman and A. R. Hibbs. *Quantum mechanics and Path Integrals"*, Mc. Graw-Hill Book Co., New York, 1965

[46] A. Houghton, J. R. Senna, and S. C. Ying, *Phys. Rev. B* **25**, 2196 (1982)

[47] F. Stern,*Phys. Rev. Lett.*, **18**, 546 (1967)

[48] B. K. Ridley, *Quantum Processes in Semiconductors*, Clarendon Press, Oxford (1988)

[49] T. Ando, *J. Phys. Soc. Jpn.* **36**, 1521 (1974)

[50] T. Ando, *J. Phys. Soc. Jpn.* **53**, 3126 (1984)

[51] R. Hang, K. von Klitzing and K. Ploog, *Phys. Rev. B* **35**, 5933 (1987)

[52] A. Isihara and L. Smrčka, *J. Phys. C* **19**, 6777 (1986)

[53] S. Das Sarma and F. Stern, *Phys. Rev. B* **32**, 8442 (1985)

[54] P. T. Cooleridge, *Phys. Rev. B* **44**, 3793 (1991)

[55] J. P. Kotthaus and D. Heitmann, *Surface Science* **113**, 481 (1981)

[56] J. H. Davies and I. A. Larkin. *Phys. Rev. B* **49**, 4800 (1994)

[57] J. D. Jackson, *Classical Electrodynamics*, John Wiley & Sons, New York (1975)

[58] P. Vasilopoulos, F. M. Peeters, *Phys. Rev. Lett.* **63**, 2120 (1989)

[59] P. Streda and A. H. MacDonald, *Phys. Rev. B* **41**, 11892 (1990)

[60] U. Wulf, V. Gudmunsson, and R. R. Gerhardts, *Phys. Rev. B* **38**, 4218 (1988)

[61] G. Arfken, *Mathematical Methods for Physicists*, Academic Press, N.Y.

[62] L. D. Landau, E. M. Lifshitz, A. M. Kosevich, and L. P. Pitaevskii, *Theory of Elasticity*, Pergamon, Oxford (1986)

[63] W. H. Press, B. P. Flannery, S. A. Teulosky, W. T. Vettering, *Numerical Recipes. The Art of Scientific Computing*, Cambridge University Press (1989)

[64] J. M. Ziman, Electrons and Phonons, Oxford University Press (1960)